PRE-FABRICATED SURFACES FOR ASSESSMENT OF SPATIAL RESOLUTION AND PROTEOMIC ANALYSIS OF TISSUE SAMPLES USING IMAGING MASS SPECTROMETRY

By
Faizan Zubair

Dissertation
Submitted to the Faculty of the
Graduate School of Vanderbilt University
in partial fulfillment of the requirements
for the degree of

DOCTOR OF PHILOSOPHY

in

Chemical Engineering
August, 2016
Nashville, Tennessee

Approved:

Paul E. Laibinis, Ph.D.
G. Kane Jennings, Ph.D.
John A. McLean, Ph.D.
Matthew J. Lang, Ph.D.
Richard M. Caprioli, Ph.D.

This work is dedicated to my mom and dad who taught me the value of hard work.

ACKNOWLEDGEMENTS

First and foremost, I will like to thank my research and teaching mentor, Paul Laibinis, for his invaluable guidance advice throughout my time at Vanderbilt. He constantly challenged me during our scientific discussions encouraging me to dig deeper and see the bigger perspective. I will also like to thank my co-advisor, Richard Caprioli, for his insight and direction, and sharing his enthusiasm for science. Thanks also to my Ph.D. committee: G. Kane Jennings, John A. McLean and Matthew J. Lang for their support and guidance.

Special thanks to Junhai Yang for being a friend and a mentor especially during my early days in Mass Spectrometry Research Center (MSRC) when I knew very little about mass spectrometry. Thanks to Jeremy Norris for support, guidance and feedback. I will also like to thank Audra Judd for keeping me in line particularly in regards to lab safety.

I am very thankful to the past and current members of the MSRC for providing an excellent environment for research and growth. Thanks in particular to Kerri Grove, Boone Prentice, Raf Van de Plas, Jeffery Spraggins, Kevin Schey, Jessica Moore, Chad Chumbley, David Rizzo and Jamie Wenke. Special thanks to Maureen Casey for her words of wisdom and positive outlook.

I will like to thank undergraduates who worked with me including Paul Kempler, Will Swisher, and Marie Armbruster. They enriched my research experience at Vanderbilt. Thanks for all the great work that you accomplished while working with me. You all have a bright future ahead of you.

Finally, I gratefully acknowledge funding support provided by NIH 5P41 GM103391-03.

TABLE OF CONTENTS

Page

LIST OF TABLES

Page

LIST OF FIGURES

Page

LIST OF ABBREVIATIONS

ACN	Acetonitrile
AcOH	Acetic acid
CAD	Computer-aided design
CDF	Cumulative density function
DESI	Desorption electrospray ionization
EI	Electron ionization
FTICR	Fourier transform ion cyclotron resonance
FTMS	Fourier transform mass spectrometry
FWHM	Full-width-at-half-maximum
HDT	n-Hexadecanethiol
IMS	Imaging mass spectrometry
LSF	Line spread function
MALDI	Matrix-assisted laser desorption/ ionization
MCP	Microchannel plate
MOVPE	Metal organic vapor phase epitaxy

ORO	Oil red O
PDF	Probability density function
PIE	Pulsed ion extraction
PSF	Point spread function
SIMS	Secondary ion mass spectrometry
TAZ	3-(4-Biphenylyl)-4-phenyl-5-*tert*-butyl phenyl-1,2,4-triazole
TFA	Trifluoroacetic acid
TOF	Time-of-flight
TPBi	2,2′,2″-(1,3,5-Benzinetriyl)-tris(1-phenyl-1-H-benzimidazole)
γ	Width for a Lorentzian distribution
σ	Width for a Gaussian distribution

CHAPTER 1. MALDI IMAGING MASS SPECTROMETRY: AN OVERVIEW

Matrix-assisted laser desorption/ionization (MALDI) imaging mass spectrometry (IMS) is an enabling tool in biological research. Since the first publication in 1997,[1] the technology has been applied to study the distribution of a wide variety of analyte classes including metabolites, lipids, peptides, and proteins in biological samples.[2-4] In a typical MALDI IMS experiment, a frozen or fixed tissue is sectioned and thaw-mounted onto a target. The tissue section is then coated with a MALDI matrix usually by sublimation or a spray-based method. The matrix-coated tissue sample is analyzed by a serial raster of a laser across the tissue section, acquiring a mass spectrum at each defined x, y coordinate. Following data acquisition, the spectral intensities can be plotted for multiple ions of interest to provide two-dimensional maps of their molecular distribution.

Current techniques for mapping the distributions of species in a biological tissue include immunohistochemistry, chemical staining, and radioactive labeling. In general, these techniques rely on an ability to quantify specific targets in the specimen, usually requiring prior knowledge of their presence and often tags for their detection. Furthermore, these techniques typically allow the investigation of one compound at a time. IMS is superior to these approaches in that it can detect hundreds of molecular species at a time and requires no prior knowledge about a specimen thereby making it a particularly powerful tool for discovery.[5-6] In this introductory chapter, I provide relevant background and discuss multiple aspects of this technology. In the subsequent chapters, my contributions to this field are described.

1.1. Ionization Methods

Before molecules can be analyzed by mass spectrometry (MS), they must be ionized. Current approaches are typically categorized into those involving soft and hard ionization. Electron ionization (EI) is the most common hard ionization method. In this approach, energetic electrons are fired directly at atoms or molecules in the gas phase to produce ions. The highly energetic nature of this process typically results in the fragmentation of large molecules. As a result, investigations using hard ionization methods are typically limited to the analysis of compounds weighing below 600 Da.

The development of soft ionization techniques such as matrix-assisted laser desorption/ionization (MALDI) and electrospray ionization (ESI) for mass spectrometry has enabled the study of large molecules weighing up to hundreds of thousands of Daltons.[7] These soft ionization methods are so labeled because the energy is gradually imparted to the molecules. As a result, these methods are able to vaporize and ionize large intact molecules without extensive fragmentation.[8-9] In ESI, a high voltage (2.5 – 6.0 kV) is applied between a nozzle and a surrounding chamber causing an ejection of a solution as charged droplets. As the solvent evaporates, electrostatic forces within the droplets accumulate and cause ion ejection. In this process, multiply charged species may also be formed, which has been useful for extending the practical mass range of intact molecules that may be detected.

Figure 1.1 illustrates key aspects of the MALDI process. Central to this soft ionization approach is the use of a matrix—typically a small organic molecule that efficiently absorbs laser energy. The analyte is co-crystallized with the matrix so that a laser striking this co-crystal results in the vaporization of both the matrix and the embedded analytes. In a second role, the

matrix molecule also helps to ionize the analyte molecules, although the exact mechanism of ionization is still debated.[10]

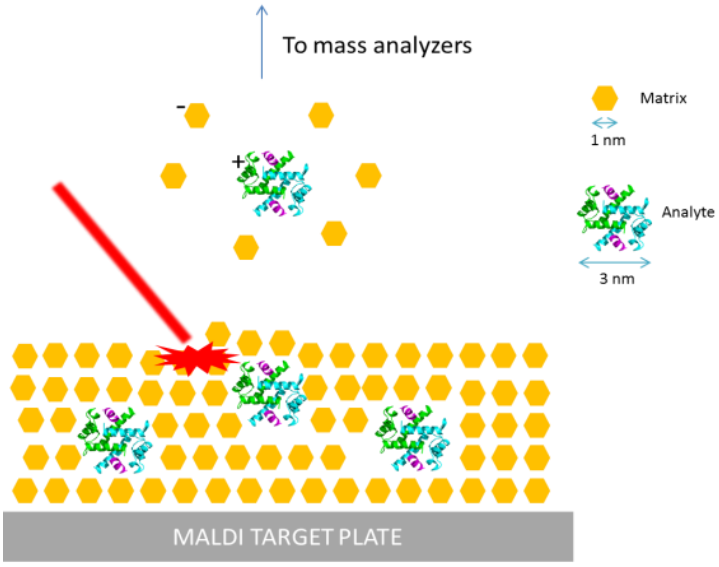

Figure 1.1. A schematic illustration of the MALDI mechanism. To provide a soft ionization process, the matrix and analyte molecules are first co-crystallized. Then, a laser is targeted at the co-crystal causing desorption and ionization of the molecules for detection.

A variety of other ionization methods have also been developed for imaging mass spectrometry, mainly secondary ion mass spectrometry (SIMS)[11-12] and desorption electrospray ionization (DESI). SIMS was conceptualized by J. J. Thomson in 1910, and the first experiments were conducted by Herzog and Viehbock in 1949.[13] In SIMS, a focused primary ion beam is targeted at the surface of the specimen and the ejected secondary ions that are analyzed using a mass spectrometer. SIMS is able to provide high spatial resolution (50-100 nm) but is typically limited to the analysis of molecules with m/z smaller than 2000 Da.[12]

DESI was developed in 2004 by Graham Cooks at Purdue University.[14] In this technique, charged droplets and solvent ions generated by electrospray are directed toward the surface to be analyzed. Upon impact, the charged particles solvate and ionize the molecules at the sample

surface. The resulting analyte ions travel through the air into a differentially pumped chamber that is connected to a mass spectrometer. DESI is limited to a spatial resolution of 35 μm and a mass range below m/z 2000.[15]

1.2. The Current State of MALDI-IMS Technology

There are three distinct yet interconnected areas of research in MALDI imaging mass spectrometry: sample preparation, instrumentation, and data analysis. Sample preparation includes the handling of tissue specimens, solvent washing to enhance particular signals, and the development of novel preparation methods. Instrumentation research focuses on enhancing sensitivity, increasing spatial resolution, and expanding the throughput of IMS instruments. Data analysis includes the development of new algorithms to do automatic data evaluation, statistical methods for data mining, and recent visualization techniques[16] for the fusion of imaging mass spectrometry results with those from other imaging modalities.

1.2.1. Sample Preparation

Sample preparation includes all steps prior to loading the sample in the mass spectrometer. These steps include the extraction of a tissue sample from an animal or a patient, its sectioning and mounting onto a substrate, any washing steps, and finally the application of the matrix. In general, the sample preparation steps must be tailored to the tissue type and the class of analytes to be analyzed.[17] Schwartz et al. investigated a range of sample preparation methods and found that the matrix, its crystal size, tissue washing procedures, matrix concentration, solvent composition, and concentration of signal-enhancing species such as TFA affected MALDI-MS signals.[18] In addition, the type of target (AnchorChip vs. Ground steel target) also influenced the signal.[19]

For the preparation of fresh-frozen tissues for MALDI-IMS, the tissue is mounted on a chuck using an optimal cutting temperature compound (OCT) and sectioned inside a cryostat into slices between 3-20 µm in thickness as shown in Figure 1.2. The sectioned tissue is thaw-mounted onto a conductive substrate that is typically indium tin oxide (ITO)-coated glass. The tissue section is then washed with solvents to remove unwanted species. If lipids are the analytes of interest, washes with buffer solutions are used to remove salts that may cause ion suppression.[20] If proteins are to be analyzed, organic washes are also used to remove lipids from the tissue sample.[21]

After the series of solvent washes, a matrix is applied to the tissue section. Typical delivery approaches include automated sprayers, a robotic spotter, or a sublimation device. Robotic spotters enable the best extraction of analytes from the tissue sample into the matrix; however, they suffer from a lower throughput due to the serial nature of this deposition approach. Spray-based methods can provide homogeneous coatings and a higher throughput and are an attractive option for most applications. Sublimation provides the ability to deposit matrix with a small crystal size that is useful for high-resolution applications.[22]

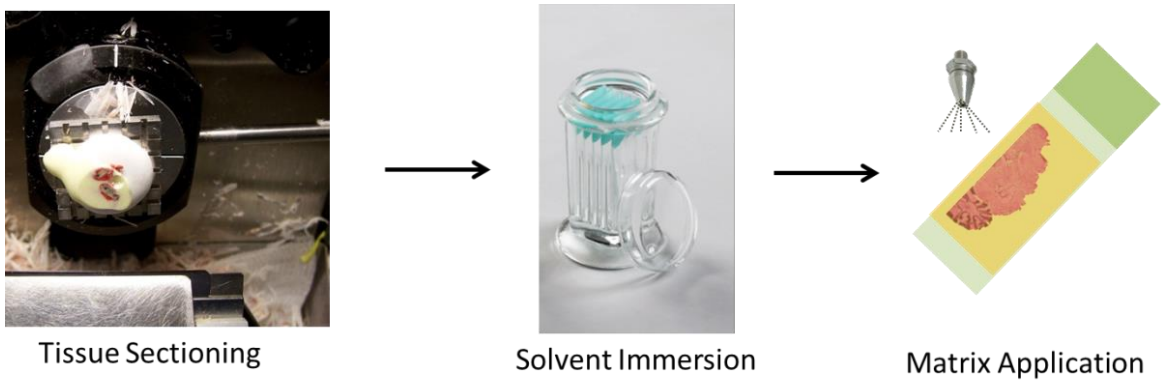

Figure 1.2. Typical sample preparation process involves cryosectioning of a tissue, solvent washing, and matrix application.

1.2.2. Instrumentation

MS instruments consist of a laser source, associated optics, a sample stage, a mass analyzer, and a detection scheme. The laser source provides the necessary energy to generate ions from a sample. For imaging, the laser beam can be focused and positioned at different locations on a sample to investigate spatial variations. This process occurs in a chamber that is typically operated at vacuum pressures below 10 mTorr although intermediate and atmospheric pressure MALDI have been developed.[23]

The development of mass analyzers with improved capabilities is an active area of research. Time-of-flight (TOF), quadrupole, Fourier transform ion cyclotron resonance (FTICR) and Orbitrap are among the most commonly used mass analyzers for MALDI-IMS.[24] In my work, I primarily relied on TOF and FTICR analyzers and the basis for their operations is detailed below.

TOF analyzers rely on the premise that all ions have the same initial kinetic energy as they are desorbed from a target. As the ions then accelerate through an electric field, their increase in kinetic energy is equivalent to the decrease in the electrical potential as described by

$$E_K = \frac{1}{2}mv^2 = zeV; v = \frac{D}{t} \quad (1.1)$$

where E_K is kinetic energy, m is mass, v is velocity, z is charge, t is the flight-time of an ion, eV is the applied voltage, and D is the distance to the detector. In eq 1.1, as D and eV are constant for all ions, the relationship between t and a m/z ratio can be expressed by:

$$t = D\sqrt{\frac{m}{2zeV}} \quad (1.2)$$

Eq 1.2 shows that *t* is directly proportional to the square-root of the mass-to-charge ratio. For ions of greater mass, a longer time is needed for them to reach the detector. As a result, time measurements of the detected signals are used to determine ion masses. In general, the mass resolution of TOF mass spectrometers is limited by the differences in energy provided to the analyte molecules from the laser pulse which results in ions varying in their initial kinetic energies. These differences compromise the relationship between the mass-to-charge ratio for an ion and its time-of-flight as expressed in eq 1.2.

Various methods have been developed to improve the resolution of TOF instruments. Delayed extraction introduces a delay of 100 – 300 ns in the application of an electric field post-ionization. During this time, ions of similar mass with greater kinetic energy travel further away from the target than those with less kinetic energy. When the voltage gradient is then introduced between the target plate and the ground electrode, the faster ions being further away from the target experience a lower electrical potential and therefore gain less kinetic energy by the electric field than do other ions. Conversely, ions having lower initial velocities are closer to the target when the field is applied, and these ions experience a higher electrical potential and a greater gain in kinetic energy. Thus, the result of this pulsed ion extraction process is to narrow the kinetic energy distribution of the ions.

Figure 1.3 shows an approach where the addition of a reflector to the ion path is used to further enhance the resolution of TOF instruments. A reflector is a voltage lens that reverses the direction of ion travel. Ions of the same m/z ratio that have a greater kinetic energy (shown in Figure 1.3 in gray) penetrate deeper into the reflector relative to those that have a lower kinetic energy (shown in Figure 1.3 in black). As a result, ions of the same m/z ratio with higher kinetic energy have longer path-lengths ensuring that they reach the detector at the same time as the ions

of the same m/z ratio with lower kinetic energy. By this process, the reflector sharpens the peak for common ions to improve mass resolution at the expense of minimal losses in sensitivity.

While TOF analyzers provide the highest mass range and are typically less expensive than other mass analyzers, they offer limited molecular specificity with a mass resolution on the order of 10,000.[25] More advanced multiple-reflection methods in time-of-flight mass spectrometry have been developed recently that enable mass resolution of up to 100,000 that show promise for the future.

The detector at the end of the flight-tube is responsible for measuring the intensity of the delivered ions as a function of time. A micro-channel plate (MCP) is the most common type of detector in a TOF-MS instrument. The MCP converts incident ions into measured secondary electrons with a rapid response time, although the efficiency of this conversion declines as the ion velocity decreases. Since the ion velocity varies inversely with the square root of mass for common kinetic energies, the detection efficiency for a MCP declines as the mass of the ion increases placing limits on the mass of the ion that can be detected.

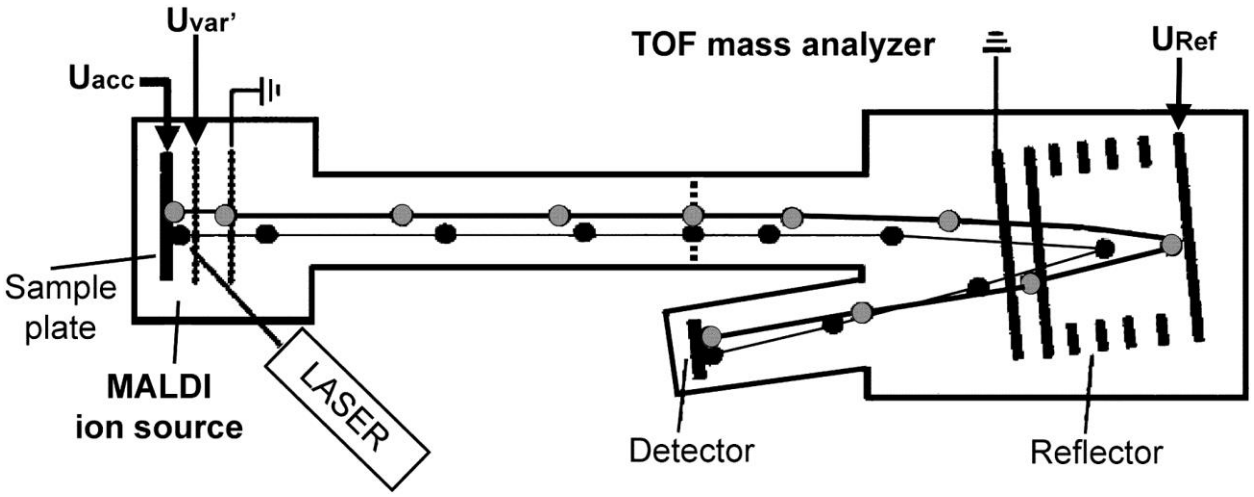

Figure 1.3. Schematic diagram of a TOF MS with a reflector. The MALDI ion source consists of a laser and a sample plate. The reflector improves the mass resolution by increasing the path

length for ions (i.e, those shown in gray) with greater kinetic energy. This figure is reproduced with permission of the Annual Review of Biochemistry.[26]

Fourier transform mass spectrometry (FTMS) is the most sensitive method of ion detection and also provides the highest mass accuracy for its signals. FTMS was developed by Melvin B. Comisarow and Alan G. Marshall in 1974.[27] In this method, the ions are trapped in an ion cyclotron resonance (ICR) cell by the magnetic field from a superconducting magnet that is cooled by a combination of liquid helium and nitrogen. The cost of these superconducting magnets makes this technique very expensive with only a handful of labs having access to these types of instruments.

The FTMS method of mass analysis relies on the measurement of resonant frequencies of the ions as they oscillate in the ICR cell. As the ions enter the ICR cell, they experience a Lorentz force (*F*) that is directly proportional to their charge (*z*), their velocity (*v*), and the strength of the magnetic field (*B*) by

$$F = zvB \tag{1.3}$$

As the Lorentz force acts in a direction perpendicular to the velocity of the ion and the magnetic field, the ions are forced to travel in a circular motion. The frequency of the ion motion (ω_c) is inversely proportional to its m/z ratio by

$$\frac{m}{z} = \frac{B}{2\pi\omega_c} \tag{1.4}$$

At this stage, no signal can be observed because the radius of motion is too small. To enhance this movement, a radio frequency sweep by excitation plates perturb the ions to higher orbits. As the ions are excited to higher orbits, they induce a current within the detector plates. The

frequency of the induced current is the same as the cyclotron frequency of the ions (ω_c), and the intensity of this current is proportional to the number of ions. The signal produced in the detector plates represents the convolution of all frequencies and their intensities. A Fourier transform is used to de-convolute the overall time-domain signal to produce a frequency vs. intensity spectrum that is then converted to a mass vs. intensity spectrum. A schematic overview of the FTMS operation is shown in Figure 1.4.

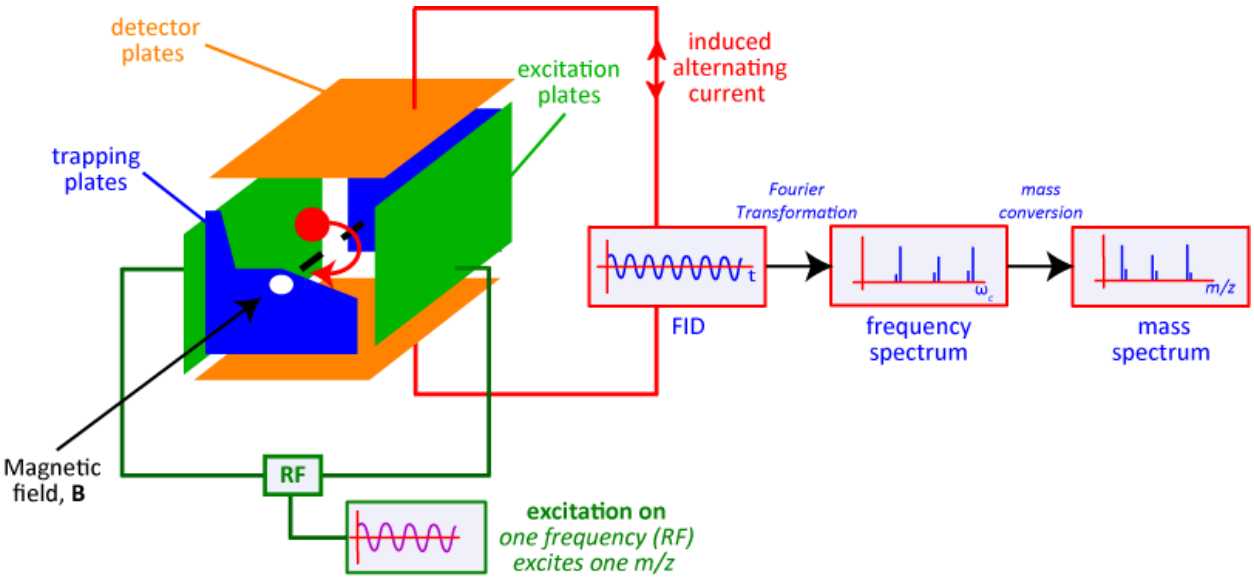

Figure 1.4. Schematic overview of the FTMS approach. Excitation plates produce a frequency sweep that excites the ions held in a resonance cell to a higher orbit. The ions in the higher orbit induce a measured current in the employed detector plates. The time domain signal for this current is Fourier transformed into a frequency spectrum that is then converted to a mass spectrum. This figure was reproduced with the permission of Dr. Paul Gates, University of Bristol.

1.2.3. Data Analysis

Data analysis is a critical component of the overall experimental scheme. Large data sets ranging from tens to hundreds of gigabytes are normally analyzed in MALDI-IMS. A variety of commercial packages are available for these operations. For example, FlexImaging provides a convenient format for visualizing image data acquired using Bruker instrumentation.

Several pre-processing steps are applied to the spectral data to enhance analysis. These include normalization, baseline subtraction, and peak picking. Normalization is used to account for local variations in crystal size and laser energies across the sample. Total ion current (TIC) is the most common parameter used for normalizing spectra. In this approach, the total area under the spectrum is computed and set equal across all spectra.[28] TIC normalization can improve the ability to compare signals among similar cell types; however, it is less useful for normalizing data obtained across significantly different cell types.[29] In those cases, the addition of mass exclusion lists corresponding to the dominant peaks from different regions may be required prior to TIC normalization to address the issue.

Another significant development in the area of data analysis is image fusion, where image data acquired using distinct imaging modalities are combined.[16] At the mass spectrometry level, data sets acquired using TOF and FTICR platforms can be fused together to combine the advantage from these methods. For example, TOF analyzers have a much higher throughput that is useful for high spatial resolution imaging. In contrast, FTICR analyzers offer a higher molecular specificity but at a lower throughput compared to TOF platforms. Image fusion couples the individual strengths of these techniques to allow ion images to be obtained that have both high spatial resolution and high chemical specificity. Perhaps more strikingly, images from IMS and microscopy can also be fused together to enhance spatial resolution.[16] Here, the high throughput and high spatial resolution of microscopy is combined with the molecular information from MALDI-IMS. In the future, the fusion of complementary imaging modalities can be expected to aid the visualization of increasingly complex biological and chemical details.

1.3. Research Objectives

MALDI-IMS has been used in a wide-range of applications spanning drug discovery and quantitation,[30] disease diagnosis,[31] clinical proteomics, microbiology,[32] food toxicity[33] and fundamental biological research. Diverse analyte classes such as drug molecules, metabolites, lipids, and proteins can be detected. Despite its immense analytical capability, IMS is primarily used for research applications. Clinical and industrial labs have been slow to adopt IMS due to its seemingly complex sample preparation procedures and lack of standardized methods. Different washing protocols, a multitude of available matrices, and variations in their use represent a huge obstacle for non-expert users.

An additional challenge for the broader use of MALDI IMS beyond the research laboratories is a lack of standardized methods to benchmark instrument performance. For example, the laser performance varies over its lifetime as does the cleanliness of the source and these factors influence the obtained MS signal. In addition, user-defined parameters such as laser energy and focus setting can introduce further variability in the data. The development of a standardized target for benchmarking instrument performance prior to obtaining an image would be exceedingly useful to reduce variability. Instrumentation specifications could be recorded to allow rigorous comparisons of imaging results obtained at different times and by different laboratories.

A goal in this thesis was to develop novel, readily standardized, and high-throughput preparation methods for MALDI-IMS that can reduce the burden of sample preparation from the end user and minimize experimental and instrumental variability. In this work, methods of surface modification, self-assembly, and lithography are used to produce tools for IMS that include user-friendly protocols. The developed techniques are intended to expedite the adoption

of MALDI IMS for clinical and industrial applications by their ease, reliability, and ability to be standardized. My specific objectives are outlined below:

1. Formulate a practical definition for spatial resolution in MALDI-IMS. Evaluate the effects of imaging parameters such as beam size, beam profile, and step size on the effective spatial resolution in obtained images.
2. Fabricate standardized patterned surfaces useful for objectively assessing and comparing MS instrument performance, particularly spatial resolution. The pattern would provide a defined set of features consisting of molecules that are readily desorbed and ionized by a laser source without requiring the presence of a MALDI matrix. These targets should be safe and stable over time to allow repeated use. Routine automated computational methods should also be developed for objectively assessing the effects of operating conditions on an instrument's spatial resolution prior to obtaining an image of a biological sample.
3. Develop pre-coated targets containing both matrix and an enzyme to provide a more rapid, simplified, readily standardized alternative to current sample preparation methods. These targets should include both matrix and enzyme to avoid the need for deposition steps by the end user. The method should allow proteins within a tissue sample to be digested and the resulting peptides be imaged directly from the tissue with minimal experimental effort or variability. For analysis, the resulting image data from peptide fragments will be linked to LC-MS/MS data to yield identification of the parent proteins in the tissue sample based on accurate mass.

CHAPTER 2. DEFINING SPATIAL RESOLUTION IN MALDI IMAGING MASS SPECTROMETRY

Spatial resolution is a critical parameter in imaging mass spectrometry (IMS). Aside from determining the overall quality of the resulting image, spatial resolution has significant consequences on the acquisition time of an image and its resulting file size. In general, the resolution of any image is directly related to the number of pixels in each unit area. Given that the pixels in MALDI-IMS are acquired in series, the acquisition time and file size for an image are directly proportional to the number of pixels. Thus, an improvement in the resolution of an image is often at the expense of longer acquisition times and larger file sizes.

This chapter develops theoretical foundations for defining spatial resolution in imaging mass spectrometry. The presented ideas and concepts are adapted from other surfaces analytical techniques such as light and electron microscopy, x-ray imaging, and SIMS. The first part of this chapter discusses the knife edge method and its use in measuring beam size for different beam profiles. The second part of this chapter focuses on defining a spatial resolution threshold for MALDI IMS and calculating the resulting spatial resolution for a combination of step sizes and beam sizes.

2.1. Knife-Edge Method

Beam size is an important parameter in determining spatial resolution as it defines the area responsible for generating a signal from a particular coordinate location in an image. The knife-edge method is commonly used in the surface analytical community to measure width of an incident beam, particularly for lasers. In this approach, a knife edge is translated through a

laser beam and the transmitted laser intensity is measured using a photodiode or other method of detection (Figure 2.1). A minimum in intensity is measured when the blade blocks the entire laser, while a maximum in intensity is observed when the laser is fully exposed. The laser intensity profile measured by the photodiode as a function of translation distance for the knife edge enables measurement of the beam width.

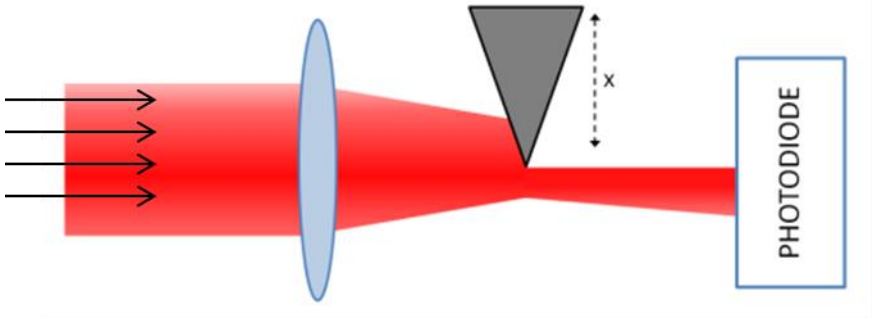

Figure 2.1. Measurement principle of the knife-edge method. The blade is translated along the x-direction, and the transmitted light is measured by a photodiode.

Figure 2.2 illustrates the application of the knife-edge to various Gaussian beam profiles. To consider the effect of beam size, Figure 2.2a shows the profiles for Gaussian beams of three different widths. For these cases, Figure 2.2b shows the expected total ion current as a blade is translated perpendicular to the direction of the beam. The fractional beam intensity that reaches a detector downstream varies from full to no intensity, differing in the required translation distance for the blade to accomplish this intensity change. Based on the shape of the profile in Figure 2.2b, the width of the Gaussian beam can be deduced where smaller beam widths generate sharper changes in the total ion current with blade movement.

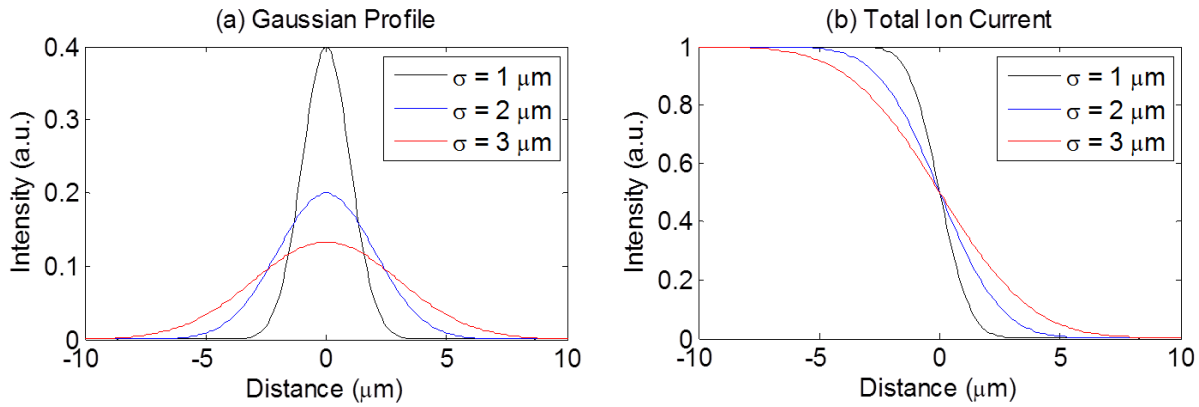

Figure 2.2. Application of the knife-edge method to measure the beam width. (a) Profiles for Gaussian beams of different widths σ (b) Expected total ion current as measured by a photodiode as a blade is translated across Gaussian beams of different widths.

2.2. Modeling 1-D Beams

In order to determine the resulting spatial resolution that could be obtained for an incident laser, it is useful to first determine the influence of its beam profile. In this section, three model profiles for the laser beam are considered: Top-hat, Gaussian, and Lorentzian. The probability density, cumulative density, and full-width-at-half-maximum (FWHM) for each of these beam profiles are listed in Table 2.1 and displayed in Figure 2.3. The FWHM is a standard measure of beam size and its relationship to overall signal intensity depends on the type of distribution. For the Top-hat distribution, its FWHM encompasses 100% of the intensity in its cumulative density function due to the sharp edges in its profile. For the Gaussian distribution, its FWHM contains 76% of the total intensity, corresponding to an associated increase in signal from 12% to 88% over this region. The Lorentzian distribution has broader tails and a sharper peak in comparison to the Gaussian distribution. As a result, only 50% of the total intensity is contained within the FWHM. The positions of its FWHM correspond to an associated increase in signal from 25% to 75%.

Table 2-1. Properties of one-dimensional Top-hat, Gaussian, and Lorentzian distributions centered at x = 0.

	Probability Density Function	Cumulative Density Function	FWHM
Top-hat	$\frac{1}{2a}\ for -a < x < a$	$\frac{x+a}{2a} for -a < x < a$	$2\,a$
Gaussian	$\frac{1}{\sigma\sqrt{2\pi}}\ exp\left(-\frac{x^2}{2\sigma^2}\right)$	$\frac{1}{2}\left[1+\mathrm{erf}\left(\frac{x}{\sigma\sqrt{2}}\right)\right]$	$2\sqrt{2ln2}\,\sigma$
Lorentzian	$\frac{1}{\pi\gamma\left[1+\left(\frac{x}{\gamma}\right)^2\right]}$	$\frac{1}{\pi}\arctan\left(\frac{x}{\gamma}\right)+\frac{1}{2}$	$2\,\gamma$

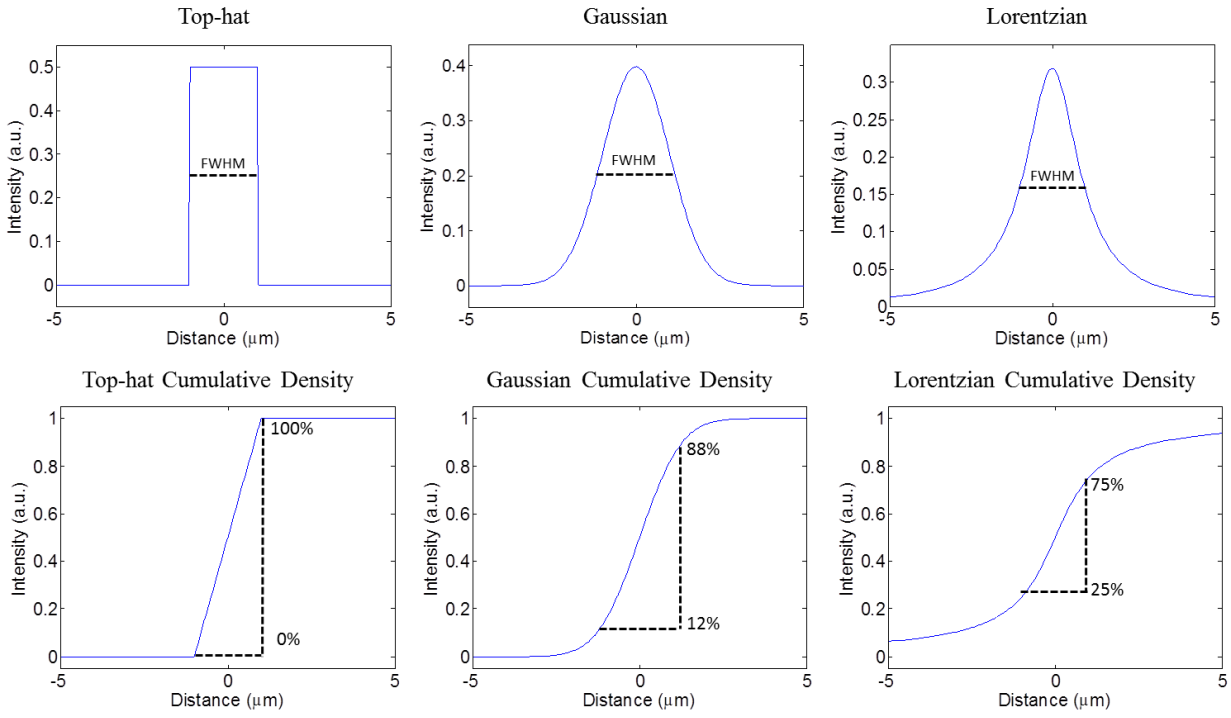

Figure 2.3. One-dimensional Top-hat, Gaussian, and Lorentzian distributions along with their cumulative density functions. All functions are centered at x = 0. The FWHM is marked for all three beam profiles.

2.3. Convolution of One-dimensional PSF with a Step Function

Model functions can be used to describe the loss of spatially separated differences between an object and its image as resulting from characteristics of the imaging instrument. The choice of model function to describe this effect depends on the optical setup. The images obtained for simple objects are calculated here considering various model functions. As a first example, image functions can be computed for an object that is defined by the step function:

$$o = 1 \quad for\ x \geq b$$
$$o = 0 \quad for\ x < b \tag{2.1}$$

where *o* represents the object function that changes its value from 0 to 1 at $x = b$. For a Top-hat beam, the image function can be easily constructed by imagining the Top-hat profile moving across this step function as shown in Figure 2.4. The width and the height of the Top-hat beam are $2a$ and $\frac{1}{2a}$, respectively, where *a* is an arbitrary constant. As the Top-hat beam approaches the edge of the boundary, the overlap between the Top-hat profile and the step function becomes positive. The integral of the overlap is equal to the area of the highlighted rectangle in Figure 2.4. For a Top-hat beam of normalized intensity, the intensity level across the beam is constant and is equal to $\frac{1}{2a}$. The length of the highlighted rectangle in Figure 2.4 is equal to $(x' - b + a)$ where x' corresponds to the center position of the Top-hat beam. The resulting image function, $i(x')$, is equal to the area of overlap by:

$$i(x') = \frac{x' - b + a}{2a} \quad for\ (b - a) \leq x' \leq (b + a) \tag{2.2}$$

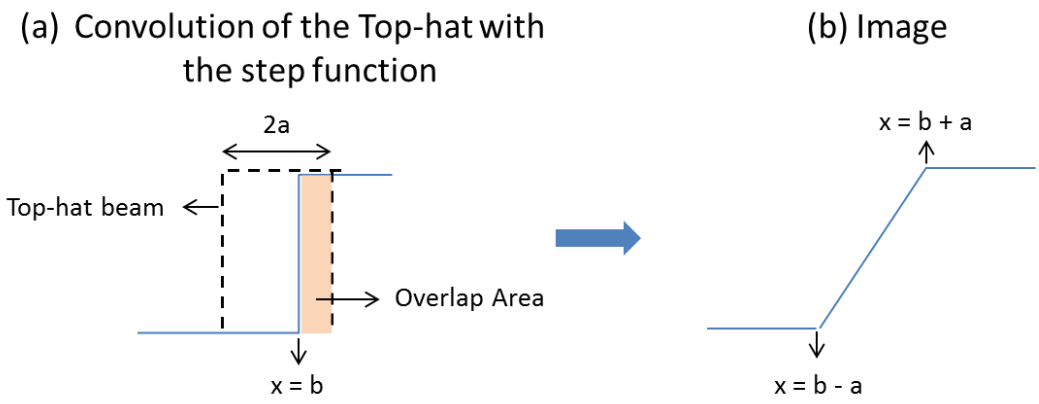

Figure 2.4. (a) Convolution of a Top-hat beam of width *2a* with a step function as described by eq 2.1. The Top-hat beam of width designated by the dashed black lines moves along the x-axis. As the beam overlaps the step function, a positive signal is generated for the image. (b) The image function increases linearly once overlap begins with the step function, and then increases with position as the area of overlap continues to increase. It reaches a maximum value that no longer changes when the beam completely overlaps the step function.

For beam distributions that are not uniform, a point-spread-function can be defined that is synonymous with a probability density function for the beam intensity with position. The point-spread-function for a Gaussian beam is given by eq 2.3:

$$PSF(x) = \frac{1}{\sigma\sqrt{2\pi}} e^{-\left(\frac{x^2}{2\sigma^2}\right)} \tag{2.3}$$

where σ represents the width of the Gaussian beam. The image intensity at a given location (x') can be computed by integrating the product of the object pattern, *o(x)*, and the PSF in the x-dimension:

$$i(x') = \int_{-\infty}^{+\infty} o(x)PSF(x - x')dx \tag{2.4}$$

For the step function defined by eq 2.1, since *o(x) = 1* for $x > b$, this integral in eq 2.4 could be simplified as:

$$i(x') = \int_b^{\infty} PSF(x - x')dx = \frac{1}{\sigma\sqrt{2\pi}} \int_b^{\infty} e^{-\left(\frac{x^2}{2\sigma^2}\right)} dx \quad (2.5)$$

Using the integral relationship $\int_0^x e^{-t^2} dt = \frac{\sqrt{\pi}}{2} \text{erf}(x)$, eq 2.5 can be recast as

$$i(x') = \frac{1}{2}\left[[1 + \text{erf}\left(\frac{x' - b}{\sqrt{2}\sigma}\right)\right] \quad (2.6)$$

For a Lorentzian profile, its PSF is given by

$$PSF(x) = \frac{1}{\pi\gamma\left[1+\left(\frac{x}{\gamma}\right)^2\right]} \quad (2.7)$$

Inserting this PSF into eq 2.4 yields the following image function for a Lorentzian beam over a step edge:

$$i(x') = \int_b^{\infty} PSF(x - x')dx = \frac{1}{\pi\gamma} \int_b^{\infty} \frac{1}{\left[1+\left(\frac{x-x'}{\gamma}\right)^2\right]} dx \quad (2.8)$$

Using the integral relationship: $\int \frac{dx}{1+x^2} = arctanx + C$, eq 2.8 can be written as:

$$i(x') = \frac{1}{\pi} \arctan\left(\frac{x' - b}{\gamma}\right) + \frac{1}{2} \quad (2.9)$$

For the case in eq 2.9 where $b = 0$, the image for a Lorentzian beam profile over a step function is illustrated by the cumulative density function shown in Figure 2.3.

2.4. Convolution of Two-dimensional PSF with a Step Function

In the previous section, derivations of the image functions for three different one-dimensional PSFs and a step function were developed. In this section, I extend this discussion to derive the image functions for various two-dimensional PSFs and a step function.

The molecular ion image obtained from an object in MALDI-IMS can be represented as the convolution between the pattern for the object and beam profile represented by the point spread function (PSF). Mathematically, a convolution can be expressed as

$$i(x', y') = o(x, y) \otimes PSF(x - x', y - y') \tag{2.10}$$

where $i(x', y')$ represents the image intensity at each specified beam location (x', y'), $o(x, y)$ describes the object pattern in a 2D plane, and $PSF(x - x', y - y')$ describes the beam profile in a 2D plane with its center point at (x', y'). The operator $\otimes$ denotes the convolution between these two functions. As the image intensity at a given location (x', y') can be computed by integrating the product of the object pattern and the PSF in the x- and y- dimensions, eq 2.10 can be rewritten as

$$i(x', y') = \int_{-\infty}^{+\infty} \int_{-\infty}^{+\infty} o(x, y) PSF(x - x', y - y') dx dy \tag{2.11}$$

Eq 2.11 provides a general method for determining an image function from a known PSF and an object function. This approach is general and does not assume a specific beam profile or a particular object pattern. In the following discussion, eq 2.11 is applied to determine the two-dimensional image functions for various model beam profiles and a step function.

Top-hat Beam Profile

A two-dimensional Top-hat profile represents a circular region with a uniform intensity distribution. An illustration of a Top-hat beam is shown in Figure 2.5a. Its PSF is given by:

$$PSF(x, y) = I \quad for\ x^2 + y^2 < a^2 \tag{2.12}$$

where a is the beam radius for a normalized PSF, $I = \frac{1}{\pi a^2}$. The variation in beam intensity in one direction can be expressed by a line spread function (LSF) that represents the convolution of the PSF with an infinitely narrow line:

$$LSF(x) = \int_{-\infty}^{\infty}\int_{-\infty}^{\infty} PSF(x,y)\delta(x-x')dx'dy = \int_{-\infty}^{\infty} PSF(x,y)dy = \frac{2}{\pi}\sqrt{a^2-x^2} \tag{2.13}$$

With this LSF, the image function expressing the two-dimensional result for a Top-hat beam profile and an object described by a step function in one direction can be calculated as follows:

$$i(x',y') = \int_{-a}^{x} \frac{2}{\pi}\sqrt{a^2-x^2}\,dx \tag{2.14}$$

$$= \frac{1}{\pi}\left[x\sqrt{a^2-x^2} + a^2 tan^{-1}\left(\frac{x}{\sqrt{a^2-x^2}}\right)\right]_{-a}^{x}$$

$$= \frac{1}{\pi}\left[x\sqrt{a^2-x^2} + a^2 tan^{-1}\left(\frac{x}{\sqrt{a^2-x^2}}\right)\right] + \frac{a^2}{2}$$

$$= \frac{1}{\pi}\left[x\sqrt{a^2-x^2} + a^2 sin^{-1}\left(\frac{x}{a}\right)\right] + \frac{a^2}{2} \tag{2.15}$$

The functions expressed by eq 2.12, 2.13, and 2.15 are illustrated in Figure 2.5 which displays the Top-hat beam profile, its LSF, which is obtained by integrating along one dimension, and its image function across a step function which is obtained by integrating the LSF along the second dimension.

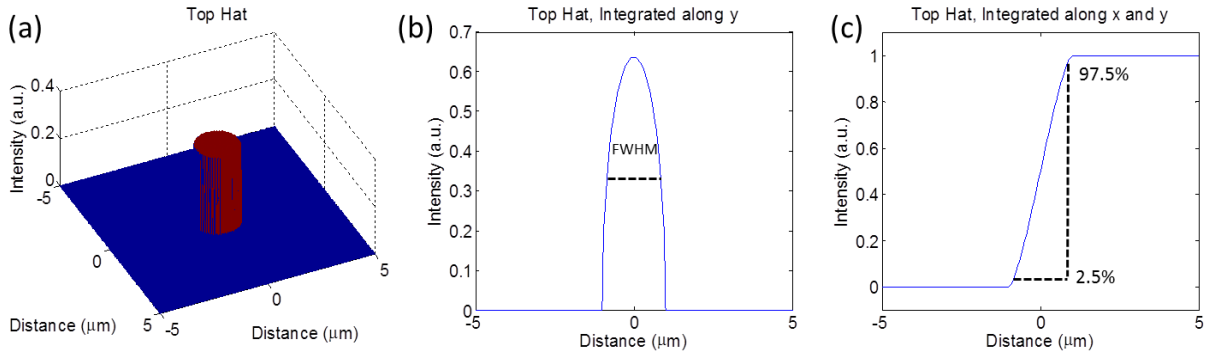

Figure 2.5. (a) A two-dimensional Top-hat beam with radius set to 1 μm and intensity 1/π. (b) The Top-hat beam with intensity integrated in the y-direction results in the shown line-spread function. (c) The intensity of the Top-hat profile is integrated along x and y generating the image function for the convolution of a step function and the Top-hat beam.

Gaussian Beam Profile

For a two-dimensional Gaussian-shaped beam, its PSF is represented as

$$PSF(x-x', y-y') = \frac{1}{\sigma_x \sigma_y 2\pi} e^{-\left(\frac{(x-x')^2}{2\sigma_x{}^2} + \frac{(y-y')^2}{2\sigma_y{}^2}\right)} \tag{2.16}$$

where x' and y' are the center locations of the beam, and σ_x and σ_y are characteristic widths of the beam in the x- and y- dimensions, respectively. For a circular beam, σ_x and σ_y are equal, and for an elliptical beam, σ_x and σ_y have different values.

For a 2-D pattern consisting of a sharp edge that extends in the y-direction, the object pattern can be described in the orthogonal x-direction by the step function

$$\begin{aligned} o &= 0 \quad for\ x < b \\ o &= 1 \quad for\ x \geq b \end{aligned} \tag{2.17}$$

where b represents the boundary where the value for the object changes abruptly from 0 to 1. For imaging such an object pattern with a Gaussian beam, the image function can be expressed based on eq 2.11 as

$$i(x', y') = \int_{-\infty}^{\infty}\int_{b}^{\infty} \frac{1}{\sigma^2 2\pi}\, e^{-\left(\frac{(x-x')^2}{2\sigma_x{}^2}+\frac{(y-y')^2}{2\sigma_y{}^2}\right)} dx\, dy \tag{2.18}$$

Separation of variables yields

$$i(x', y') = \frac{1}{\sigma_x \sigma_y 2\pi} \int_{b}^{\infty} e^{-\frac{(x-x')^2}{2\sigma_x{}^2}} dx \int_{-\infty}^{\infty} e^{-\frac{(y-y')^2}{2\sigma_y{}^2}} dy \tag{2.19}$$

Simplification using the substitutions $g = \frac{y-y'}{\sqrt{2}\sigma_y}$, $\frac{dg}{dy} = \frac{1}{\sqrt{2}\sigma_y}$, and $dy = \sqrt{2}\sigma_y dg$ leads to the expression

$$i(x', y') = \frac{1}{\sigma_x \sigma_y 2\pi} \int_{b}^{\infty} e^{-\frac{(x-x')^2}{2\sigma_x{}^2}} dx \int_{-\infty}^{\infty} e^{-g^2} \sqrt{2}\sigma_y dg \tag{2.20}$$

that using the integration relationship $erf(x) = \frac{2}{\sqrt{\pi}}\int_0^x e^{-t^2}\, dt$ allows the image function to be expressed as

$$i(x', y') = \frac{1}{\sigma_x \sigma_y 2\pi} \int_{b}^{\infty} e^{-\frac{(x-x')^2}{2\sigma_x{}^2}} dx \left[\frac{\sqrt{\pi}\sigma_y}{\sqrt{2}} \mathrm{erf}(g)\right]_{-\infty}^{\infty} \tag{2.21}$$

As $= 2$,

$$i(x', y') = \frac{1}{\sigma_x \sqrt{2\pi}} \int_{b}^{\infty} e^{-\frac{(x-x')^2}{2\sigma_x{}^2}} dx \tag{2.22}$$

which provides an expression for the LSF of the two-dimensional Gaussian profiles as

$$LSF = \frac{1}{\sigma_x \sqrt{2\pi}} e^{-\frac{(x-x')^2}{2\sigma_x{}^2}} \tag{2.23}$$

since eq 2.22 includes the integral of the PSF in the y-direction which is equivalent to the LSF. A plot of the LSF for a two-dimensional Gaussian beam is shown in Figure 2.6b, which is equivalent to the profile for a one-dimensional Gaussian beam.

To determine an explicit expression for the image function for a two-dimensional Gaussian beam over a step function, eq 2.22 is recast using the substitutions of $h = \frac{x - x'}{\sqrt{2}\sigma_x}$, $\frac{dh}{dx} = \frac{1}{\sqrt{2}\sigma_x}$, and $dx = \sqrt{2}\sigma_x dh$ to yield

$$i(x', y') = \frac{1}{\sigma_x\sqrt{2\pi}} \int_{\frac{b - x'}{\sqrt{2}\sigma_x}}^{\infty} e^{-h^2} \sqrt{2}\sigma_x dh \tag{2.24}$$

Using the integration relationship $erf(x) = \frac{2}{\sqrt{\pi}} \int_0^x e^{-x^2}\, dx$,

$$i(x', y') = \frac{1}{\sigma_x\sqrt{2\pi}} \left[\frac{\sqrt{\pi}\sigma_x}{\sqrt{2}} \operatorname{erf}(h)\right]_{\frac{b - x'}{\sqrt{2}\sigma_x}}^{\infty} \tag{2.25}$$

which yields

$$i(x', y') = \frac{1}{2}\left(1 + \operatorname{erf}\left(\frac{x' - b}{\sqrt{2}\sigma_x}\right)\right) \tag{2.26}$$

to provide the image function shown in Figure 2.6c for the convolution of a two-dimensional Gaussian beam and a step function. The FWHM in this expression is the same as that for one-dimensional Gaussian function.

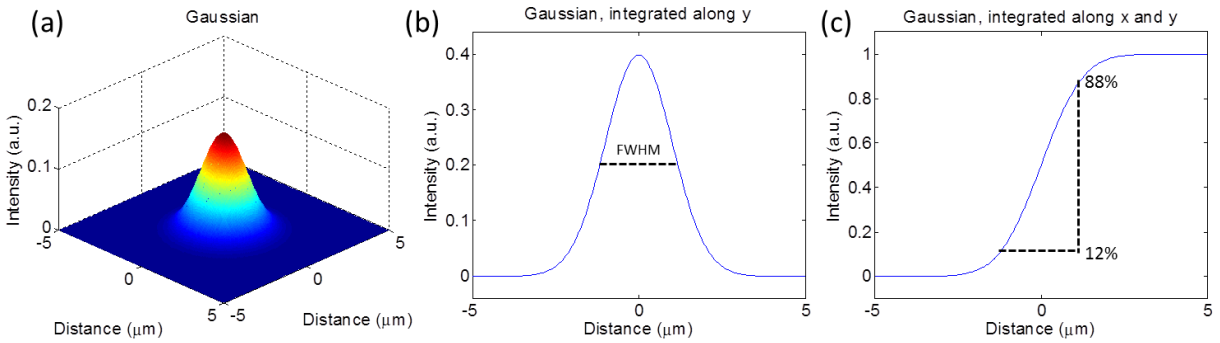

Figure 2.6. (a) A two-dimensional Gaussian beam with σ set to 1. (b) The Gaussian beam integrated along the y-direction generates the shown LSF. (c) The Gaussian beam with intensity integrated in both the x and y directions generates an image function for the convolution of the Gaussian beam with a step function.

Lorentzian Beam Profile

As a two-dimensional Lorentzian profile cannot be integrated in two-dimensions to give a finite value, a corresponding image function cannot be obtained for this profile by the approach detailed above. In imaging, the Lorentzian function has utility in modelling lens aberration and/or particle scattering within a sample. While an evaluation of the effects of a two-dimensional Lorentzian profile on an image function could be done by excluding intensity from the beam below a certain threshold, this analysis was not pursued due to the uncertainty in selecting an appropriate threshold.

2.5. Convolution of Two-dimensional PSF with Custom Objects

In the previous sections, a simple step function was used as an object to be imaged. For an object that is not as easily defined as a step function, it is not always possible to obtain a mathematical solution for its image function. In such cases, a numerical method can be used to produce the corresponding image function. It is worth noting that analytically derived mathematical solutions assume infinitesimally small step sizes in their derivation. As such, they

do not include the effects that step size or sampling frequency can have on the spatial resolution in the actual image. To include these factors, a numerical model was developed to examine the effects of step size and beam size on spatial resolution.

To illustrate these effects, a considered test object is shown in Figure 2.7. The object is the letter F drawn on a 2-D plane with 10 x 10 blocks. Each block is a square of dimensions 100 µm x 100 µm. The red color represents the intensity of 1, and the blue color represents the intensity of 0.

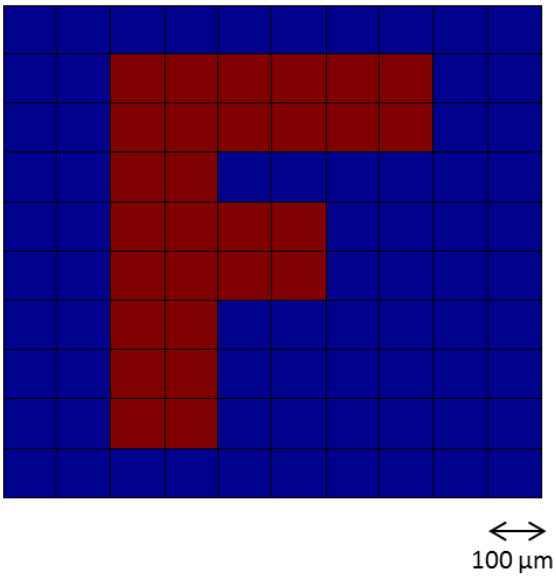

Figure 2.7. A test object consisting of the letter F drawn on 1 mm x 1 mm field. The red color represents the intensity of 1, and the blue color represents the intensity of 0.

Figure 2.8 displays the results from a numerical simulation where the test object in Figure 2.7 was convoluted with a Gaussian beam (refer to Appendix B for the employed MATLAB code) where both σ_x and σ_y were set to 5 µm. The images were obtained using step sizes of 5, 10, 25, and 50 µm. In the figure, the effect of step size on the resolution is evident with the edges of the pattern being defined in their width by the increasing step sizes. Further, the fraction of the

total pixels that represent regions of full (red) or no (blue) intensity decreases as the step size is increased, denoting a loss in spatial resolution.

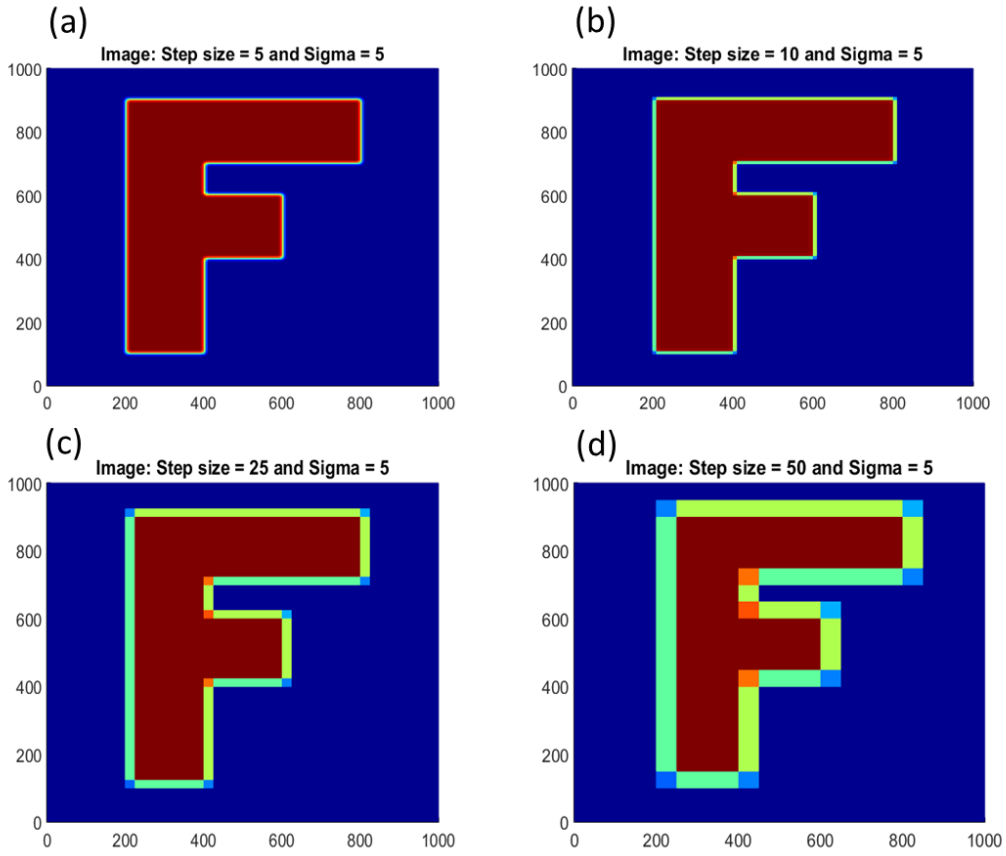

Figure 2.8. Images of the test object in Figure 2.7 acquired at step sizes of 5, 10, 25, and 50 μm. The images were calculated by convoluting the Gaussian beam with the object. The beam width, σ, was held fixed at 5 μm.

In the second set of simulated images, the step size was held constant at 5 μm and σ was varied from 1 to 25 μm. Figure 2.9 displays the results where a loss of spatial resolution is apparent with increases in σ. In these images, the edges are blurred when σ is greater than the step size. For values of σ less than half the step size (not shown), the images were similar in appearance. These results illustrate the degree that the spatial resolution in an image is influenced by both σ and step size to the extent that one factor may have a dominant effect.

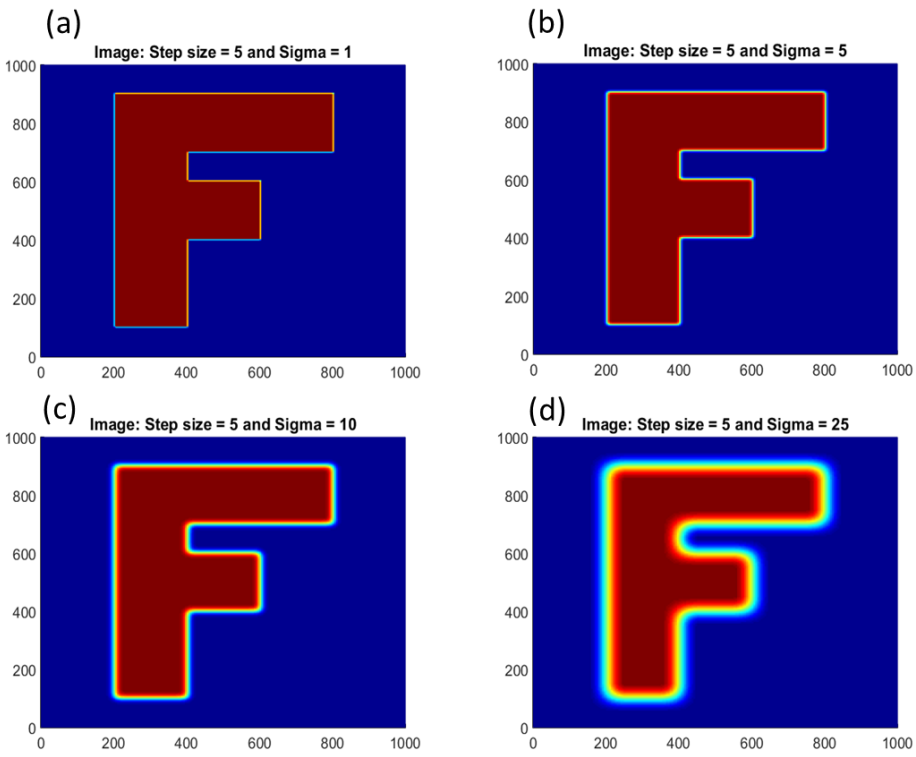

Figure 2.9. Images of the test object in Figure 2.7 acquired at σ values of 1, 5, 10, and 25 μm. The step size was held fixed at 5 μm. The images were calculated by convoluting the Gaussian beam with the object.

2.6. Defining a Resolution Criterion

While the blurring induced by step size and beam size is visually apparent in Figures 2.8 and 2.9, a method is needed for providing a quantitative measurement of spatial resolution. In general, the spatial resolution in an image improves as the step size is decreased for a given beam diameter. However, diminishing improvements were observed if the step size is decreased to values below the beam size. In this section, the effects of beam size and step size on the spatial resolution are examined in more detail. Additionally, a criterion for defining spatial resolution in a manner that is compatible with the specific operating conditions of MALDI IMS is developed.

Before considering the specific case of MALDI-IMS, it is useful to consider how spatial resolution is defined for other techniques. In light and electron microscopy, a simple definition of spatial resolution is "the minimum spacing at which two features in an image can be recognized as distinct and separate.[34] Typically, a threshold must be set to give a sufficient degree of confidence in the identification of two objects as distinct. In optical microscopy, the Rayleigh criterion sets a resolution limit as corresponding to the separation between two equal point sources such that the maximum from one source falls on the minimum of the other. For this case, a dip is apparent in the summed image from these two sources (Figure 2.10). For comparison, the Abbe and Sparrow limits represent alternative definitions of the resolution limit where the region between the two sources in the summed image contains a small dip (Abbe) or a flat region (Sparrow). By these definitions, the Rayleigh limit assigns the spatial resolution with a highest value and the Sparrow limit with the lowest value for images of the same inherent spatial resolution. In other words, these methods each provide their own specific (albeit arbitrary) metric for defining spatial resolution. The limits for these three cases are shown in Figure 2.10.

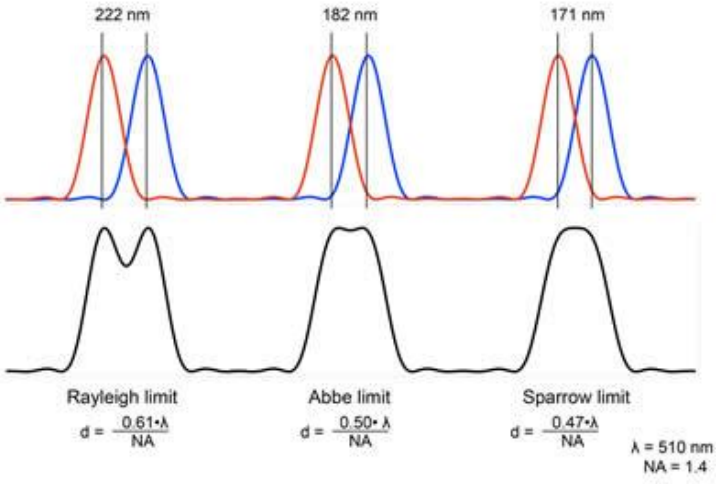

Figure 2.10. Various conventional resolution limits and their definitions. In the Rayleigh criterion, the first minimum of one Airy profile overlaps the maximum of a second Airy profile, with the sum of the two profiles showing a distinct dip. In the Abbe limit, a small dip is still

discernible between the two maxima. In the Sparrow criterion, the sum of the two Airy patterns produces a flat intensity profile. This figure is adapted from an advanced microscopy guide from the University of Utah.

The Rayleigh, Abbe, and Sparrow limits provide useful theoretical constructs for defining spatial resolution, but they do not factor in experimental conditions such as noise and sampling frequency that complicate their direct use. As an alternative, a modulation transfer function (MTF) has been used to establish a resolution criterion.[35] In this method, contrast is calculated by the expression

$$C = \frac{I_{max} - I_{min}}{I_{max} + I_{min}} \tag{2.27}$$

where I_{min} and I_{max} represent minimum and maximum intensities, respectively. The ratio of the contrast in an image relative to the contrast for the object is known as a modulation transfer function

$$MTF(f) = \frac{C_{image}(f)}{C_{object}(f)} \tag{2.22}$$

where *f* represents the spatial frequency. For test patterns, the object is assumed to have perfect contrast, that is, $C_{object} = 1$. In eq 2.22, the contrast for an image is dependent on the spatial frequency of the pattern. As the spatial frequency increases (i.e., the pattern element are repeated more frequently in a define spatial region), the contrast of an image decreases. The MTF represents the quality of transfer from the object to the image. A MTF value of 1 implies perfect image quality whereas lower values of MTF represents greater losses in spatial information.

The MTF requires the determination of differences in the maximum and minimum intensities. In applying this approach to experimental MALDI-IMS results, I observed that there

was a greater degree of variability in the maximum MS signal from regions that should give a common full value than from blank regions that should give a common zero value. Due to the greater differences from these former regions, a method whereby changes in the minimum intensity are used for the evaluation of spatial resolution would be more reliable. Figure 2.11 shows a developed approach detailed later in the thesis where the resolution criterion on the gap between two patterned regions was defined at 10% of the maximum signal. If the signal in the 'empty regions' exceeded more than 10% of the maximum signal, then the resolution limit at that gap-size was not satisfied (shown in red in the figure as not resolved). If the signal in the empty regions was consistently below the threshold (as shown in green in the figure), those gaps are said to be resolved. By this approach, a designation of the achieved spatial resolution was straightforward, in contrast with the MTF approach that required an evaluation at each spatial frequency. I note that the method illustrated in Figure 2.11 assumes nothing about shape of the beam profile. As such, the generality of the approach allows its application to any beam profile including those that are irregularly shaped as demonstrated later in the thesis.

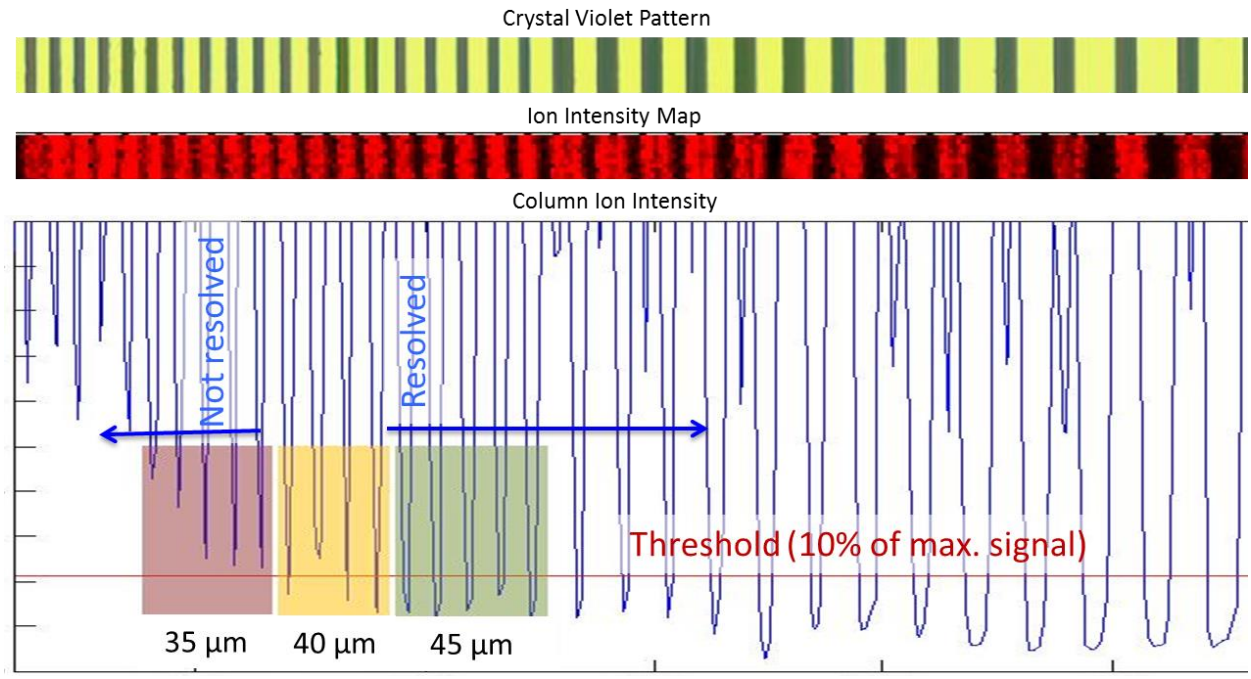

Figure 2.11. A schematic definition of the resolution threshold. Here, the valleys in the MS signal corresponding to the gaps between crystal violet lines must dip below a specified threshold set at 10% of the maximum signal for the resolution limit to be satisfied. In contrast, if the valleys do not consistently dip below the threshold, the corresponding gaps are considered not resolved. Here, gaps of dimension 45 µm and above are resolved.

For the approach shown in Figure 2.11 for determining spatial resolution, its measurement of spatial resolution may be influenced by the width of the lines that sandwich a gap of a specific size. To address this issue, signal data were computed for a pattern of lines with gap distances varying from 1 to 30 µm and differing in the widths of the lines. Specifically, the image signals were computed for patterns of lines where the gaps between the lines were twice, equal to, or one half the widths of the lines. In all three cases, both the beam width and the step size were maintained at 5 µm. Figure 2.12 summarizes these results showing that the measurement of spatial resolution by this approach was unaffected by the width of the lines. Specifically, the resolved gap size was similar (19 or 20 µm) in all three cases, where the line width for the condition where the resolution threshold was achieved ranged from 10 to 38 µm.

For assessing a threshold where a minimum value is achieved, the gap size is the most important factor for this approach.

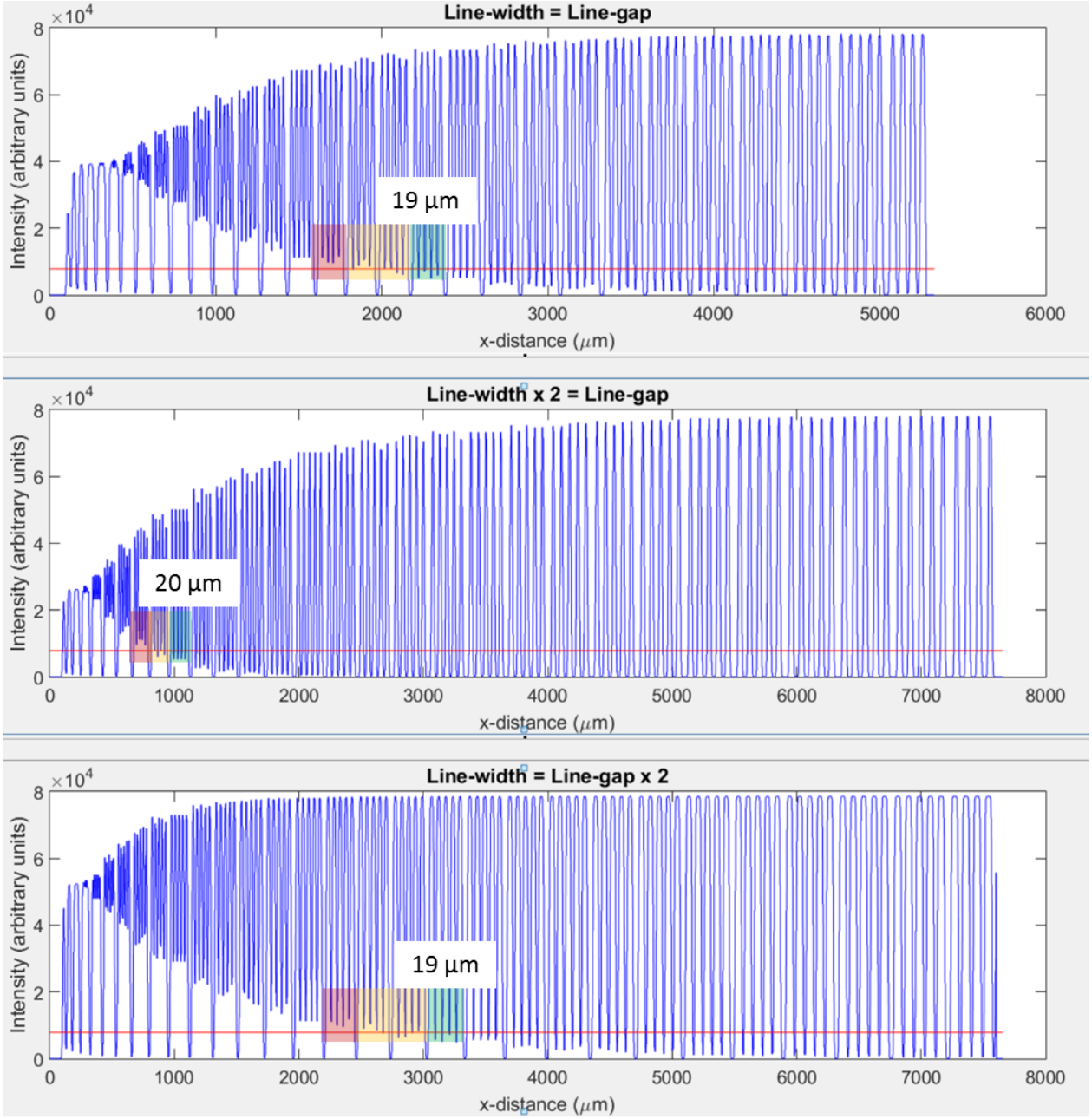

Figure 2.12. The effect of the ratio of line-width to line-gap on the measurement of spatial resolution using a 10% threshold of maximum signal. The ratio between these two features of the lines had little influence on the measurement of spatial resolution as the measured spatial resolution was 19-20 µm in all three cases.

In MALDI-IMS, step size and beam size both impact the spatial resolution in an image as illustrated in Figures 2.8 and 2.9. To explore their effects in greater detail, simulated ion images were generated for various combinations of step sizes and beam sizes, and the spatial resolutions for these conditions were determined. Before conducting these simulations, a test object was designed where the gap between parallel lines was gradually increased from 1 µm to 100 µm as shown in Figure 2.13. A common structural pattern consisting of five parallel lines for each gap size formed a repeating feature in the test object, albeit of different sizes. Among each set of five lines, their widths were equal to the spacing between them. A larger gap was used to separate adjacent sets of lines to aid in distinguishing one set from another. The first region consisted of lines with widths and gaps from 1 to 10 µm in size increasing in 1 µm increments. The second region consisted of a similar arrangement with 10 to 50 µm features increasing in 2 µm increments. The third region consisted of features 50 to 100 µm in size increasing in 5 µm increments. In each of these regions, the employed patttern consisting of five lines (and four gaps) allowed multiple tests at each gap size as way to provide increased confidence in the determination of spatial resolution.

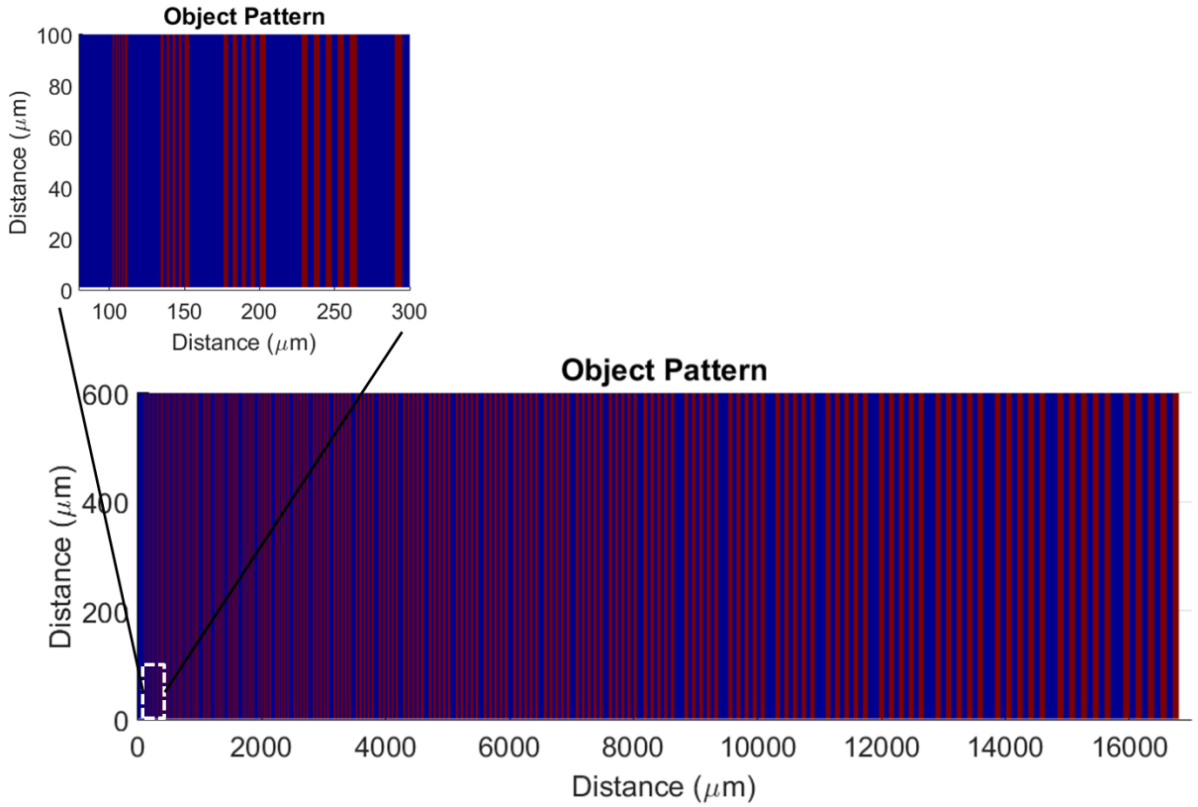

Figure 2.13. A test object pattern used to assess spatial resolution for various combinations of step sizes and beam sizes. The red color represents the intensity of 1 and the blue color represents the intensity of 0. The line-widths range from 1 to 100 μm. The pattern contains five sets of replicate lines for a given line-width. The spacing between the adjacent lines is equal to their line-width. The spacing between the sets of five lines is 25 μm for features ≤ 10 μm, 50 μm for features between 10 and 50 μm, and 100 μm for features > 50 μm .

The object pattern in Figure 2.13 was convoluted with a Gaussian beam of constant σ = 5 μm using different step sizes. Simulated images were obtained using step sizes of 5, 10, 15, 20, 25, and 50 μm that are presented below. For the 5 and 10 μm step sizes, the smallest interval that was consistently resolved was 20 μm (Figure 2.14) with the 18 μm gap being resolved occasionally. That the obtained spatial resolutions were the same for both cases suggests that its value is limited by the beam size in these two simulations. For comparison, the beam diameter that encloses 90% of the area under the PSF curve is called the 90% signal width. For a beam with σ = 5 μm, the 90% signal width is 16.5 μm. This value represents the theoretical limit for

the spatial resolution of a Gaussian beam with σ = 5 µm using a 10% threshold assuming an infinitely small step size. The results in Figure 2.14 compare favorably with this value.

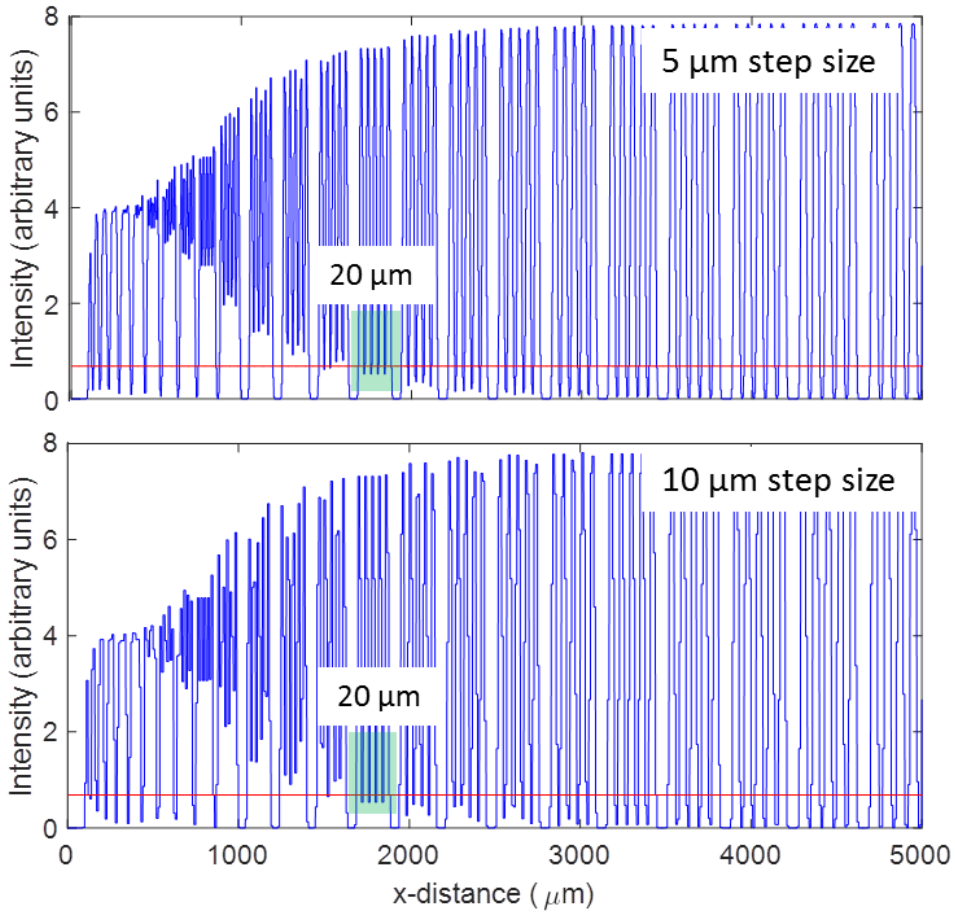

Figure 2.14. Linescans across the test object in Figure 2.13 for 5 and 10 µm step sizes with a constant σ of 5 µm. Spatial resolution is measured to be 20 µm in both cases.

Above a 10 µm step size, the measured resolution increased above the 20 µm value obtained using smaller step sizes. With the 15 and 20 µm step sizes, the line scans showed a regular transition from displaying minimum values below the 10% threshold on large gap sizes to displaying minimum values close to half intensity on the smaller gap sizes. With the 25 µm step size, the signal was less well defined, particularly across the smaller gap sizes (Figure 2.15). Despite this difference in appearance, the criterion of a consistent achievement of a signal below

the threshold value could be used and the spatial resolution was measured to be 38 μm. As the step sizes were increased above 25 μm with the beam width held constant, the measured values of the spatial resolution at these conditions approached those of the step size. Table 2-2 summarizes the spatial resolution results obtained from the simulations using the test object in Figure 2.13 for the six step sizes.

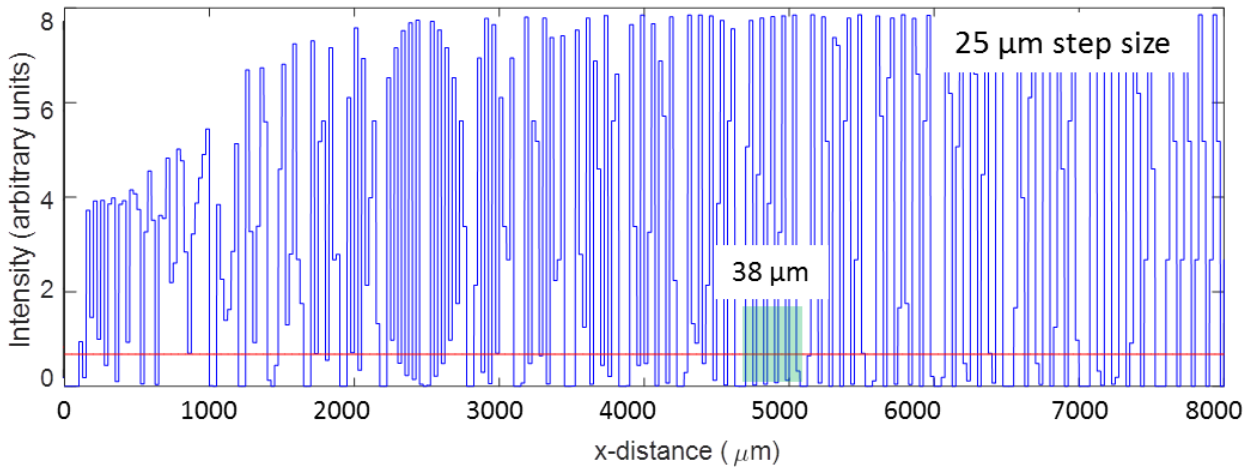

Figure 2.15. Linescan across the test object in Figure 2.13 at a 25 μm step size with σ = 5 μm. Spatial resolution was measured to be 38 μm. The line scan is less defined that are those in Figure 2.14 obtained using a smaller step size.

Table 2-2. Spatial resolution obtained using the method outlined in Figure 2.11 and the test object in Figure 2.13 as a function of step size for a Gaussian beam of constant width σ = 5 μm, a corresponding FWHM of 11.8 μm, and a 90% signal width of 16.5 μm.

Step Size (μm)	**Resolution (μm)**
5	20
10	20
15	26
20	30
25	38
50	60

In a second set of simulations using the test object in Figure 2.13, a value of σ of 10 μm was employed with step sizes having values of 5, 10, 15, 20, 25, and 50 μm. For these conditions, the theoretical minimum resolution for a Gaussian beam with σ = 10 μm would be 32.9 μm based on its 90% signal width. Figure 2.16 shows the results for selected step sizes. For a 5 μm step size, the smallest interval to be resolved was 36 μm, which was close to the expected theoretical limit of 32.9 μm. At a 10 μm step side, the smallest interval resolved consistently increased slightly to 40 μm. The shapes of the two line scans appeared similar and well-defined. In constrast, at a 50 μm step size, the signal appeared less regular suggesting complete loss of spatial information for small feature sizes (Figure 2.17). For regions where the step size was larger than the feature size, this irregularity in the signal is to be expected as the sampling is less arbitrary and may be periodic with the spacing of the pattern. Despite these issues, the criterion of a consistent achievement of a signal below the threshold value still applied. Table 2-3

summarizes the spatial resolution results obtained from these simulations using the test object in Figure 2.13 for the six step sizes and σ = 10 µm.

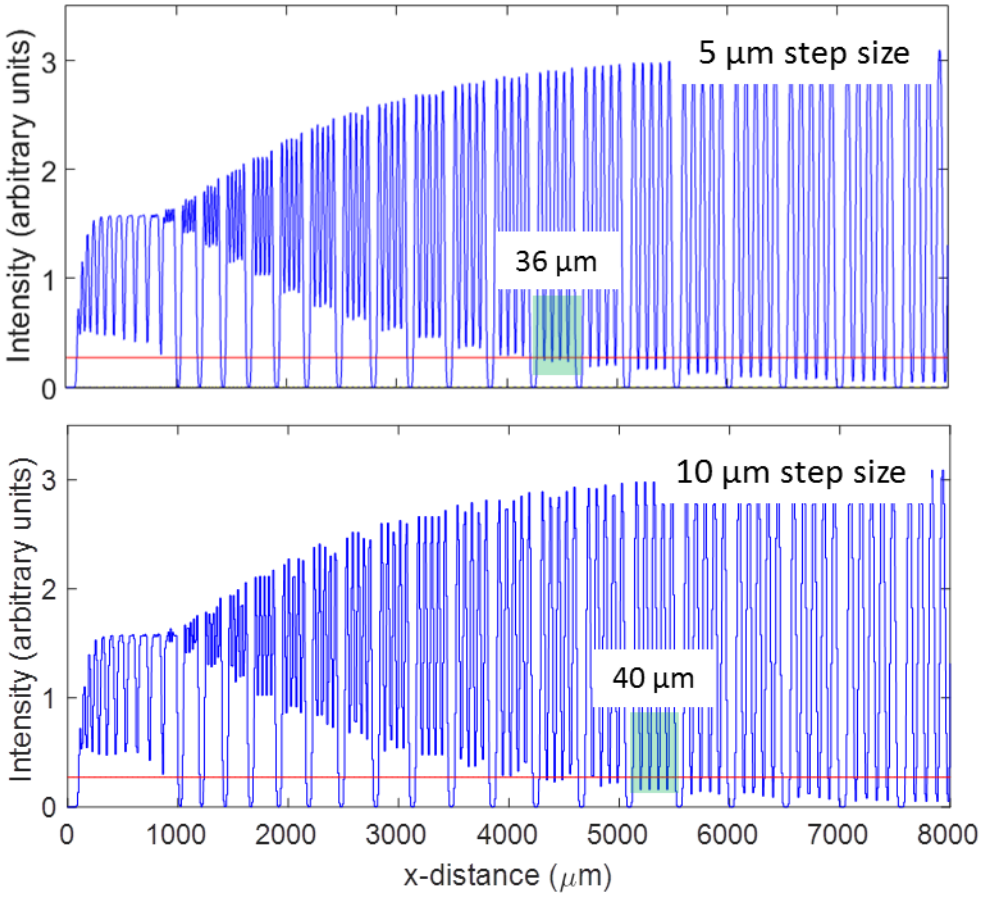

Figure 2.16. Simulated scan lines for the test object in Figure 2.13 obtained using step sizes of 5 and 10 µm and a constant σ of 10 µm. Spatial resolutions were measured to be 36 and 40 µm, respectively.

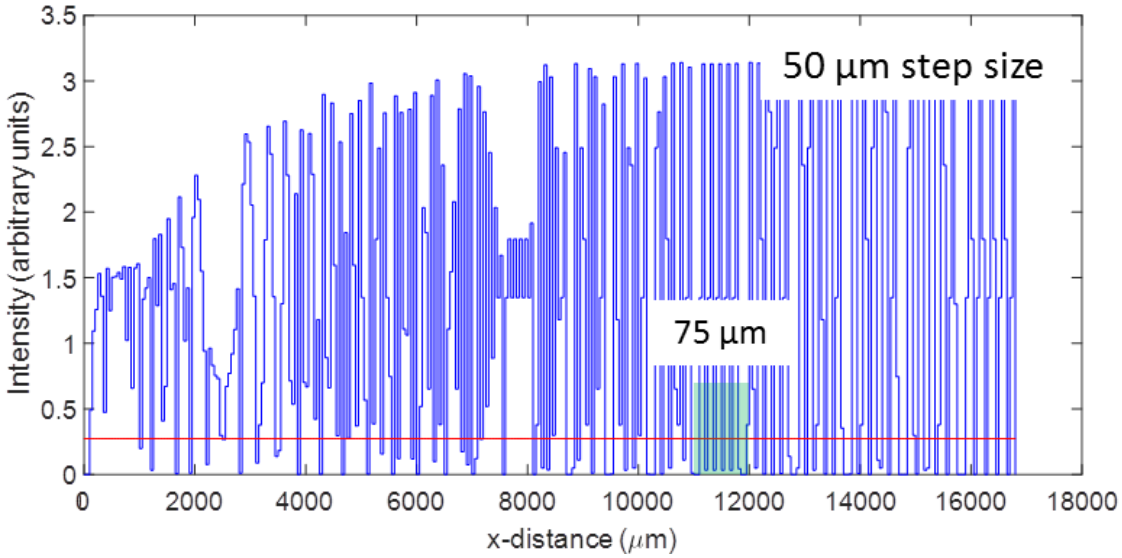

Figure 2.17. Simulated scan lines for the test object in Figure 2.13 obtained using a step size of 50 µm and a σ of 10 µm. Spatial resolutions was measured to be 75 µm.

Table 2-3. Spatial resolution obtained using the method outlined in Figure 2.11 and the test object in Figure 2.13 as a function of step size for a Gaussian beam of width σ = 10 µm, a corresponding FWHM of 23.5 µm, and a 90% signal width of 32.9 µm.

Step Size (µm)	**Resolution (µm)**
5	36
10	40
15	42
20	44
25	50
50	75

In a third set of simulations using the test object in Figure 2.13, a value σ of 20 µm was employed, with step sizes having values of 5, 10, 15, 20, 25, and 50,µm. In this case, the theoretical minimum resolution is 65.8 µm as calculated by the 90% signal width for a Gaussian

beam with σ = 20 μm. Figure 2.18 shows the results for a selection of these step sizes. With step sizes ranging from 5 to 20 μm, the smallest gap in the pattern that was consistently resolved was 70 μm, which is close to the theoretical limit of 65.8 μm based on its 90% signal width. With the 50 μm step size, the shape of the signal was less defined than with the smaller step sizes as observed in the earlier figures and simulations under related conditions. A resolution limit of 100 μm was obtained with the 50 μm step size. Table 2-4 summarizes the spatial resolution results obtained from these simulations for the six step sizes.

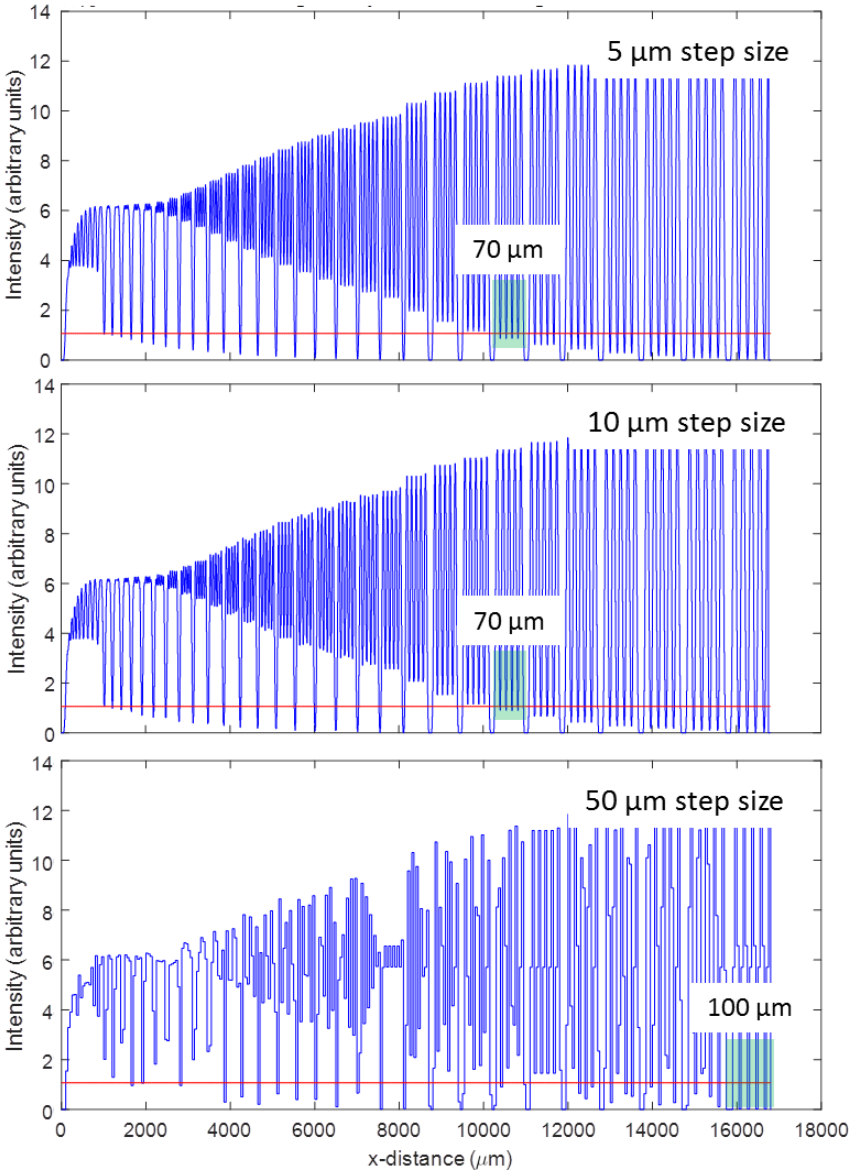

Figure 2.18. Simulated scan lines for the test object in Figure 2.13 obtained using step sizes of 5, 10, and 50 µm and a constant σ of 10 µm. Spatial resolutions were measured to be 70, 70 and 100 µm, respectively.

Table 2-4. Spatial resolution obtained using the method outlined in Figure 2.11 and the test object in Figure 2.13 as a function of step size for a Gaussian beam of width σ = 20 μm, a corresponding FWHM of 47.1 μm, and a 90% signal of 65.8 μm.

Step Size (μm)	**Resolution (μm)**
5	70
10	70
15	70
20	70
25	75
50	100

Figure 2.19 summarizes the results of these three sets of simulations examining the effects of beam width and step size on spatial resolution. In the figure, the measured spatial resolution worsens as the step size or the beam size increases. At the smallest step sizes, the obtained measurements of spatial resolution were close to the values expected theoretically for these beam widths based on their 90% signal widths. Improvements in spatial resolution in Figure 2.19 were modest (or not observed) when the step size was reduced below values roughly twice that of σ. For MALDI-IMS, this observation implies that the optimal conditions with regard to image resolution and data acquisition are those where the step size has a value that is roughly two times σ. Image acquisition with step sizes below these values results in no (or little) improvement in actual spatial resolution. This suggests is that the additional instrument time and larger data files associated with the use of step sizes smaller than these values provide no (or little) benefit to spatial resolution in MALDI-IMS.

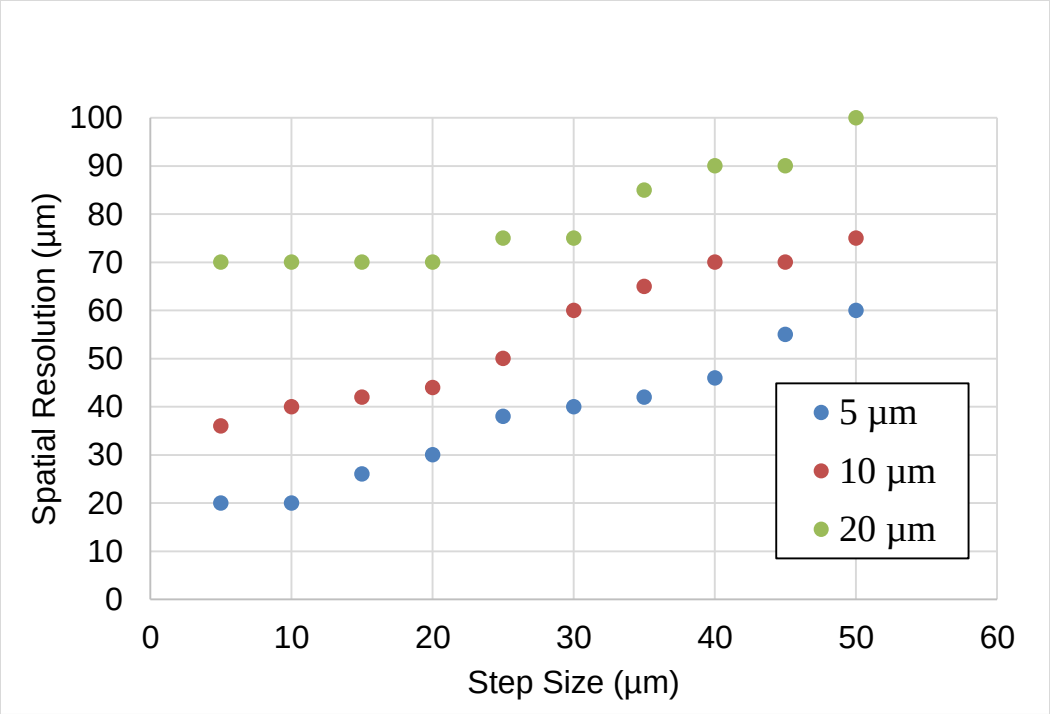

Figure 2.19. Spatial resolution as a function of step size and beam width (σ = 5, 10, and 20 µm) using simulated results for a Gaussian beam and the test object in Figure 2.13. Spatial resolution was determined using a threshold limit of 10% of maximum signal by the method detailed in Figure 2.11. Representative linescans are presented in Figures 2.14 to 2.18.

When the step size is must larger than the 90% beam width, the beam width can contribute significantly to the obtained spatial resolution. For example, with a step size of 50 µm, spatial resolution values of 100 µm to 60 µm were obtained for Gaussian beams of widths σ of 20 and 5 µm, respectively. The general trend is that the spatial resolution depends on both beam size and step size, with reductions in both offering improvements when step size is greater than 2 times σ. When the step size is greater than twice σ, the obtained spatial resolution in an image is roughly equal to the sum of the step size and twice the beam width σ for a Gaussian beam. For other beam shapes, a related relationship between spatial resolution, step size, and a characteristic beam width likely applies. The measurement of spatial resolution using the 10%

threshold provides a convenient approach for characterizing spatial resolution. A different threshold can be chosen to generate similar measurement depending on the application.

CHAPTER 3. FABRICATION OF A STANDARD RETICLE SLIDE FOR MALDI-IMS

Chapter 2 sets the theoretical definition for quantifying spatial resolution. Spatial resolution in MALDI imaging is a function of laser beam size and raster step size. The extent of blurring induced by the imaging device was quantified using the established criterion. In particular, two parameters affecting spatial resolution were investigated: the beam characteristics and step sizes in a 2D plane. The properties of the sample can also affect the measurement. In particular, the sample thickness can determine if the image was acquired in oversampling vs. overlapping mode and threshold ablation/ ionization energy can alter the effective beam size measurement. Experimental data must be acquired for a well-defined object to evaluate effective spatial resolution. In this chapter, I discuss the development of a well-defined pattern that is compatible with MALDI-IMS.

Patterned surfaces as resolution standards for imaging mass spectrometry have been developed by other researchers, particularly BAM-L200 by Senoner and Unger.[36] BAM-L200 consisted of 142 layers of AlGaAs-InGaAs-GaAs formed by metal organic vapor phase epitaxy (MOVPE) on a GaAs wafer substrate. This stack of layers was cross-sectioned and carefully polished to provide 23 gratings with graded periods between 2 and 600 nm. This object was subsequently used to assess spatial resolution in surface analysis techniques such as secondary ion mass spectrometry (SIMS). However, the metallic targets are not appropriate for MALDI IMS as the required power for ablation/ ionization is typically higher compared to that needed for organic substrates. Additionally, the size scale of 2 and 600 nm is too small for MALDI-IMS.

3.1. Design Requirements

At the outset, a list of design criteria for the materials and processes to be used in the construction of a reticle for MALDI-IMS was established. Their selection was based on a knowledge of the specific needs for MALDI-IMS and the likely best patterning approaches for generating usable features. The listed chemical attributes affect the choice of compound which influences the method of patterning that is required. Included:

a. A compound that can be easily seen using optical microscopy i.e. it is colored
b. A compound that is stable over time
c. A compound that is readily desorbed and ionized by a laser without requiring a MALDI matrix
d. A required laser energy for ablation and ionization that is similar to that typically used for investigations of biological tissues
e. A fabrication process that is inexpensive, rapid and amenable to being scaled up for high-throughput generation

3.2. Choice of Compounds for Reticle

Organic dyes were chosen to be readily visible under a microscope when cast as a thin film. A number of dyes were screened to identify those compounds that provided strong mass spectrometry signals with little fragmentation. Figures 3.1 and 3.2 provide the mass spectra and the chemical structures along with the mass spectra for the various candidate dyes that were explored. Figure 3.1 shows spectra for tris(8-hydroxyquinolinato)aluminum (Alq_3), laccaic acid A, and fast blue B salt. The spectra for these compounds do not show corresponding monoisotopic peaks suggesting fragmentation or molecular rearrangement in the gaseous phase.

Due to a lack of clean spectra, these compounds were deemed to be unsuitable for the reticle development. Figure 3.2 shows the spectra for copper (II) phthalocyanine, crystal violet, and rhodamine B. These compounds show clean spectra with peaks corresponding to the intact molecules. For copper (II) phthalocyanine, peaks were observed at 575 and 577 Da nominal masses corresponding to the ^{63}Cu and ^{65}Cu isotopes. For both crystal violet and rhodamine B, peaks were observed for their $[M - Cl^-]^+$ ions. Additionally, the power needed for ablation and ionization was similar to that used in a typical MALDI experiment.

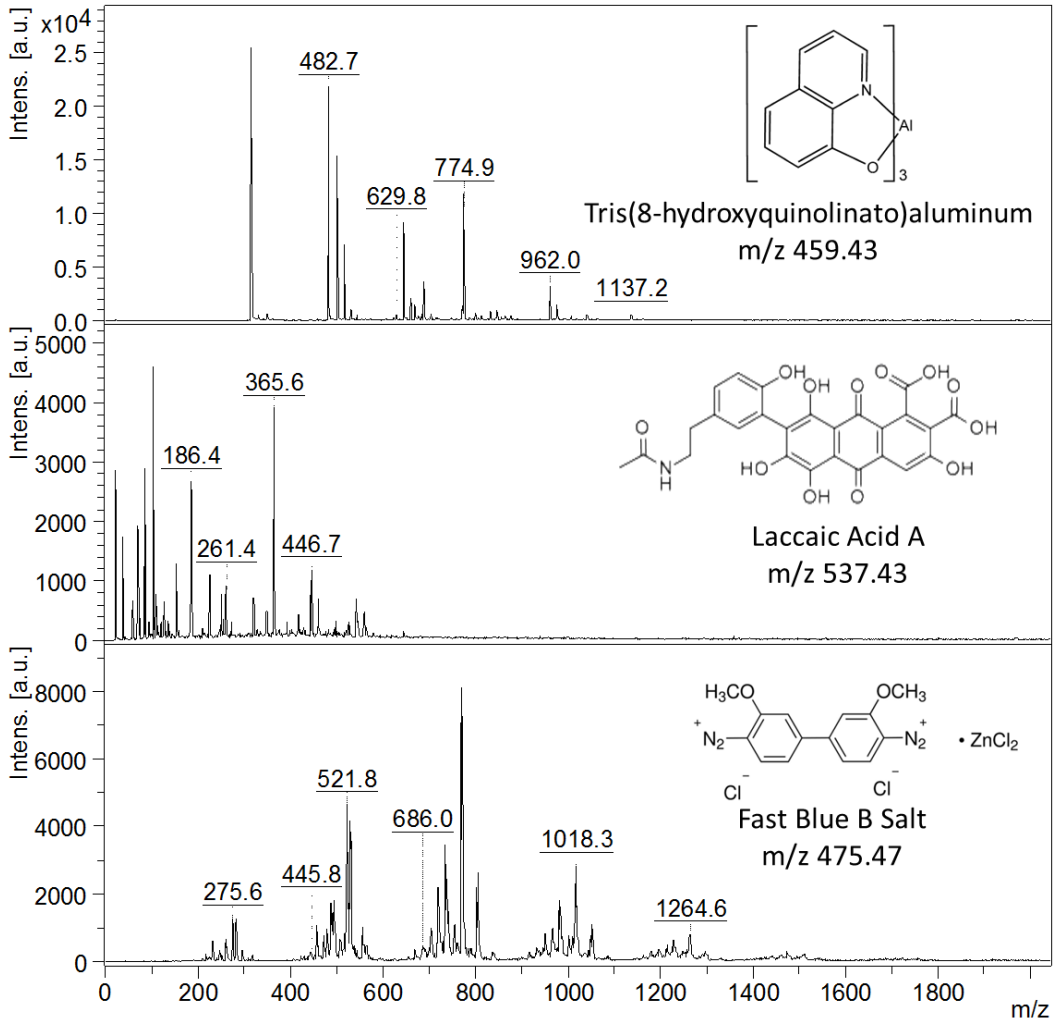

Figure 3.1. Mass spectra for tris(8-hydroxyquinolinato)-aluminum, laccaic acid A, and fast blue B salt. Laser power was 94%, 96%, and 89%, respectively. No intact molecules were observed suggesting that these molecules fragmented or rearranged in the gas phase.

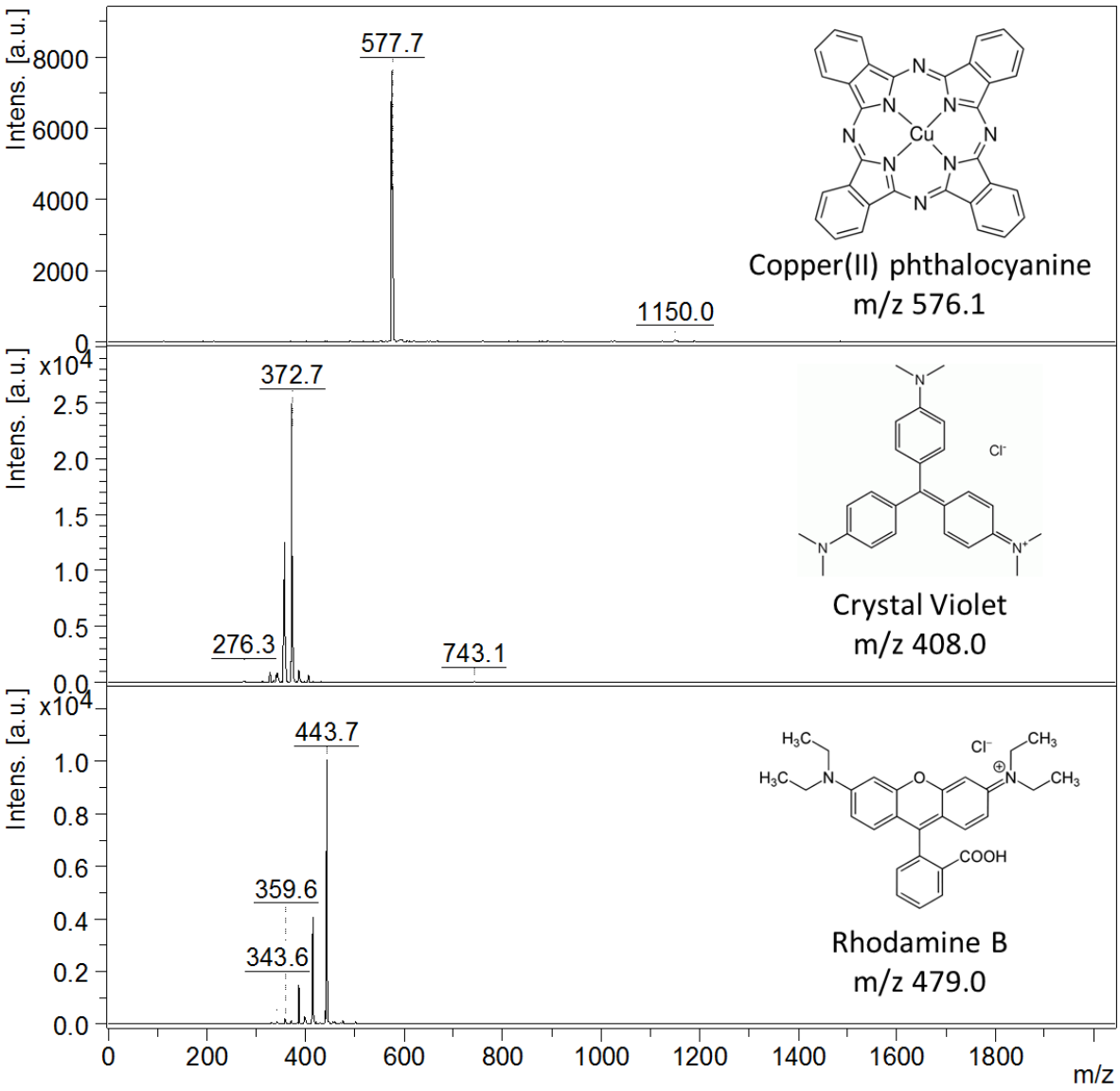

Figure 3.2. Mass spectra for copper (II) phthalocyanine, crystal violet, and rhodamine. For copper (II) phthalocyanine, two peaks are observed at nominal masses of 575 and 577 Da corresponding to ^{63}Cu and ^{65}Cu isotopes. For both crystal violet and rhodamine B, $[M - Cl^-]^+$ peaks are observed at m/z 372 and 443 Da, respectively.

3.3. Selection of Fabrication techniques

Many surface patterning approaches have been developed by the Whitesides group and others.[37] These patterning methods can be divided into those done in a top-down or bottom-up approach. Conventional top-down patterning methods include photolithography and scanning

beam lithography. These methods are encumbered by high capital costs and routine access to a clean-room facility, motivating the development of alternative approaches. Unconventional approaches for fabrication include both top-down and bottom-up approaches. Molding, embossing, and printing are primarily classified as top-down. Scanning probe lithography and self-assembly are classified as bottom-up even though they use templates that are typically fabricated by the top-down approaches.

Conventional photolithography techniques were used to form the template. Once the template was fabricated, printing and self-assembly methods were used to fabricate many patterns because of inexpensive technology and high-throughput. Printing methods can be subdivided into additive, subtractive and diffusive printing. Additive printing employs an inked PDMS stamp and a bare substrate. Upon contact between the stamp and the substrate, the material transfers from the stamp to the substrate provided that the force of adhesion is stronger between the substrate and the material. First used to transfer self-assembled monolayers, the technique has now been extended to transfer biomolecules, colloidal particles, and polymers. In contrast to additive stamping, subtractive printing removes the material from the substrate as the stamp is peeled off. In this case, the compound is spin-coated on the substrate, and the stamp is brought into contact with the spin-coated surface. The compound adheres to the stamp more strongly than the substrate and is therefore peeled off. Lastly, diffusive stamping is similar to subtractive stamping in that the material is removed from the substrate. However, instead of simply adhering to the stamp, the material diffuses into the bulk of the PDMS stamp. All three forms of stamping have limitations requiring specific interactions between the material to be transferred and the substrate or the stamp.

Self-assembly relies on having molecules assemble in a pre-defined way to build a larger structure. When used in two dimensions, a surface can be functionalized with thiols or other compounds to impart spatially selective properties. The resulting differences in surface energies then direct molecules in a second step to spontaneously assemble in a spatially directed manner.

3.4. Stamp Fabrication

Both printing and self-assembly methods require a stamp that provides the template for patterning. Conventional photolithography techniques are employed to fabricate a template for the stamp. Polydimethylsiloxane (PDMS) is chosen as the material for the stamp because of its commercial availability and its widespread applications. The process of stamp fabrication is divided into three parts: designing the photomask, photolithography and PDMS molding as illustrated in Figure 3.3.

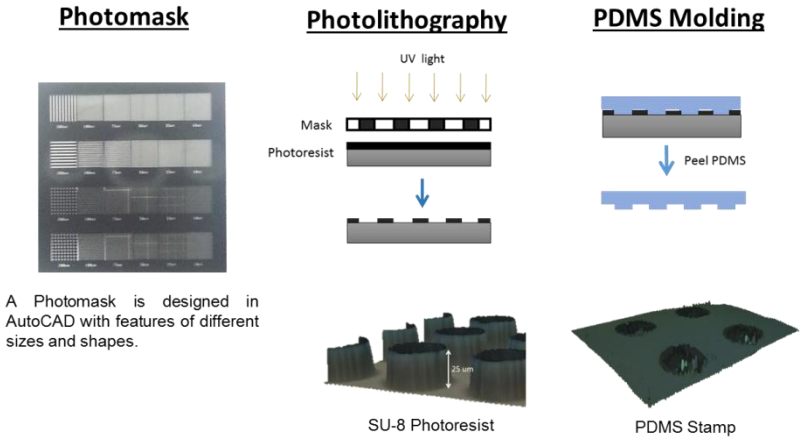

Figure 3.3. Fabrication of the PDMS stamp consists of three steps: designing the photomask, photolithography, and PDMS molding.

3.4.1. Designing the Photomask

The photomask was designed in freely available CAD software called DraftSight. The resulting .dwg file was sent to CAD/Art Services, Inc. The pattern was printed on a transparency

sheet using a high-resolution printer (Orbotech LP9008) that can print features down to 10 µm. For higher resolution mask, a chrome mask and the laser writer in Vanderbilt Institute of Nanoscale Science and Engineering were employed (Laser Writer Heidelberg Instruments µPG101).

Figure 3.4 depicts a couple of different photomasks designs. The first design consisted of increasingly spaced lines with separations ranging from 30 µm to 200 µm. The line widths were 25 µm in the left region, 50 µm in the middle region and 100 µm in the right region of the mask. The second design consisted of circles with separations ranging in dimensions from 30 µm to 200 µm.

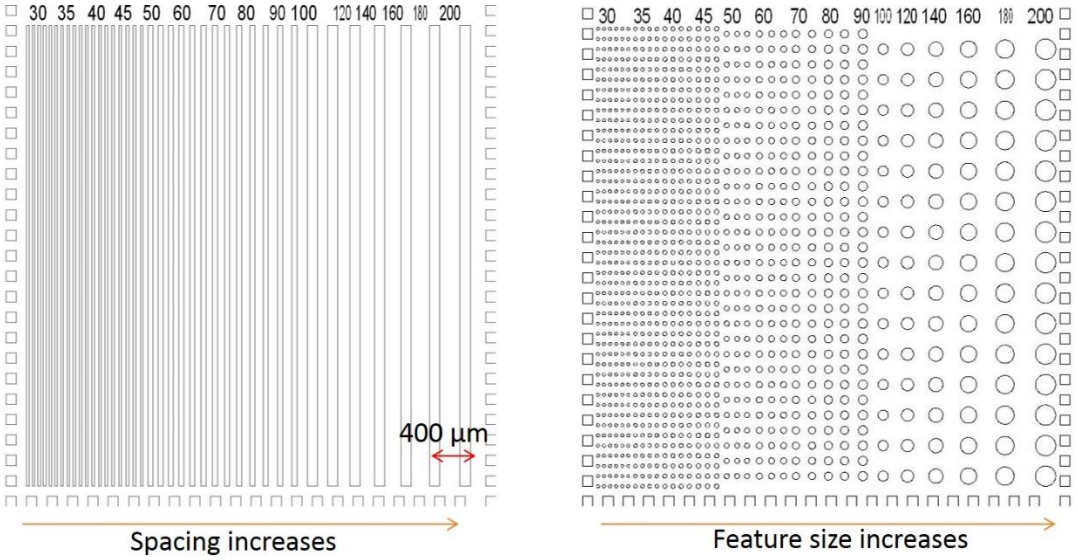

Figure 3.4. Photomask developed in a CAD software. (a) Line-gaps ranging from 30 to 200 µm (b) Circles with separations ranging from 30 to 200 µm.

3.4.2. Photolithography

The photomask was printed as a 2D pattern onto a transparent substrate. Conventional photolithographic methods were used to create a corresponding 3D relief pattern from the

photomask. Equipment outside of a cleanroom was utilized to save costs. A detailed list of equipment and the employed methods are included below.

Selection of the photoresist

Various polymeric materials have been developed for use as resists for microlithography.[38] In general, resists function by a change in their solubility due to a radiation-induced chemical reaction. Such reactions can either increase the solubility of the polymer (positive tone) or decrease its solubility (negative tone) in the irradiated regions.

A wide variety of positive and negative tone resists have been developed by companies such as Dow Chemical, Microchem, Shipley, and Micro Resist Technology. SU-8, an epoxy-based negative photoresist, was selected due to its ability to generate high aspect ratio features and stable vertical sidewalls. Depending on the desired aspect ratio and the lateral dimension of the relief structure, a specific member of the SU-8 3000 series can be chosen. Based on literature review, an aspect ratio between 0.3 and 1.0 for patterned structures is useful for contact printing applications.[39] For example, aspect ratios below 0.3 can result in the recessed regions of the stamp coming into contact with the substrate causing poor patterning for feature sizes below <100 nm. Aspect ratio above 1.0 may cause the vertical walls to bend causing blurry printing. Biswal et al. found that PDMS stamp with features ranging from 10 – 250 μm in lateral dimensions with 1.9 μm in thickness accurately transferred pattern by contact printing.[40] This suggests for features ≥ 10 μm aspect ratios between 0.2 – 0.008 are acceptable.

Since feature sizes in the range of 25 μm to 100 μm are needed for this application, 25 μm thickness of the photoresist is recommended as that will lead to aspect ratios in the range of 0.25 to 1. Equipment and process are described in more detail below.

Equipment

1. Spin Coater (MODEL-WS-650MZ-23NPP)
2. UV source (Dymax Light Curing System, Model 5000 flood) Intensity: 225 mW/cm^2
3. Two hot plates
4. Stopwatch
5. Tweezers
6. Pressurized nitrogen and a vacuum source

Process

1. Substrate Cleaning

Clean glass slide or silicon wafer by rinsing with acetone, isopropanol, and water. For best results substrates should be cleaned with a piranha etch (using H_2SO_4 & H_2O_2) followed by a de-ionized water rinse. Substrates may also be cleaned using reactive-ion etching.

2. Spin Coat SU-8 3025 (Results in ~25 μm thick photoresist coating)
    a. Dispense 1 ml of resist for each (25 mm) of substrate diameter
    b. Spin at 500 rpm for 5-10 sec with acceleration of 100 rpm/sec
    c. Spin at 3000 rpm for 30 sec with acceleration of 300 rpm/sec
3. Soft Bake for 8 min at 95 °C

To optimize baking times, remove the wafer from the hot-plate after the prescribed time and allow it to cool to room temperature. Then return the wafer to the hotplate. If the film ‘wrinkles’, leave the wafer on the hotplate for a few more minutes. Repeat the cool-down and heat-up cycle until ‘wrinkles” are no longer seen in the film after placing the wafer on the hotplate

4. UV Exposure: 25 sec with an absorptive neutral density filter 0.4
    a. Eliminate UV radiation below 350 nm using a long pass filter to obtain vertical sidewalls
    b. 170 mJ/cm^2 of net radiation in needed for 25 μm SU-8 layer on a silicon wafer. Detailed procedure for optimizing exposure time is outlined below.
5. Post Exposure Bake for 3 minutes at 95 °C

    1 min at 65 °C is recommended before post exposure bake for stress reduction

6. Develop for 5 min in SU-8 developer

    Strong agitation is recommended for high aspect ratio and/or thick film structures

7. Rinse and Dry:
    a. Spray/ wash the developed image with fresh developer solution for 10 sec.
    b. Then spray/wash with IPA for another 10 sec
    c. Air dry with filtered, pressurized air or nitrogen

Optimization of Exposure Time

One of the key parameters in the photo-lithography process is exposure time. The power rating on the UV source is 225 mW/cm^2. The SU-8 recipe suggests 170 mJ/cm^2 for silicon wafer and 255 mJ/cm^2 for the glass substrate. Based on these numbers, exposure times of 0.75 sec and 1.13 sec were calculated for silicon and glass substrates, respectively. For a glass substrate, exposure time of 1-2 second did not yield a pattern as most of the features were rinsed off in the developer solution. As the exposure time increased to 3 sec, features were observed although they were significantly enlarged. Figure 3.5 shows that the enlargement of 50 μm square as the

exposure time increased from 3 to 10 seconds. Even at 3 seconds, the size of the feature was 80 µm. At 5 sec, the height and width increased to over 90 µm. At 10 second exposure time, the square measured 116 x 111 µm. This increase was likely due to non-collimated beam undercutting the 50 µm feature on the photomask.

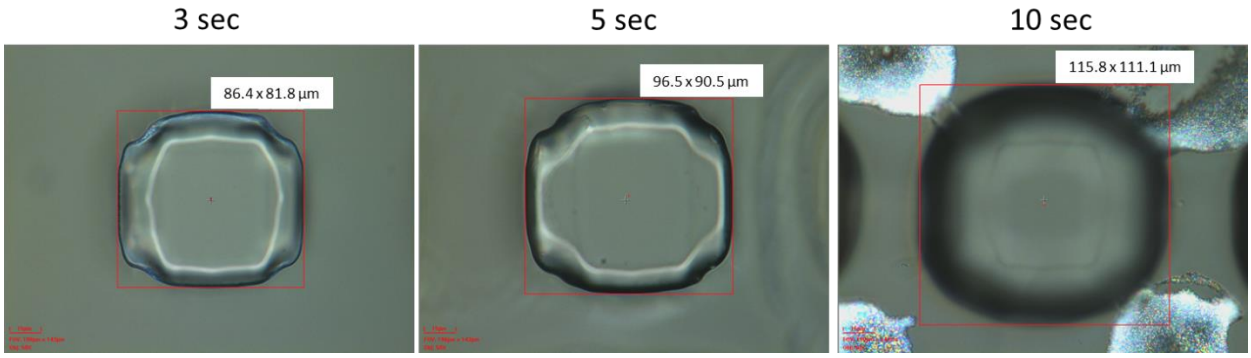

Figure 3.5. A 50 µm square feature on the photomask was transferred onto the SU-8 feature. The feature size increases significantly as the exposure time increases. The size of the feature after 3 s, 5 s, and 10 s exposure time are shown above.

Features ranging from 1-100 µm were exposed to UV radiation to experimentally determine the optimal exposure time. The photomask is shown in Figure 3.6a. Figure 3.6b shows SU-8 features on the glass substrate after the 3 sec exposure. Features above 50 µm coalesced together indicating overexposure whereas features below 20 µm were fully rinsed off suggesting poor adhesion. If the exposure time was too short, the SU-8 pillars were dissolved away in the developer solution. If the exposure time was too long, not all photoresist was removed from the masked regions. Figure 3.7 shows the height of the pillars as measured by optical profilometry. The distance between base and top of the pillars was measured to be 28 µm.

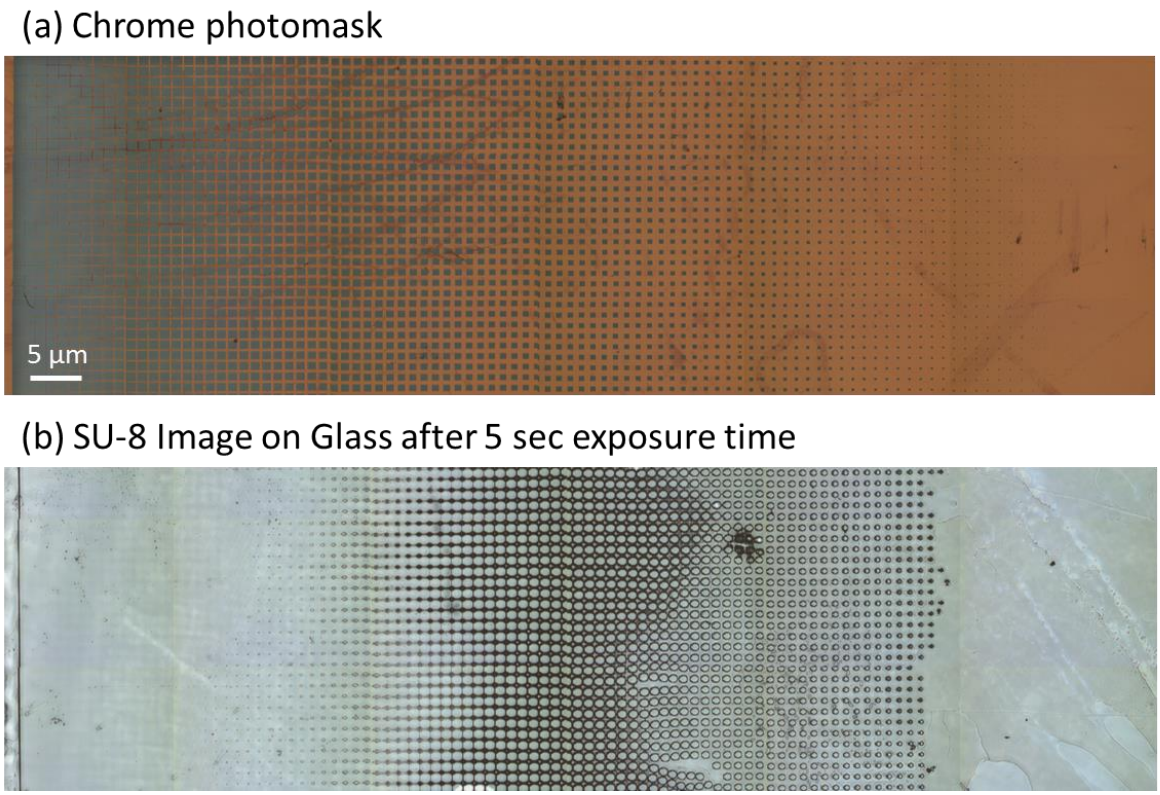

Figure 3.6. (a) Chrome mask showing features from 100 to 1 µm. (b) SU-8 master on glass indicates that features below 30 µm did not adhere to glass. All features have grown significantly in size from those on the mask.

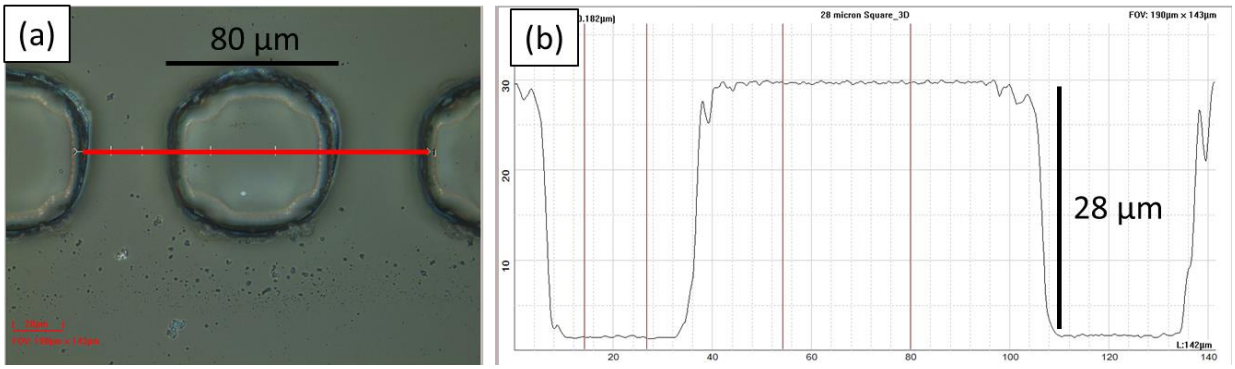

Figure 3.7. (a) A top-down view of the SU-8 feature that measures 80 µm in width (50 µm on the photomask). (b) The cross section of the pillar along the red line. The height of the pillar is 28 µm.

The exposure time of 0.75 s was deemed too short for silicon wafer especially since the exposure time on the UV-light curing system can only be controlled in increments of 1 s. An

absorptive neutral density filter 0.4 (50 mm square) was used to remove part of the ultraviolet-light and thereby increase the exposure time. Figure 3.8 shows that the filter blocked all of the radiation below 340 nm. The transmission gradually rose from 0 to 15%, as the wavelength increased from 340 nm to 390 nm. Above 400 nm, the transmission fluctuated around 40%. Based on the specifications of the UV Curing System, the range of emitted wavelengths is between 320 and 390 nm. Thus, the majority of the light was absorbed, and only about 5% of the light was transmitted on average in the 340 – 390 nm region. I examined a range of exposure times between 10 and 30 s and found that an exposure time of 25 s worked best. Figure 3.9 shows an SU-8 master with 30, 50, and 60 µm features produced on silicon using a 25 s exposure.

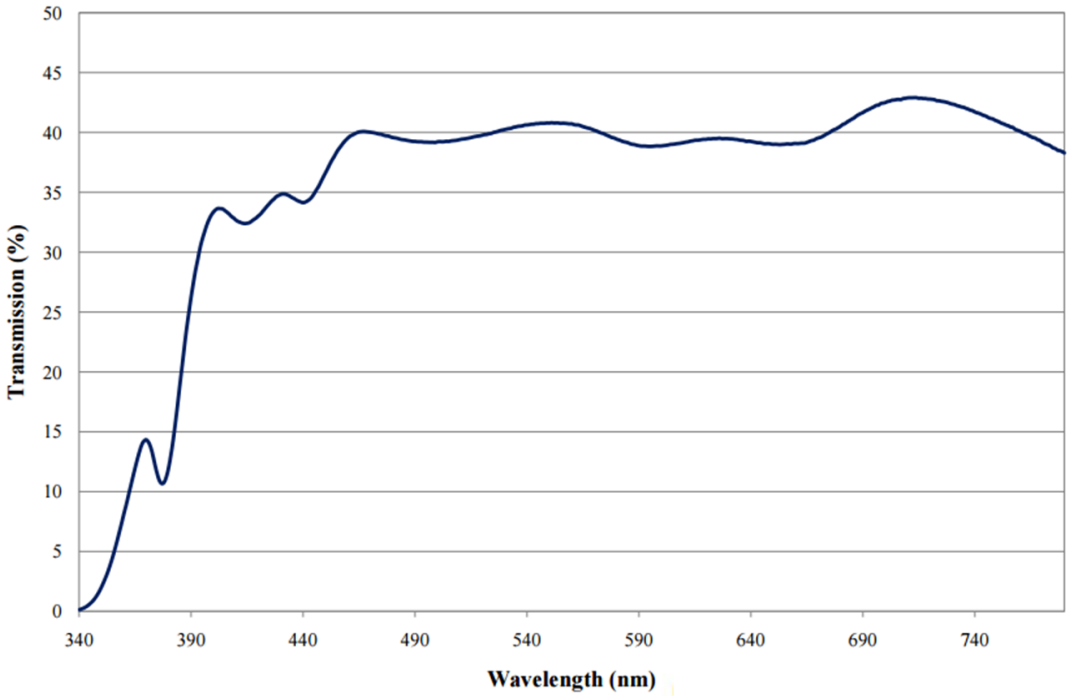

Figure 3.8. Transmission spectrum for a 0.4 optical density absorptive neutral density filter.

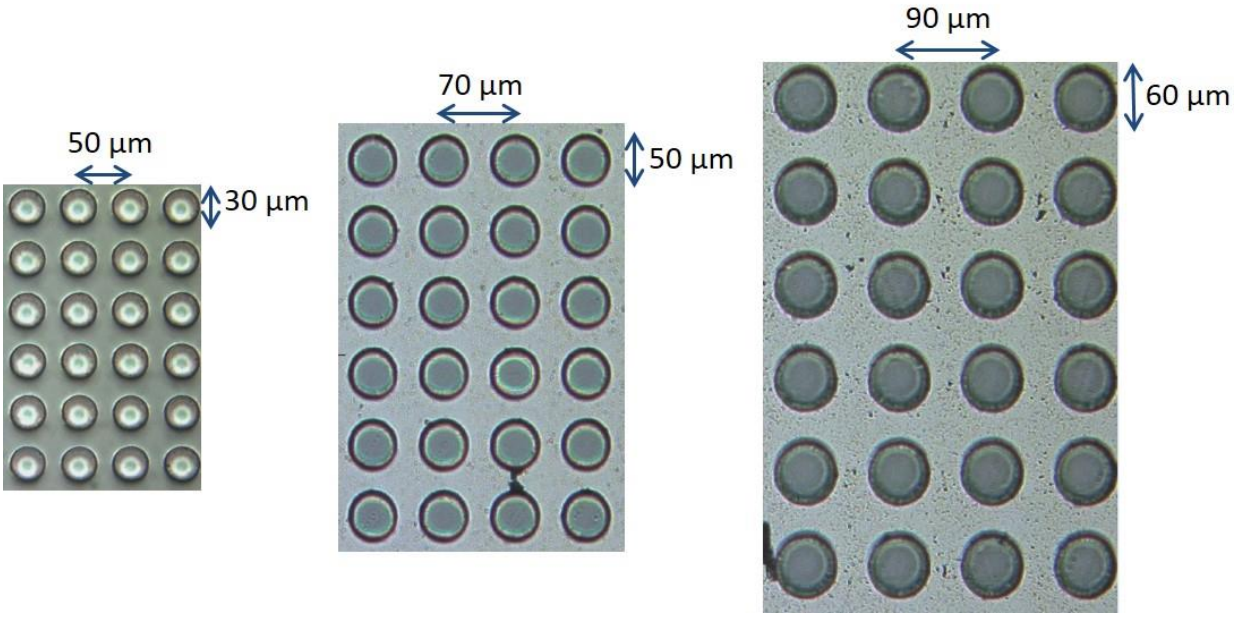

Figure 3.9. SU-8 master consisting of an array of circles ranging in size from 30 to 60 µm in diameter. The features were fabricated on a silicon wafer using SU-8 3025 photoresist and UV-photolithography.

3.4.3. Soft-lithography

Creating the photolithographic master can be expensive, particularly in the cleanroom environment. For features down to 25 µm in size, photolithography could be performed with few resulting patterning imperfections in a laboratory fume hood rather than in a cleanroom. The cost of this process can be further amortized by producing several replicas from the original master. Polydimethylsiloxane (PDMS) was chosen as the polymer used for creating replicas of the SU-8 patterns because of its beneficial rheological properties. Because of its viscoelastic properties, PDMS behaves as a viscous liquid at long flow times. As it is poured over the SU-8 master, it faithfully adapts to the surface of the master. Among the various types of commercial PDMS, Sylgard 184 from Dow Corning has been used most commonly for fabrication of stamps with feature sizes larger than 500 nm.[41]

The protocol used for fabricating the PDMS stamp was as follows:

1. The SU-8 master was cleaned with isopropyl alcohol and then dried with compressed air
2. The Sylgard monomer and the cross-linker were mixed in a 10:1 ratio by weight in a disposable plastic container. About 25 g of the mixture is recommended to fill a 3.5" Petri dish to a thickness of 5 mm. The viscous mixture was thoroughly mixed using a metal spatula for 3-5 min to ensure homogeneous distribution of the monomer and the crosslinker.
3. The plastic container was placed in a desiccator for 30 min to remove the trapped bubbles from the PDMS solution. After the bubbles had been removed, the pre-polymer solution was poured on top of the master.
4. The Petri dish with the master and the pre-polymer solution was placed in the oven at 80 °C for 2 h. The polymerization reaction takes 24 h to complete at room temperature.
5. The stiffness of the resulting stamp is directly related to the temperature of reaction and the ratio of the crosslinking agent. At higher temperatures and/or higher ratios of the crosslinking agent, a stiffer stamp is produced.

Figure 3.10 shows a 50 μm pillar on the SU-8 master and the corresponding 50 μm well on the PDMS stamp.

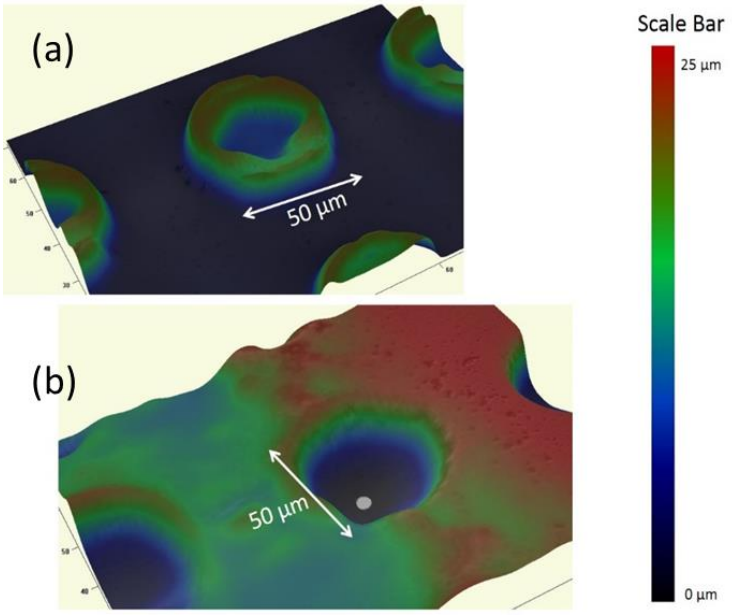

Figure 3.10. Optical profilometry of an SU-8 master and a resulting PDMS stamp. (a) Photoresist master with a 50 µm pillar. (b) A resulting PDMS well produced using soft-lithography from the SU-8 master.

The PDMS molding process could be repeated using the stamp as a master to create a negative replica of the stamp shown above. To minimize adhesion between the PDMS master and newly formed PDMS, the PDMS master was silanized with heptadecafluoro-1,1,2,2-tetrahydrodecyl-1-trichlorosilane for 1 h under vacuum. The silanization to generate a low energy surface on the PDMS master prevents PDMS-PDMS molding. The pre-polymer solution was poured onto the stamp and incubated in an oven as described earlier in this section.

3.5. Patterning using Printing

3.5.1. Detachment Lithography

After fabrication of the stamp, various options were available for generating patterned surfaces. Detachment lithography or subtractive stamping provides a method for patterning organic molecules on a surface.[42,43] This process is based on the relative adhesion strengths of

the organic dye to be patterned with the PDMS mold and with the substrate. In general, a pattern will be produced if the dye adheres to the PDMS stamp more strongly than it does to the substrate. The feasibility of this process can be determined by the work of adhesion, $W_{1,2}$, between two materials as described by

$$W_{1,2} = \gamma_1 + \gamma_2 - \gamma_{12} \tag{3.1}$$

where γ_1 and γ_2 represent the surface energies of materials 1 and 2, and γ_{12} is the interfacial energy between the two materials. For the case of patterning rubrene on an ITO substrate using a PDMS stamp, if $W_{rubrene,PDMS} > W_{rubrene,ITO}$, then the subtractive stamping should proceed to remove rubrene from the ITO substrate in regions contacted by the PDMS stamp.

Figure 3.11a shows a schematic representation of the subtractive stamping process. In brief, ITO-coated glass was spin-coated with the dye of interest. The PDMS stamp was brought into contact with the spin-coated surface for 30 s to 1 min. The stamp was gently peeled off to leave behind a pattern of the dye on the ITO substrate. Figure 3.11b shows that a pattern of rubrene could be successfully obtained by this method. The circles in the image are 50 μm in size and form a pattern of separated rubrene features on ITO.

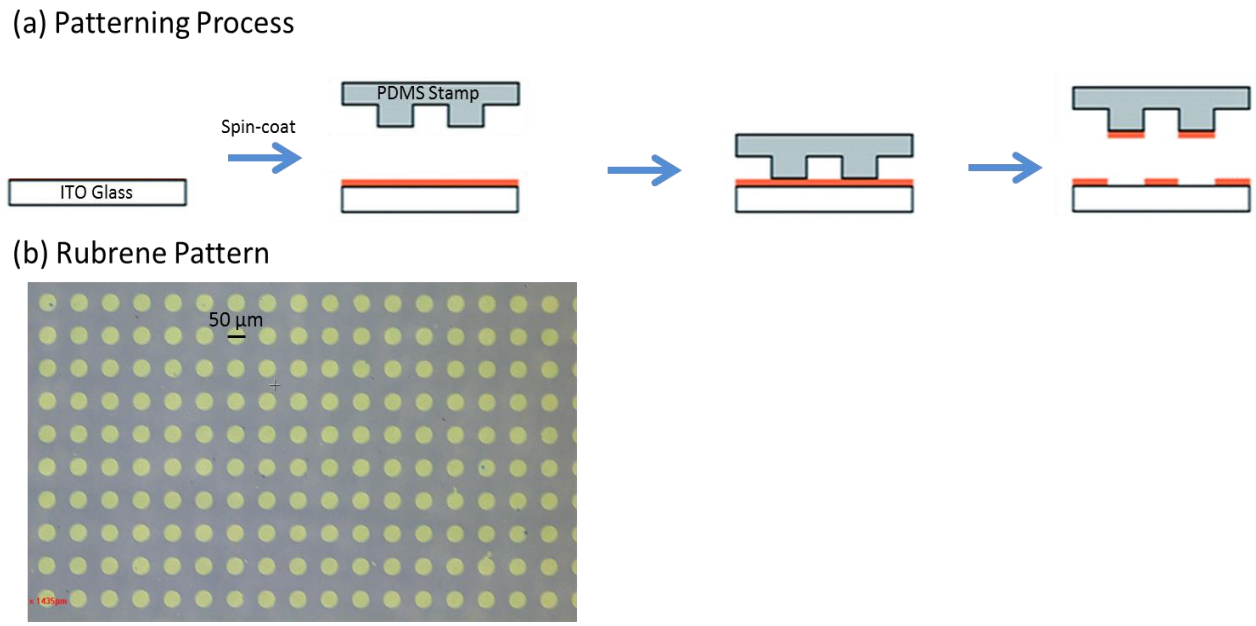

Figure 3.11. (a) Process for subtractive stamping. A PDMS stamp is brought into contact with a spin-coated surface. As the stamp is peeled off, contacted dye is removed. (b) Pattern of rubrene circles produced using subtractive stamping.

3.5.2. Diffusive Stamping

A second approach using a PDMS for patterning is shown in Figure 3.12a that is based on a diffusive printing process as described by Packard et al[44]. In this method, a dye is spin-coated on a substrate such as glass. The stamp is brought into contact with the spin-coated surface for a period to allow the dye to diffuse into contacting areas of the stamp. When the stamp is later removed from the surface, a pattern is left on the glass as shown in Figure 3.12.

The time needed for patterning by this diffusive printing approach is generally longer than that required for adhesive stamping. It depends on the chemical diffusivity of the dye into the PDMS which can be a slow process. Figure 3.12b shows some representative data for the amount of dye removed as a function of time.[44] For these literature data, the rate of removal was fastest for 3-(4-biphenylyl)-4-phenyl-5-*tert*-butyl phenyl-1,2,4-triazole (TAZ) and slowest for 2,2′,2″-(1,3,5-benzinetriyl)-tris(1-phenyl-1-H-benzimidazole) (TPBi). After 60 min, about 250

nm of TAZ was removed from a film by contact with PDMS as compared to less than 25 nm of TPBi that was removed over the same period. The contact time required for the diffusive stamping process depends both on the dye to be patterned and the thickess of its coating.

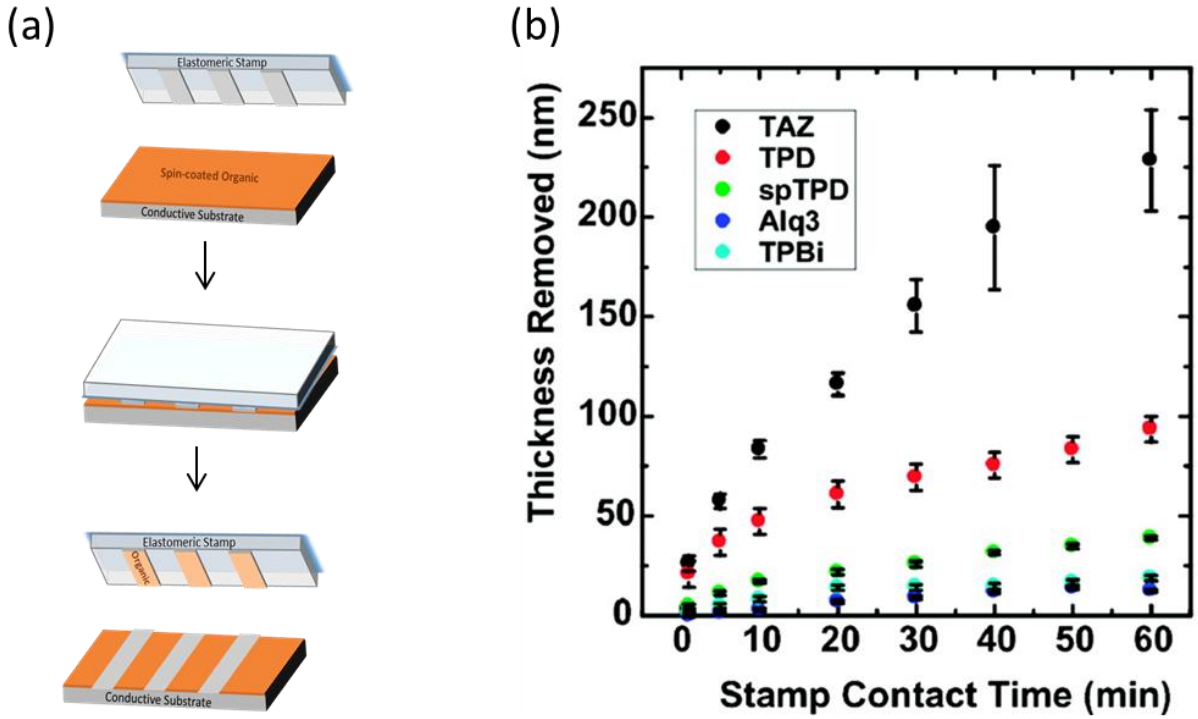

Figure 3.12. (a) Process for diffusive stamping. (b) Prolonged contact with a PDMS stamp results in a greater thickness of material removed for each of the five organic materials studied here. Figure reproduced with permission of Langmuir.[44]

The process of diffusive stamping was employed to pattern Oil Red O (ORO). For this process, it was critical to ensure long contact times between the stamp and the substrate to remove ORO completely from the contacted regions. Figure 3.13 shows that 30 min was an insufficient length of time to remove ORO from the surface as poor contrast was observed between the ORO and blank regions. If the stamp was left in contact with the surface for 1 h, ORO could be fully removed from the contacted regions. The length of time required to fully

remove the ORO was directly related to the thickness of the film, where films measured to be 40 nm by contact profilometry required 1 h for their complete removal.

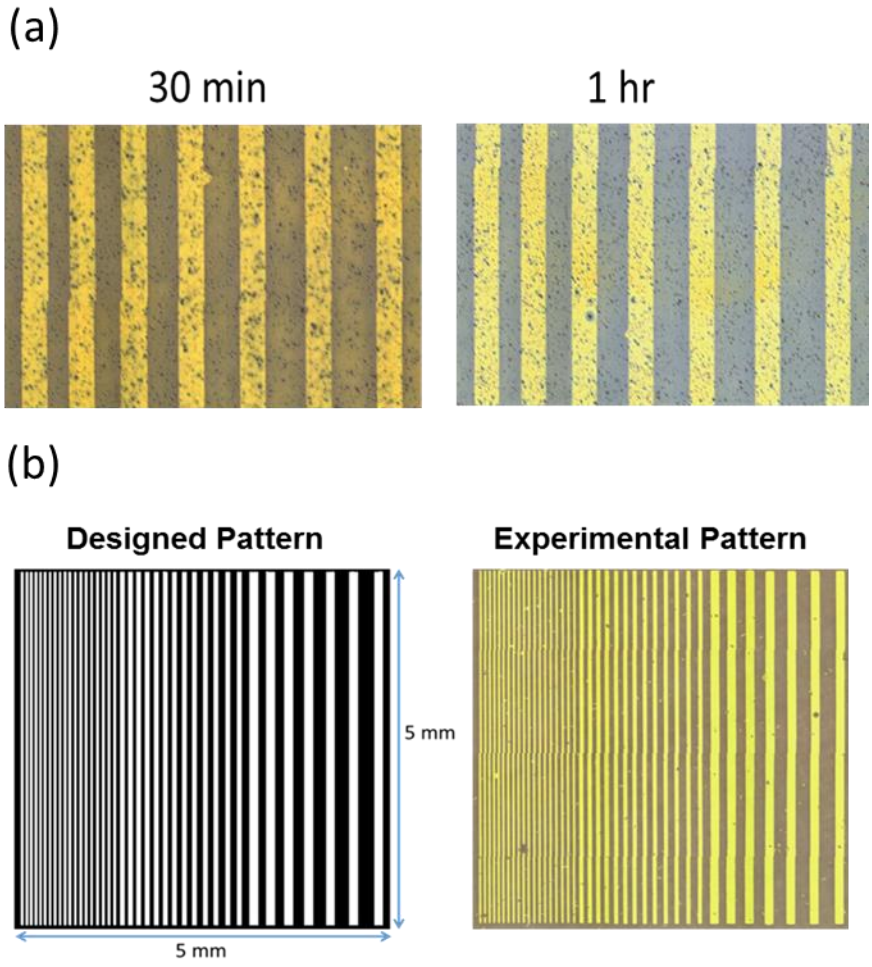

Figure 3.13. (a) Optical image of the ORO patterns obtained after a PDMS stamp was peeled from the surface. A contact time of 30 min with the PDMS stamp was insufficient to remove ORO from the contacted regions; however, a contact time of 1 h completely removed ORO from the contacted regions. (b) A comparison of the photomask designed in CAD software along with the ORO pattern that was produced using diffusive lithography.

3.6. Patterning using Surface Directed Self-assembly

An alternative approach for fabricating pattern organic films relied on a surface-directed self-assembly process for depositing organic molecules onto a functionalized substrate.[41] The

first step in the process was the patterning of a surface with a hydrophobic thiol. The adsorbed hydrophobic thiols then directed the deposition of the organic compound to be patterned in a second step into discrete areas. The method for surface functionalization is described below:

Surface functionalization

1. A standard gold-coated glass slide was cut into three square-shaped slides each measuring 1" x 1."
2. A PDMS stamp was inked with the solution of hexadecanethiol (~2 mM) using a Q-tip. The Q-tip was dipped into the solution of hexadecanethiol (HDT). The excess solvent was removed by grazing the tip against the rim. The entire surface of PDMS was gently coated with HDT.
3. 10 mL of H_2O_2 and 5 mL of KOH were poured into a glass Petri dish. Cut gold slides were immersed in this solution for 90 s to remove organic impurities from the gold surface. After 90 s, the slides were withdrawn from the solution, rinsed with water and ethanol, and dried in a stream of clean pressurized air.
4. After cleaning the gold slide, the stamp was brought into contact with the gold slide for 30 s to functionalize the gold surface. The edge of the stamp was first put in contact with the gold surface, and then the stamp was gradually tilted to bring it into full contact. This method minimized the possibility of trapping air bubbles.

3.6.1. Solvent Casting

After patterning a gold surface with a hydrophobic thiol by the PDMS stamp, the functionalized gold surface was used to direct the self-assembly of compounds in a spatially controlled manner. A saturated solution of the compound to be patterned was deposited on top of

the functionalized surface. As the solvent evaporated, crystals of the compound selectively deposited onto the bare gold regions and avoided deposition on the hydrophobic areas. As a result of this selectivity, a patterned coating of the compound was produced. The process of patterning α-cyano-4-hydroxycinnamic acid (CHCA) using this method is described below:

1. CHCA was dissolved at 10 mg/mL in Carnoy solution. Carnoy solution consists of 6:3:1 ethanol: chloroform: acetic acid
2. Water was added to this solution in a 1:1 ratio. The addition causes the solution to phase separate into organic and aqueous phases.
3. The aqueous phase was collected using a pipette and deposited onto the functionalized surface. As the solvent evaporated, the matrix crystallized and deposited in the hydrophilic regions. The solvent evaporation took about 30 min.

The directed self-assembly process is depicted in Figure 3.14. In the middle panel, the green areas represent gold regions that were stamped with the hydrophobic thiol, leaving the unstamped yellow areas more hydrophilic. A resulting pattern of CHCA produced by this process is shown in Figure 3.15.

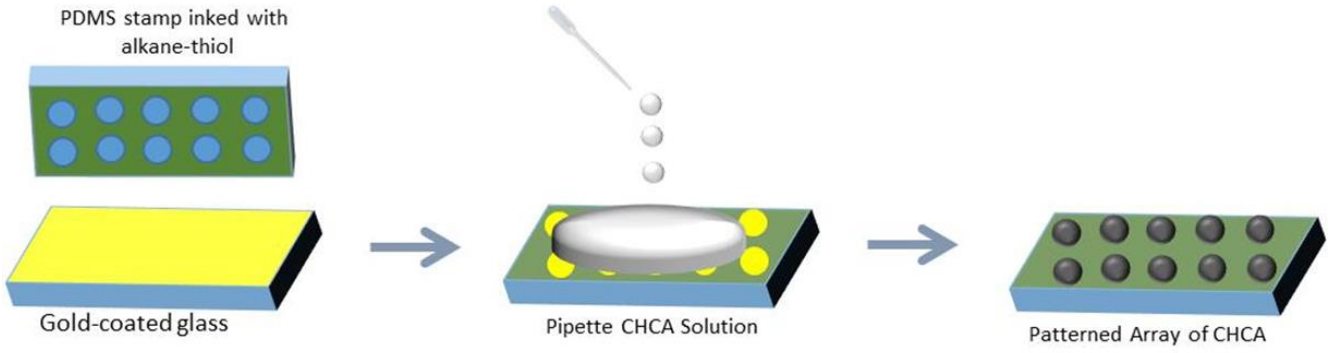

Figure 3.14. Directed self-assembly method for patterning CHCA. PDMS stamp inked with HDT was brought into contact with the cleaned gold surface. CHCA solution was deposited onto

the functionalized gold surface where CHCA molecules selectively deposited into the patterned hydrophilic regions.

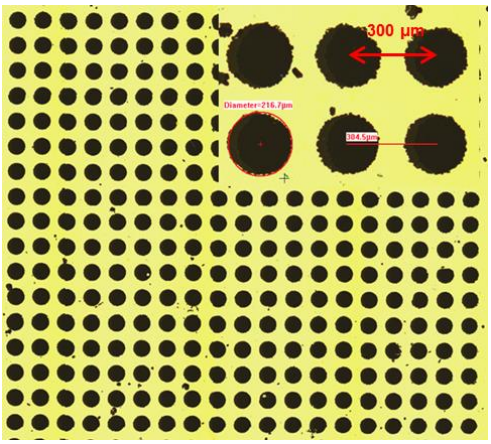

Figure 3.15. A patterned array of CHCA produced using self-assembly. Each circle of CHCA is about 200 µm in diameter, and the center-to-center distance is 300 µm.

Sinapinic acid was also patterned using this selective deposition process. The density of crystals could be easily controlled by varying the time of deposition. The sinapinic acid solution was pipetted onto the functionalized gold surface, and the solution was left on the slide for a specified period ranging from 1 to 11 min. As shown in Figure 3.16, the density of sinapinic acid increased as the time of deposition increased.

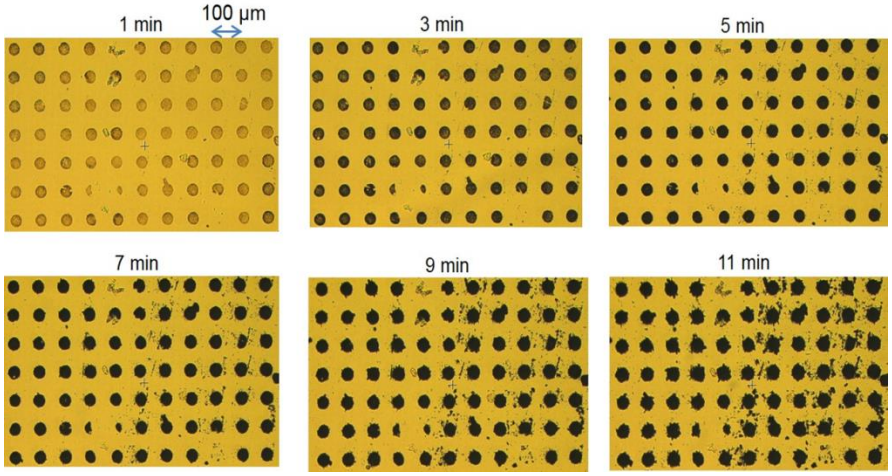

Figure 3.16. A microarray of sinapinic acid. The density of sinapinic acid crystal increased with the time of deposition.

3.6.2. Spin Coating

Selective deposition requires specific interactions between the substrate, the solvent and the solute. The process works well for relatively non-polar compounds such as sinapinic acid and CHCA. However, this method does not function for polar compounds. For example, crystal violet deposited in bulk on a functionalized gold and was not affected by the thiol pattern. Further testing involved forming a liquid layer of dye solution on the substrate and then quickly tilting the slide to remove the bulk liquid. Only small amounts of liquid would remain on the surface, and these remnants were confined to regions of bare gold. This technique was simple but had low reproducibility and could not form complete patterns on a substrate. Deposition was much more successful when carried out in a spin coater. The centrifugal force generated by the spin coater removed the bulk dye solution. The general spin coating procedure was as follows: the sample was spun at 600 rpm for 10 seconds during which the crystal violet solution can be deposited vertically. Typically, 300 μL of the solution was deposited. Most of the deposited solution was immediately removed from the substrate surface leaving behind a thin liquid film. Next, the sample was accelerated to 2000 RPM, and this rate of rotation was maintained for 2 minutes. The high rotation rate reduced the thickness of the liquid film to a level that pulled away from hydrophobic regions to form a pattern.

Water, acetonitrile, acetone, ethanol, and various combinations of these solvents were attempted. Water was found to be too polar; droplets of CV in water quickly dewetted the functionalized gold surface leaving no pattern behind. It is hypothesized that the lower the surface tension of the solvent, the slower it de-wets and greater the likelihood of leaving behind dye in designed patterns. Ethanol provided the appropriate solvent for the formation of a pattern. The solution was sonicated for 10 minutes and filtered with 0.45 μm mesh. A concentration

range between 2 – 20 mg/mL was attempted; 2 mg/mL generated a very thin pattern of CV whereas 20 mg/mL resulted in random blotches on the pattern. Solution with concentration of 10 mg/mL provided a good compromise between the amount of material deposited and 'cleanliness' of the pattern.

3.7. Characterization of the Reticle

The reticle was characterized using optical microscopy, contact profilometry and atomic force microscopy. Figure 3.17a shows a representative optical image for a reticle prepared in a traditional wet chemical laboratory environment. The image shows a series of parallel lines of crystal violet (dark regions) separated by changing distances between them. The crystal violet lines ranged in thickness from 300 to 800 nm, as measured using contact profilometry and atomic force microscopy. In general, the narrower lines were thinner than the wider lines. In comparing the reticle pattern with that of our photomask, the measured widths of the crystal violet lines and the gaps between them were both ~2% smaller than those in the mask. This difference was attributed to shrinkage of the PDMS stamp as no size differences were found between the features in the photomask pattern and those in the SU-8 master. Figure 3.17b shows a magnified view for one of the 100 μm wide crystal violet lines from the reticle. In this image, both sides of the crystal violet line show an edge sharpness of better than 1 μm which was routinely achieved across all lines by the fabrication method.

MS signals from the crystal violet pattern were readily obtained by direct laser ablation without the use of the matrix. Figure 3.17c displays a representative mass spectrum from the reticle, showing a monoisotopic peak at m/z 372.5 that corresponds to crystal violet (M) after the loss of chlorine ion, $[M - Cl]^+$. The ease of generating of the peak at m/z 372.5 and measuring its

intensity provided the basis for mapping variations in its locational intensity from the reticle and using these variations for determining spatial resolution.

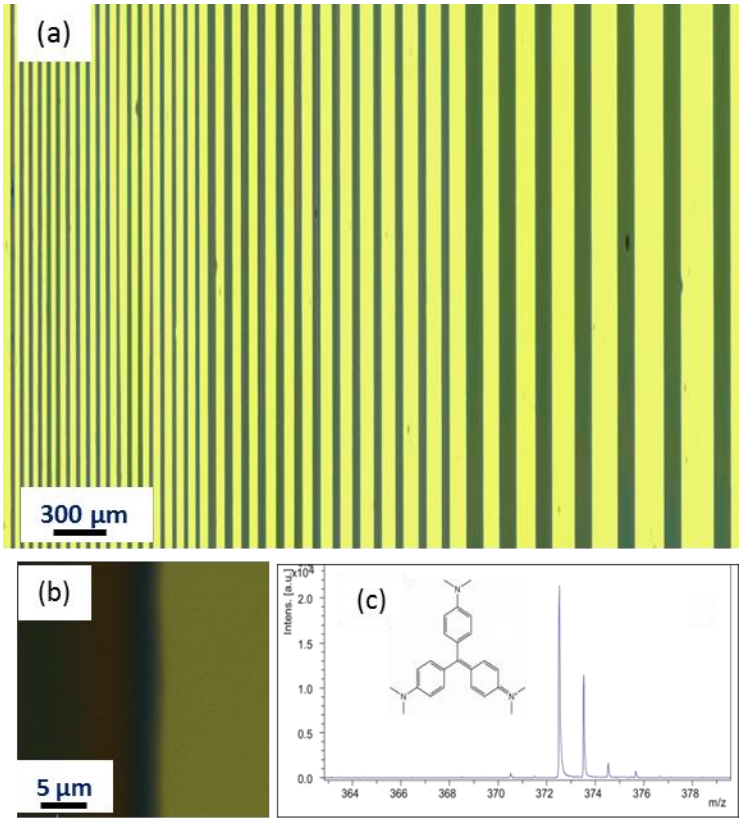

Figure 3.17. (a) Optical microscopy image of the reticle. The widths of the crystal violet lines are 25 µm, 50 µm, and 100 µm from left to right. The gaps between the crystal violet lines range from 30 µm to 200 µm. (b) Magnified view of a 100 µm crystal violet line. (c) Mass spectrum obtained from the reticle showing a monoisotopic peak at m/z 372.5 Da that represents crystal violet after the loss of its chlorine ion. Direct laser ablation was sufficient to detect this peak for crystal violet without the use of a matrix.

The reticle was also characterized using contact profilometry and atomic force microscopy (AFM). Figure 3.18 shows the results acquired using Stylus contact profilometer in VINSE. A diamond tip was translated across the reticle and differences in height were measured. The results indicate that the height of the features was generally between 300 – 600 nm except for some unusually thick lines towards the left that were between 1000-1600 nm. Additionally,

the wider lines towards the right show 'M' shaped profile; this profile is attributed to faster rates of evaporation along the edges.[45] Figure 3.19 shows AFM image at the edge of 100 µm crystal violet line. The AFM image shows that several large crystals with heights up to 280 nm.

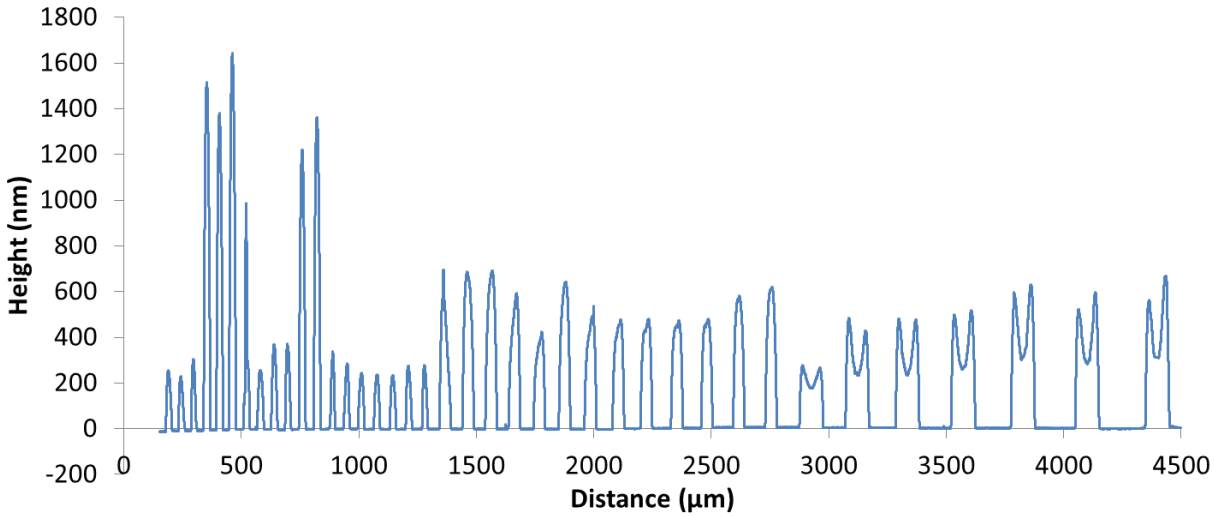

Figure 3.18. A contact profilometery scan across the crystal violet pattern measuring the height of the features.

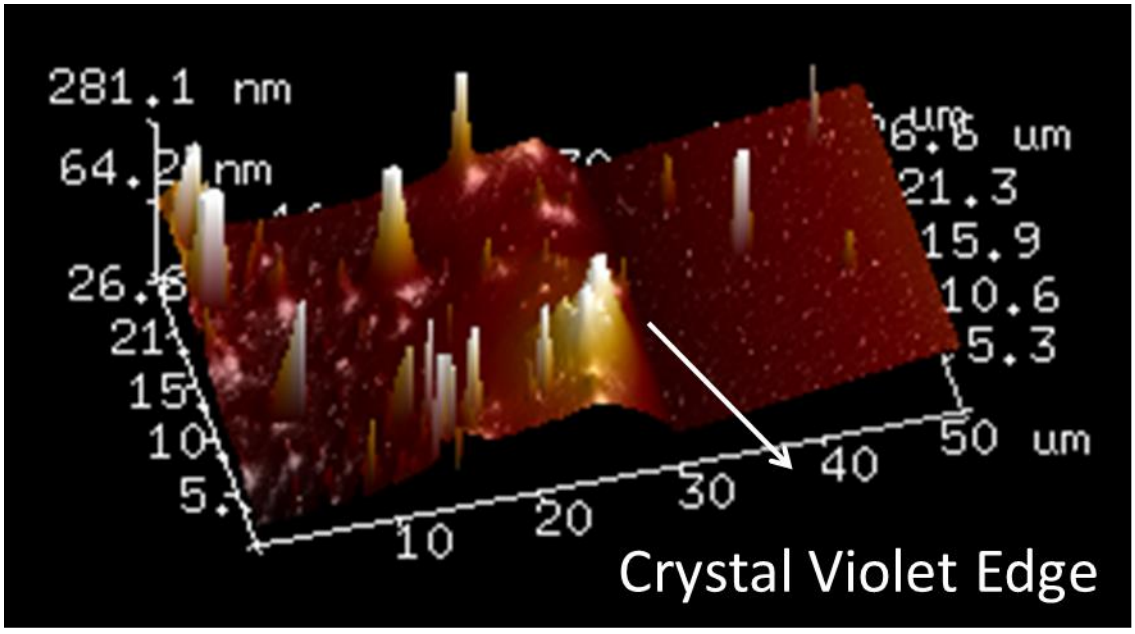

Figure 3.19. An AFM image acquired at the edge of a crystal violet line. Several peaks up to 280 nm in height are observed in the crystal violet region.

CHAPTER 4. A STANDARD RETICLE SLIDE TO OBJECTIVELY EVALUATE SPATIAL RESOLUTION AND INSTRUMENT PERFORMANCE IN IMAGING MASS SPECTROMETRY

4.1. Overview

Matrix-assisted laser desorption/ionization (MALDI) imaging mass spectrometry (IMS) is an enabling tool for medical and biological research. Since the first publication in 1997,[1] the technology has been applied to study the distribution of wide variety of analyte classes including metabolites, lipids, peptides, and proteins in biological samples.[2-4] In a typical MALDI IMS experiment, a frozen or fixed tissue is sectioned and thaw-mounted onto a target. The resulting tissue section is coated with a MALDI matrix usually by sublimation or spray-based methods. The matrix-coated tissue sample is then analyzed by a serial raster of the laser across the tissue section, acquiring a mass spectrum at each defined x, y coordinate. Following the acquisition, the spectral ion intensity is plotted for ions of interest providing two-dimensional maps of specific molecular distributions.

Instrumental conditions in IMS experiments offer tradeoffs in various aspects of performance. For example, higher spatial resolution IMS generates a greater number of pixels in a given area compared to the same area sampled at a lower spatial resolution. Consequently, higher spatial resolution images allow the visualization of fine structural detail; however, the file size for such images will be greater and their acquisition time will be longer. Depending on the experimental task or question to be answered, instrument parameters are typically selected to achieve particular image characteristics. Beam optics, laser energy, the number of laser shots,

and stage step size can be independently tuned for each experiment. For example, to achieve high spatial resolution, Gaussian laser beams have successfully been focused to small diameters, whereas smartbeam™ (Bruker Daltonics) lasers have been developed to yield high sensitivity.[46] Spatial resolution is also limited by sample stage positioning, with most commercial instruments offering 1-10 μm stage accuracy. As vendors and investigators actively refine instrumentation, objective methods are needed to test for and correct hardware inaccuracies (e.g., inaccuracies in data acquisition and stage positioning) that can diminish spatial resolution. Monitoring the consequences of instrumental parameters and catching potential errors affecting spatial resolution is crucial to maintaining high-quality IMS data.

Several investigators have reported methods for evaluating spatial resolution in secondary ion mass spectrometry (SIMS). Senoner et al.[47] fabricated a multilayer structure comprising alternating layers of GaAs, AlGaAs, and InGaAs using metal organic chemical vapor deposition. They used this target in cross-section to evaluate spatial resolution in SIMS across 16 laboratories in 10 countries.[48] They scanned the beam across a narrow strip (0.5-50 nm) of $Al_{0.65}Ga_{0.35}As$ and used the intensity profile to estimate the beam width. They also imaged a series of parallel lines to estimate spatial resolution using the Rayleigh criterion.[34] Passarelli and Ewing fabricated a reticle with gratings of liposomes and PEG that they used to measure spatial resolution in TOF-SIMS and MALDI-TOF, obtaining FWHM values of ~2-4 μm and ~184 μm, respectively.[35] The high value of FWHM observed in the case of MALDI-TOF was because of subsequent steps required for sample preparation, including the use of a solvent-based matrix spray that caused delocalization of the liposomes and PEG. This confounding factor prevented the intrinsic measurement of MALDI instrument spatial resolution. Fagerer et al.[49] placed a tungsten grid on top of matrix coatings to evaluate spatial resolution in a MALDI-TOF

instrument with continuous stage motion. While the use of a grid as a physical mask with defined openings provided a simple approach, the laser beam was distorted upon transmission through the grid.

In the present work, we developed a method to measure the spatial resolution of a given instrumental setup of an imaging mass spectrometer. Our approach employs a device that consists of a crystal violet pattern on a conductive substrate; crystal violet was selected because it readily desorbs and ionizes upon laser ablation. Imaging this crystal violet pattern enables a direct measurement of beam size and spatial resolution without the delocalizing effect of matrix application or the distorting effect of a masking grid as encountered for other methods. The developed reticle provides a reliable standard for measuring and comparing spatial resolution across different MALDI imaging platforms. With the reticle, the measurements of spatial resolution could be automated. We also present results using this approach to evaluate the effects of the laser energy and focus setting on spatial resolution. The reticle described here includes patterned features with dimensions ranging from 30 to 200 µm. The lithographic techniques used in the fabrication of the reticle can be scaled down to smaller dimensions when needed for evaluating spatial resolutions below 30 µm.[50]

4.2. Methods

Mass Spectrometry Instrumentation. The reticle was used to assess the performance of three mass spectrometers: a Bruker UltrafleXtreme MALDI-TOF/TOF (Billerica, MA), a Bruker Rapiflex MALDI Tissuetyper (Billerica, MA), and a SimulTOF 300 Tandem MALDI-TOF/TOF (SimulTOF Systems, Sudbury, MA). The Bruker Ultraflextreme was equipped with a smartbeam^{TM} and operated in positive ion reflector mode at 20 kV. A laser step size of 5 µm was used in both the x- and y-directions. The laser focus setting was set to different settings including

'ultra', 'medium', and 'small'. Laser power was individually adjusted for each focus setting to enable comparable ion current for crystal violet. Each pixel represents signal accumulated from 100 laser shots.

The Rapiflex was also equipped with smartbeam^{TM} laser and operated in positive ion reflector mode at 20 kV. A laser step size of 5 µm was used in the x-direction; a step size of 30 to 70 µm was utilized in the y-direction as stated in the text. The laser focus setting was set to 'single', 'mod 5', and 'mod 5 defocus'. The laser power was individually adjusted for each focus setting. Each pixel represents signal accumulated from 50 laser shots.

The SimulTOF 300 Tandem was operated in positive ion reflector mode at 8 kV. This system is equipped with a 349 nm, diode-pumped, frequency-tripled Nd:YLF laser (Spectra-Physics, Santa Clara, CA) capable of laser repetition rates up to 5 kHz. The laser energy was controlled by adjusting the current applied to the diode and was maintained at 14.5 µJ/pulse for all experiments (as measured prior to attenuation, which was kept constant). The instrument utilizes continuous laser raster sampling. All images were acquired under instrument conditions set for 50 µm spatial resolution (50 µm spatial resolution in the x-direction as defined by the laser repetition rate, stage speed, and number of hardware averages, and 50 µm spatial resolution in the y-direction as defined by the motor step size between continuously rastered rows). We systematically altered laser repetition rate, stage speed, and number of hardware averages as noted in the text to maintain a lateral spatial resolution of 50 µm.

Data Analysis. Image data for edge spread and point-spread methods were acquired on the UltrafleXtreme using Bruker FlexImaging 3.0 and were imported into MATLAB using a

conversion tool created within this lab. Subsequent numerical analysis was conducted in MATLAB; the relevant code is provided in Supporting Information (see SI-1). The curve fitting toolbox was used to model experimental results, and 18-20 rows of data were averaged together to determine beam sizes. Data for determining spatial resolution using line gratings were acquired on the Rapiflex using Bruker FlexImaging 5.0. The data were converted into Analyze 7.5 format, and further analysis was conducted in MATLAB (see Supporting Information, SI-2). For line-scan determination of spatial resolution, 10 rows were averaged together. Image data from the reticle acquired on the SimulTOF instrument were analyzed using the SimulTOF Viewer.

4.3. Results and Discussion

4.3.1. Laser Alignment and Accuracy

The circular feature of CHCA can be used to test the laser alignment. A laser pulse is directed at the center of 200 µm CHCA crystal in the instrument software. After 1000 laser shots a 60 µm crater is created. As shown in Figure 4.1 below, the ablation crater is at an offset of 25 µm from the center of the CHCA circle indicating that the laser was not aligned accurately with the stage. An array of features with various sizes can be used to verify the laser accuracy. Laser accuracy is particularly important for histology-directed analysis where the molecular profiles are needed from localized regions on the tissue.

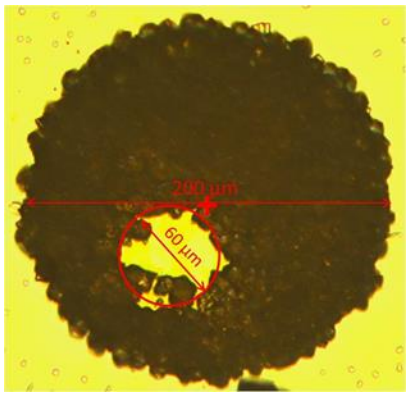

Figure 4.1. Evaluation of laser alignment using a patterned array of CHCA. The laser was targeted at the center of the spot. The ablation crater was at an offset of 25 µm from the center of the spot suggesting misalignment of the laser.

4.3.2. Qualitative Evaluation of Spatial Resolution

The synthetic pattern produced by lithography techniques was used to evaluate the spatial resolution of the MALDI source of the Bruker Ultraflextreme TOF instrument. In the designed pattern shown in Figure 4.2, the white material represents organic compounds and the black represents empty regions. The linewidth increases from 30 µm to 200 µm. The pattern was imaged with a 25 µm raster step size. From the "zoomed in" ion images at the bottom of the figure, it can be concluded that this imaging setup can adequately resolve lines of 80 µm, but is not able to resolve line widths of 40 µm.

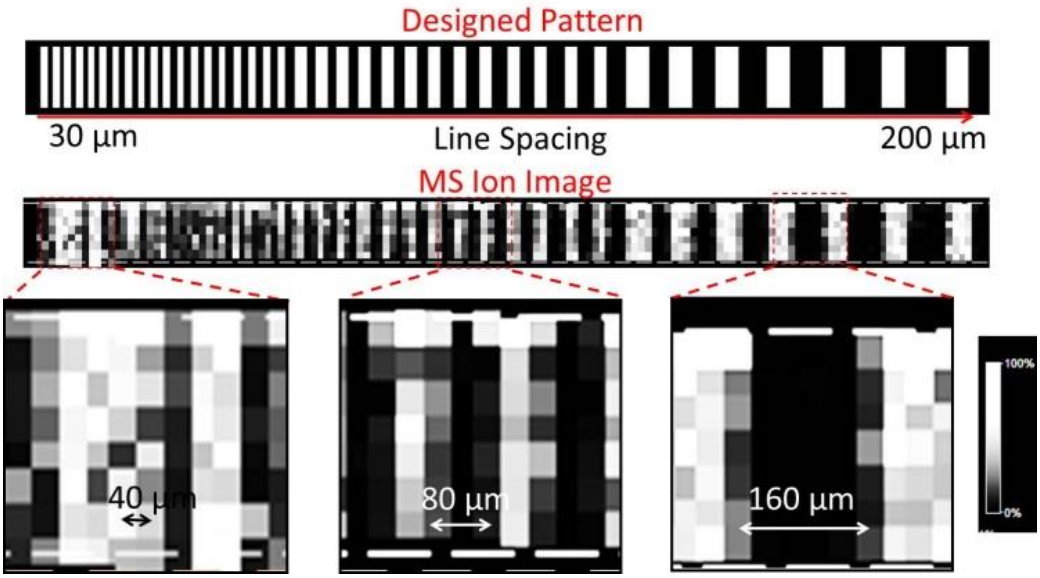

Figure 4.2. Qualitative evaluation of spatial resolution using an oil red O pattern with separations ranging from 30 to 200 µm. Above 80 µm separation, the lines are clearly resolved; however, 40 µm separation is not resolved.

4.3.3. Measurement of Gaussian Beam Size by Imaging a Sharp Edge

A routine method for measuring the beam size of an irradiated spot on a target within an IMS instrument would be useful for characterizing instrument performance and assessing the effects of alterations made during instrument development on instrument resolution. The 'knife edge' method is a common approach for characterizing beam size, where the beam intensity is measured as a sharp edge is translated perpendicular to its path.[51-52] An analogous approach can be used where the beam is translated across a sharp edge of a patterned feature, and the obtained line profile is evaluated. The steepness of the edge profile can then be used to characterize the sharpness of the image.[51] This measurement of signal intensity across the sharp edge of a pattern is attractive because it is simple, it characterizes the beam size at the site of interest, and it can yield similar profiles even for very different beam shapes.

With a suitable target, the edge spread profile approach can be adapted for MALDI IMS and provides a measurement of the beam size responsible for generating detectable signals. This measured 'effective' beam size would be the region of the laser beam with intensity above the threshold needed for ablating material and generating ionized molecular species for detection. The actual size of the laser beam on the target would be larger than that obtained by this approach; however, as this measurement only reflects the region of the incident beam that generates MS signal, it would provide more suitable information for assessing spatial resolution for MALDI-IMS.

We employed this edge spread profile approach to characterize the spot sizes provided by a Bruker Ultraflextreme mass spectrometer under three different focus settings: ultra, medium, and small. At each setting, the power was set just above the ionization threshold to prevent excessive ablation of crystal violet from the reticle during the scan. In the experiment, the laser beam was scanned toward the edge of a crystal violet feature on the reticle in 5 μm steps as illustrated in Figure 4.3a. The crystal violet pattern consisted of parallel lines, each having edge resolutions of better than 1 μm as estimated from microscopy images at high magnification (Figure 3.17b). Figure 4.3b-d shows the signal intensity for crystal violet at these three focus settings as the position of the crystal violet edge was translated across the incident laser. Typically, multiple adjacent non-overlapping scan lines were combined for analysis. In Figure 4.3b-d, all three scans exhibited a transition from no to full signal as the edge moved across the beam. At each setting, we separated the scans of signal intensity with stage position into three regions: a background signal from the bare substrate, a rising signal across the edge, and a maximum signal from the crystal violet area. We fit horizontal lines to the background and maximum signals and applied a polynomial fit to the rising signal between these values. To

compare these profiles, we determined values of $\Delta_{12\text{-}88\%}$, the lateral distance over which the signal intensity changed from 12 to 88% of the signal difference across the edge, as this distance corresponds to the full-width half maximum (FWHM) for a Gaussian profile. For FWHM values greater than 30 μm, the profiles exhibited well-defined shapes for this analysis. In contrast, smaller spot sizes (< 20 μm) were more sensitive to local differences in the amounts of crystal violet on the surface, leading to greater difficulties in fitting the region of maximum intensity by a horizontal line. Despite this challenge, we estimate the uncertainty in $\Delta_{12\text{-}88\%}$ to be a few micrometers.

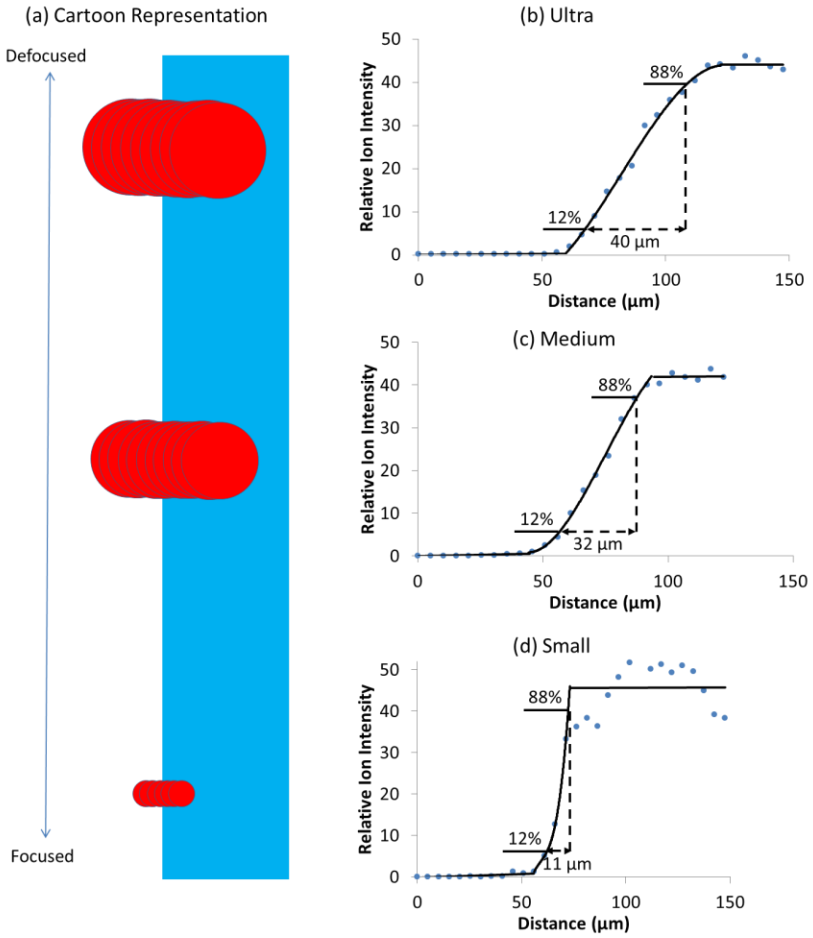

Figure 4.3. Edge spread profile analysis obtained by scanning a smartbeam laser across a crystal violet edge. (a) Schematic illustration of laser pulses traversing the crystal violet edge as the stage is moved in 5 µm steps. (b)-(d) Average ion intensity for crystal violet vs. distance (µm) at three different laser focus settings: 'ultra', 'medium', and 'small'. Effective beam sizes were measured to be 40 µm, 32 µm, and 11 µm, respectively. The signal intensities with respect to the distance are the average from ~20 adjacent scans.

Table 4-1 summarizes the averaged results from three independent edge spread profile measurements using the reticle at each of three focus settings. The data were obtained under acquisition conditions where the average signal intensities were at similar levels to minimize differences in ablation levels. The measured FWHM values showed good reproducibility at each setting and clearly distinguished the differences in lateral size for the different beam settings.

Table 4-1. Results from edge spread profile analysis of a smartbeam laser at various focus settings. The ± values represent standard deviations from three measurements.

Laser Focus Setting	Laser Power	Average Signal/Pixel (x 10^4)	$\Delta_{12-88\%}$ (μm)
Ultra	82.0%	9.6	45 ± 4
Medium	83.2%	7.5	31.9 ± 0.3
Small	84.8%	7.1	11.2 ± 0.8

4.3.4. Measurement of Gaussian Beam Size Using the Convolution of PSF with the Object Pattern

The edge spread profile method described above involves imaging a single sharp edge or a step function. Its precision is limited by the available step size for the scan, particularly for smaller beams. As shown above, variations in the signal intensity in a region where its value should be a maximum can introduce uncertainties for defining the position of the edge. To overcome this issue, we extended the edge spread profile method to the characterization of a pattern of step edges separated by known distances. The separation distances between the crystal violet features on the reticle and their widths were defined by the photomask used to generate the reticle and verified by optical microscopy. In cross-section, the pattern provides a series of rising and falling edges with known distances between them, thereby reducing the uncertainty in the position of any one edge profile in a scan. By this approach, the results across multiple edges can be evaluated simultaneously for measurement of the effective beam size on the target.

To describe the signal intensity expected from the beam moving in a direction perpendicular to the parallel lines of crystal violet on the reticle, we employed a general two-

dimensional point spread function (PSF) that would describe the beam profile (i.e., shape, size, and power distribution). The PSF can be considered as an impulse response of the incident laser beam on the target that is responsible for producing a blurred image of the actual pattern. The PSF profile for the incident beam may have a Gaussian, Top-hat, Lorentzian, or other shape depending on the optical setup. When used to image a pattern, the intensity of each pixel $i(x', y')$ in the resulting image represents a convolution between the pattern provided by the target being imaged and its blurring by the PSF. The mathematical representation for this convolution is presented in detail in chapter 2 along with the development of general mathematical expressions to describe the expected variations in signal intensity for imaging a pattern of parallel lines. For a Gaussian-shaped beam, the signal intensity obtained by scanning across four parallel lines in the perpendicular direction with widths and separation distances for the pattern shown in Figure 4a can described by the equation:

$$i(x', y') =$$
$$A_{min} + A_1\left[\mathrm{erf}\left(\frac{x-b}{\sqrt{2}\sigma}\right) - \mathrm{erf}\left(\frac{x-b-100}{\sqrt{2}\sigma}\right)\right] + A_2\left[\mathrm{erf}\left(\frac{x-b-260}{\sqrt{2}\sigma}\right) - \mathrm{erf}\left(\frac{x-b-360}{\sqrt{2}\sigma}\right)\right] +$$
$$A_3\left[\mathrm{erf}\left(\frac{x-b-540}{\sqrt{2}\sigma}\right) - \mathrm{erf}\left(\frac{x-b-640}{\sqrt{2}\sigma}\right)\right] + A_4\left[\mathrm{erf}\left(\frac{x-b-840}{\sqrt{2}\sigma}\right) - \mathrm{erf}\left(\frac{x-b-940}{\sqrt{2}\sigma}\right)\right] \qquad (4.1)$$

where x' and y' are the center positions of the incident beam, σ is a parameter describing the width of the beam in the x-direction, *b* represents the position along the x-axis of the first rising edge (i.e., the edge of the first line), A_{min} represents a background signal level, and A_1, A_2, A_3, and A_4 represent the maximum signal amplitudes obtained on each line. The different values for these maximum signal amplitudes accommodate for local intensity variations in the maxima from each feature should they occur.

Figure 4.4b shows experimental data of the signal intensity obtained from line scans performed on the test pattern shown in Figure 4.4a along with the best fit by eq 4.1. The experimental data were obtained with a step size of 5 μm, an acquisition setting of 100 shots/pixel, an 'ultra' focus setting, and a power setting of 82.0%. The signal intensity exhibits four rising and four falling transitions, with the maximum signal intensity obtained from each line showing some variations. The data are fit well by eq 4.1, yielding a 95% confidence range of 16.4 ± 0.8 μm for the characteristic beam width, σ, at this acquisition setting. The second set of experimental data obtained under the same operating conditions yielded a 95% confidence range for σ of 16.8 ± 1.0 μm, showing good reproducibility for the method.

Related experimental data sets of signal intensity as a function of laser focus position and power setting were obtained on the pattern of four lines to examine their effects on the characteristic beam width. Figure 4.4c shows that using a 'medium' focus setting and a power setting of 83.2% resulted in a smaller beamwidth, σ, of 13.1 ± 0.7 μm. As the 'medium' instrumental setting provided a more focused beam than the 'ultra' setting, the σ value was expected to be reduced as was observed. For this data set, the best fit exhibited flatter tops than those in Figure 4.4b, resulting from greater sharpness in the rising and falling transitions. Figure 4.4d shows the results for the 'small' focus setting at a power setting of 84.8%. Under these conditions, the fit to eq 4.1 produced a 95% confidence range for σ of 5.4 ± 0.9 μm. Flatter tops are even more apparent in the fit for the 'small' focus setting, consistent with the greater sharpness in the rising and falling transition regions. Table 2 summarizes the results of these and related experiments showing the reliability of the determined values of σ. As the focus is changed from 'ultra' to 'medium' to 'small', the FWHM of the beam decreased from 40 ± 2 μm to 30.8 ± 1.6 μm to 13 ± 2 μm.

Across these three different focus settings, a consistent 95% confidence range of ± 1.0 μm or less on the value of σ was obtained, corresponding to a FWHM range of ± 2.0 μm or less, when a sufficient laser power setting was used. In all cases, the model fit the transition regions well, with the greatest departures being in the regions of maximum signal intensity, possibly reflecting local variations in crystal violet amounts within the patterned lines. These differences likely affect little the measurement of σ as its primary influence on eq 4.1 is the sharpness of the fitting curve in the rising and falling transition regions. The known locations of and the distances between these transition regions in the pattern allow the determination of σ by a fully objective curve fitting algorithm, providing a notable advantage over the analysis method performed over a single step edge (Figure 4.3) where the exact position of the edge in a scan is not known. Further, the fitting approach using eq 4.1 is amenable to being conducted under automated control and being performed on other related patterned structures with different separation distances and line widths for determining σ with greater confidence by a global fitting strategy.

Table 4-2 summarizes the results of experiments testing the effects of various instrumental settings on the determined values of σ. As the focus setting was changed from ‘ultra’ to ‘medium’ to ‘small’, the measured FWHM values for the beam showed a reproducible change from 40 to 13 μm. The values obtained at each focus setting were consistent with each other, with small differences in laser intensity causing small variations in the uncertainty values. Laser power settings that yielded much weaker signal intensities produced fits having the greatest uncertainty in the fitted FWHM values; however, the 95% confidence intervals on the FWHM values measured at the lower laser power settings were consistent with those obtained at that focus setting and a higher laser power setting.

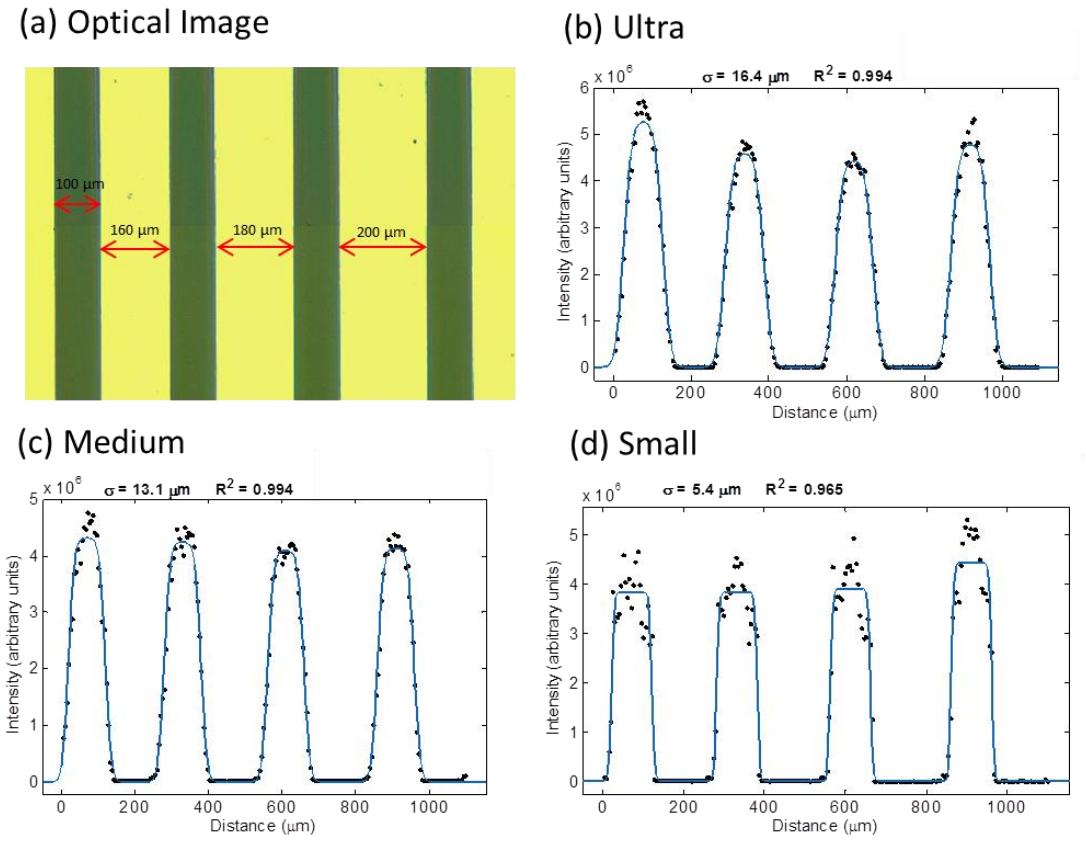

Figure 4.4. Edge-profile analysis across multiple rising and falling edge profiles of known spacings. (a) Crystal violet pattern before laser ablation. Each crystal violet line is 100 µm wide; the gaps between the lines are 160 µm, 180 µm, and 200 µm from left to right. Beam focus and power settings were adjusted manually for each of the three experiments. (b) Beam focus = 'ultra'; σ = 16.4 µm. (c) Beam focus = 'medium'; σ = 13.1 µm. (d) Beam focus = 'small'; σ = 5.4 µm. Data are fit are to eq 4.1 to provide measurements of σ.

Table 4-2. Beam width values obtained from edge spread analysis across multiple rising and falling edge profiles of known spacings under different focus and power settings.

Laser Focus Setting	Laser Power	Average Signal/Pixel (x 10^4)	σ (μm)	FWHM (μm)
Ultra	82.0%	9.0	16.8 ± 1.0	40 ± 2
	82.0%	9.6	16.4 ± 0.8	38.6 ± 1.9
Medium	83.2%	7.5	13.1 ± 0.7	30.8 ± 1.6
	82.4%	0.3	12.2 ± 2.7	29 ± 6
Small	84.8%	7.1	5.4 ± 0.9	13 ± 2
	84.8%	8.0	5.5 ± 0.8	13.0 ± 1.9

At each of the focus settings in the Table 4-2, the step size (5 μm) was smaller than the calculated FWHM values for the beam. As a result, adjacent laser spots overlapped with one another during a scan raising the concern whether oversampling could be occurring that could affect signal intensity. In preparing the reticle, the crystal violet features were fabricated to be sufficiently thick (> 300 nm) to ensure that they would not be completely ablated during a scan when typical laser power settings were used. An optical image of the crystal violet pattern after imaging is provided in Figure 4.5a showing that most of the crystal violet is retained. We tested to ensure that such changes to the crystal violet film did not dramatically affect signal intensity. Under the standard laser power settings, we found that the signals provided from previously investigated homogenous areas of crystal violet were roughly 90% or more of those obtained previously unexamined areas and the measured FWHM values were unchanged. At higher power settings, it was possible to ablate greater amounts of crystal violet (as shown in Figure 4.5b) and produce results compatible with oversampling. For example, in scanning a previously investigated region at a ‘large’ (i.e., intermediate between ‘‘medium’ and ‘ultra’) focus setting, a

FWHM value of 21.9 ± 1.4 μm was obtained that was roughly 10 μm smaller than was obtained for this setting in a first scan. The lower value of FWHM is consistent with an oversampling type of experiment in which the signal intensity would rise more quickly and reach a plateau faster across a pattern. By proper control of conditions, oversampling could be avoided. By such repeated scans, the reticle provided the ability to evaluate whether its measurements of the spatial resolution were compromised by oversampling effects.

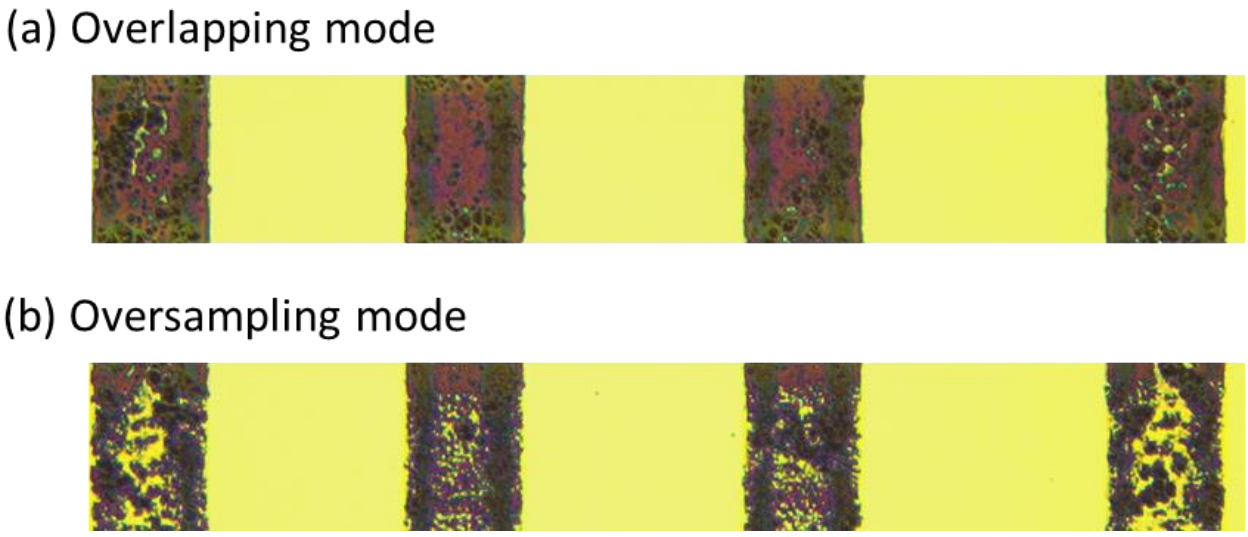

Figure 4.5. Optical images of 100 μm-wide crystal violet lines after MALDI imaging. (a) Effect of operating in an overlapping mode where a moderate laser power was used. (b) Effect of operating in an oversampling mode where a high laser power was used.

4.3.5. Use of Line Gratings to Determine Spatial Resolution

Spatial resolution is defined as the smallest spacing in an image that can be recognized as distinct and separate within a specified threshold. The effective beam sizes determined by the edge spread and PSF methods detailed above provide a measurement related to spatial resolution but are themselves not a direct measure of spatial resolution. The ability to resolve a small region with attributes different from those adjacent to it underlies most determinations of spatial resolution. Various criteria have been suggested for assessing spatial resolution such as those

reported by Rayleigh and Sparrow that have been primarily used for optical measurements. The Rayleigh criterion measures the separation between two equal point sources such that the central maximum in the signal originating from one source overlays with the minimum signal from the other. An empirical estimate of spatial resolution is made based on the observation of an intensity level from a region that has a value that is 19% lower in intensity from that of two nearby maxima, as expected for two equal point sources with this separation.[34] The Sparrow criterion defines the minimum possible spatial resolution by the observation of a dip in the obtained signal from separated equal point source.[34] A drawback of these methods is that neither of these criteria includes experimental uncertainties such as noise in their theoretical assignment of spatial resolution. The reliance of the Rayleigh and Sparrow criteria on the ability to discern modest differences in the signal from those that may be due to noise severely limits the application of these criteria for IMS. Instead, we employed a threshold level where the ability to distinguish separated sources of no signal intensity was used to provide a measurement of spatial resolution. Specifically, we defined a threshold level of 10%, so that if the signal intensity dipped to a value less than 10% of that of the maximum as the laser beam is scanned across a striped pattern, the features are said to be resolved.

For determination of spatial resolution in IMS, we designed a pattern that would provide a series of parallel stripes that differed in their separation distances between them. Figure 4.6a shows an illustration of the line grating design used to produce the photomask that yielded the reticle pattern. The numerical values in Figure 4.6a represent the separation distances (the black regions) in microns between adjacent stripes (the white regions) of the reticle pattern. The white regions in the photomask correspond to those areas on the reticle that contain crystal violet, and the black regions define their separation. Figure 4.6b shows an optical image of a crystal violet

pattern obtained using the photomask by the procedure summarized in Figure 1. The crystal violet areas appear black against the gold background for the uncovered areas. Figure 4.6c shows the ion image collected at m/z of 372.5 ± 0.2 Da corresponding to the positively charged hexamethyl pararosanilium ion from crystal violet. The image was acquired at a 10 μm step size, a 70% focus setting, and 84% power. The image data were converted to a graphical view shown in Figure 4.6d by averaging ion intensities from 10 sequential scans. The signal switches from high to low-intensity values across the pattern, with the minimum values increasing in intensity from regions with smaller separation distances between the crystal violet regions. The red line in Figure 4.6d shows the cut-off used for establishing spatial resolution from the pattern. The cut-off was set to 10% of the maximum intensity. If the ion intensity from a region with a particular separation distance fell below this cut-off value, the instrumental conditions are said to resolve that feature size. Relatedly, the instrumental conditions were unable to resolve a particular feature size if the ion intensity from a region with that separation distance did not fall below this cut-off value. The data in Figure 4.6d exhibit a progression of behaviors. In Figure 4.6d, the smallest separation distance resolved consistently was 45 μm, as the line-scan in this region (highlighted in green) consistently yielded signals below the 10% cut-off value. At a smaller separation distance of 40 μm between the striped regions, the yellow region notes a limiting resolution as the line-scan dips below the cut-off inconsistently (three out the four times). The red region (35 μm separation distances) highlights results obtained below the limit of resolution as the line-scan intensity was consistently above the 10% cut-off value across this striped region. We note that this general method would be applicable to irregularly shaped beams and not just limited to Gaussian, Lorentzian, or Top-hat beam profiles.

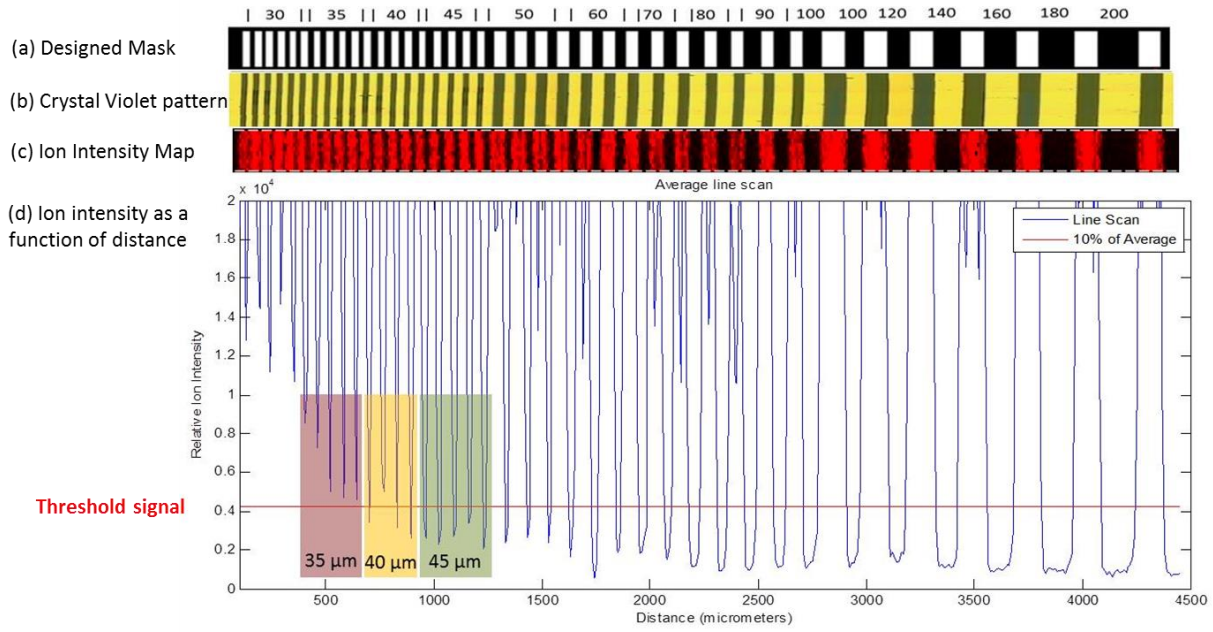

Figure 4.6. (a) Photomask pattern as designed in CAD software with specified dimensions in microns. The white rectangular regions represent transparent areas, and the surrounding black regions are opaque. (b) Resulting crystal violet pattern fabricated using the photomask, soft lithography, and surface patterning techniques. (c) Ion image acquired by MALDI IMS of the distribution of m/z 372.5 Da corresponding to signal from crystal violet after the loss of chlorine. (d) Line-scan of ion intensity for crystal violet across the pattern. The threshold signal (red line) is calculated as 10% of the obtained signal from regions with crystal violet.

We applied the method detailed in Figure 4.6 using the 10% threshold to measure the spatial resolutions across various operating conditions. Table 4-3 summarizes the results of experiments performed at three different laser focus setting: ‘single,' ‘mod 5,’ and ‘mod 5 defocused.' At each focus setting, three different power settings were tested. For each experiment, we also compared the spatial resolution measurements obtained from the line-scan analysis with the size of ablation craters produced in homogeneous coatings of crystal violet under the same instrumental conditions. For the ‘single’ laser focus setting, the intensity values dipped below the 10% threshold value between each stripe for all power settings, demonstrating a spatial resolution below 30 µm. For the ‘mod 5’ laser focus setting, the smallest resolved separation was 50 µm at a laser power setting of 39.4% and was 60 µm at laser power settings of

43.4% and 47.4%. For the 'mod 5 defocused' laser focus setting, the resolved separation spacing was below 30 μm for 62.8% power, while at laser power settings of 66% and 70%, the smallest resolved separation increased to 35 μm and 70 μm, respectively. Across all laser focus settings, the smallest resolved separation between features grew with increasing power suggesting a greater sampling area by the beam at higher power levels.

Table 4-3. Measurements of spatial resolution using line gratings across various instrument settings

Laser Focus Setting	Laser Power (%)	Smallest Resolved Separation (μm)
Single	19.0	<30
	21.0	<30
	23.0	<30
Mod 5	39.4	50
	43.4	60
	47.4	60
Mod 5 defocused	62.8	<30
	66.0	35
	70.0	70

For comparison with the obtained spatial resolution measurements, we exposed homogeneous coatings of crystal violet to repeated laser pulses at the above instrument conditions and measured the size of the resulting ablation craters. We note that the number of laser pulses required to generate visible ablation craters in the crystal violet coating was ~20

times that used to obtain the data in Figure 4.6c. Images of the resulting ablation craters are provided in Figure 4.7. For comparison, each image includes an overlay with dimensions of the smallest resolved separation obtained using the line grating at that instrumental condition from Table 4-3.

At the 'single' laser focus setting, individual ablation craters less than 30 μm in diameter were obtained at the three investigated power settings, consistent with the ability to consistently resolve separation spacings of 30 μm and greater below the 10% threshold level. At the 'mod 5' laser focus setting, the ablation patterns consisted of five separated craters, with one in the center and the other four positioned around it. Their relative positions appeared unaffected by laser power; however, the diameters of the five craters were larger at the higher power settings. At the lowest power setting of 39.4%, two of the peripheral craters appeared less developed than the other three craters suggesting that most of the ablation occurred from a more limited region, consistent with the ability to resolve a smaller separation than at the higher power settings. Ablation craters of similar size were produced at the higher laser power settings of 43.4% and 47.4% consistent with a common separation spacing of 60 μm being resolved at these two conditions. Using the 10% threshold level, the obtained separation spacing of 60 μm from the line-scan analysis was smaller than the distance between the furthest ablated regions (~80 μm); however, it compared favorably to the furthest distance between the regions—the center of each crater—where the greatest ablation occurred. At the 'mod 5 defocused' laser focus setting, ablation occurred non-homogenously over broad areas but appeared more concentrated at the lower power settings. For example, at the 62.8% power setting, ablation was observed from regions more than 60 μm apart; however, most of the ablation occurred from a smaller region less than 30 μm in diameter. At the higher power settings of 66% and 70%, the ablated regions

extended out more than 100 μm; however, most of the ablation occurred from more localized regions ~40 and ~80 μm in diameter, respectively, at these settings. In comparing these values with the spatial resolution measurements obtained using the 10% threshold level, the lower values representing the size of main ablated regions correlated favorably with those measured with the reticle. This agreement with measurements based on ion intensity suggests that while the laser pulse may ablate material from a broader area, a minimal signal is generated from the outer regions. The laser energy may be insufficient in the peripheral regions to ionize crystal violet or the signal from these areas may contribute little to the overall signal produced by a laser.

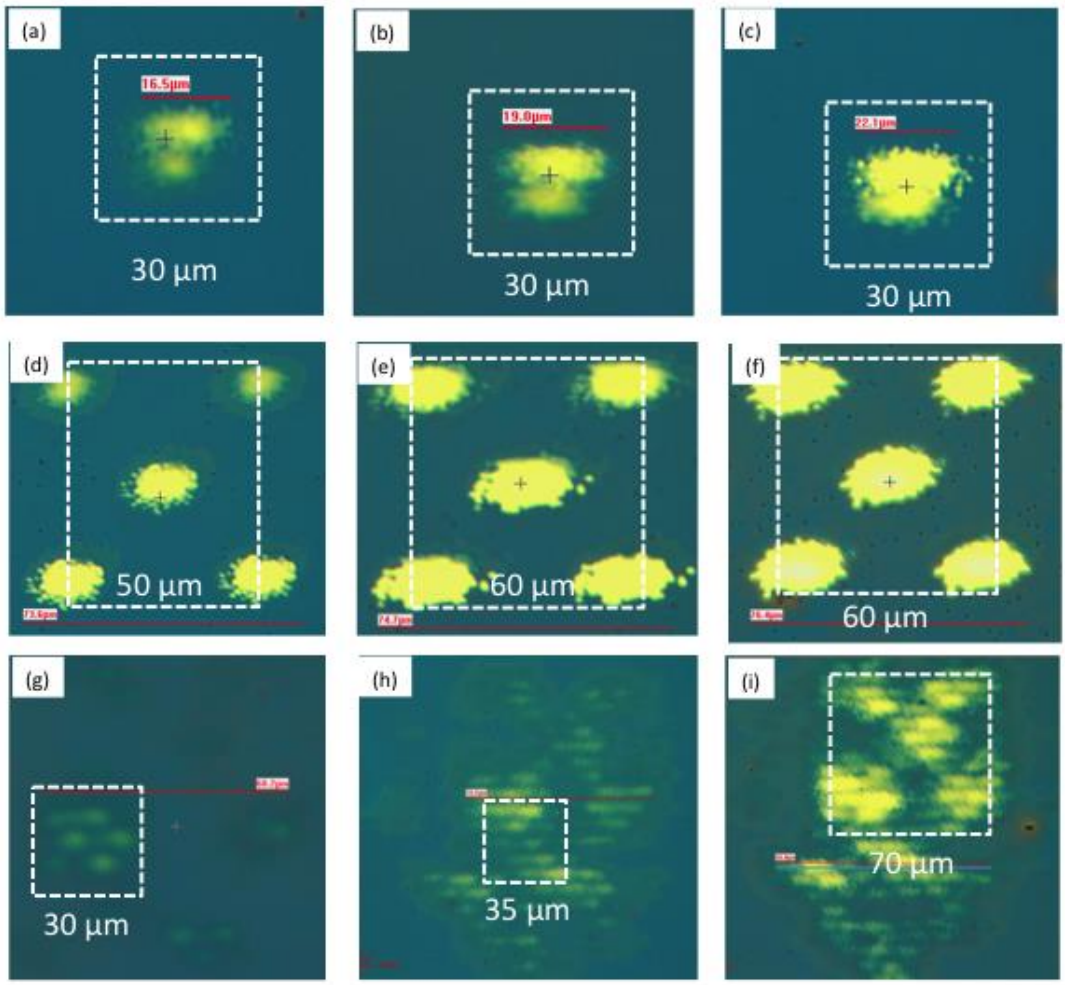

Figure 4.7. Optical images of the ablation craters formed in a homogeneous coating of crystal violet after 1000 shots under various focus and laser power settings using a Bruker Rapiflex. (a) 'Single' 19.0% power (b) 'Single' 21.0% power (c) 'Single' 23% power (d) 'Mod 5' 39.4% power (e) 'Mod 5' 43.4% power (f) 'Mod 5' 37.4% power (g) 'Mod 5 defocus' 62.8% power (h) 'Mod 5 defocus' 66.0% power (i) 'Mod 5 defocus' 70.0% power. 'Single' 'Mod 5' and 'Mod 5 defocus' designate specific focus settings on the Bruker Rapiflex used for ablation. The boxes included in each image are sized at the smallest resolved separation determined using the line-scan method with values given in Table 4-3.

The ablation craters shown in Figure 4.7 as generated by laser pulses at various operating conditions illustrate a common problem in relating the ablation crater to spatial resolution for IMS. In general, the non-uniform, complex shape of the laser beam and its lack of homogeneity challenge defining its suitable size. As such, any assignments of a "beam size" from such

ablation results include subjective assessments of how a single dimension can define their pattern. As the areas of ablation may not directly correspond to the areas that generate a signal, such determinations of their size provide a gross estimate for image resolution that may lack meaning. In contrast, the approach presented in Figure 4.6 provides an objective result that relies directly on the analysis of ion intensity as would determine spatial resolution in IMS. Any effects from the complexity of the beam shape, its pattern, and heterogeneity as they influence spatial resolution in imaging are effectively considered in a particular direction by the described line grating approach.

We attempted Gaussian-based fits to irregularly shaped beams shown in Figure 4.8. For a Mod 5 displayed in Figure 4.7f, the Gaussian fit is shown in Figure 4.8a. The R-squared value is 0.72 in Figure 4.8a, compared to > 0.99 for all Gaussian beams. Additionally, there is a large degree of uncertainty in σ ($\pm$ 9 μm). Figure 4.8b shows a Gaussian fit for a Mod 5 defocused beam corresponding to the shape illustrated in Figure 4.7h. In this case, Gaussian approximation was closer with the R-squared value of 0.92 and a smaller uncertainty in σ ($\pm$ 3 μm). In general, a true Gaussian beam has a R-squared value greater than 0.99. Lower R-squared suggest non-Gaussian beam profile and the resulting value of σ is only a gross estimate of the beam size.

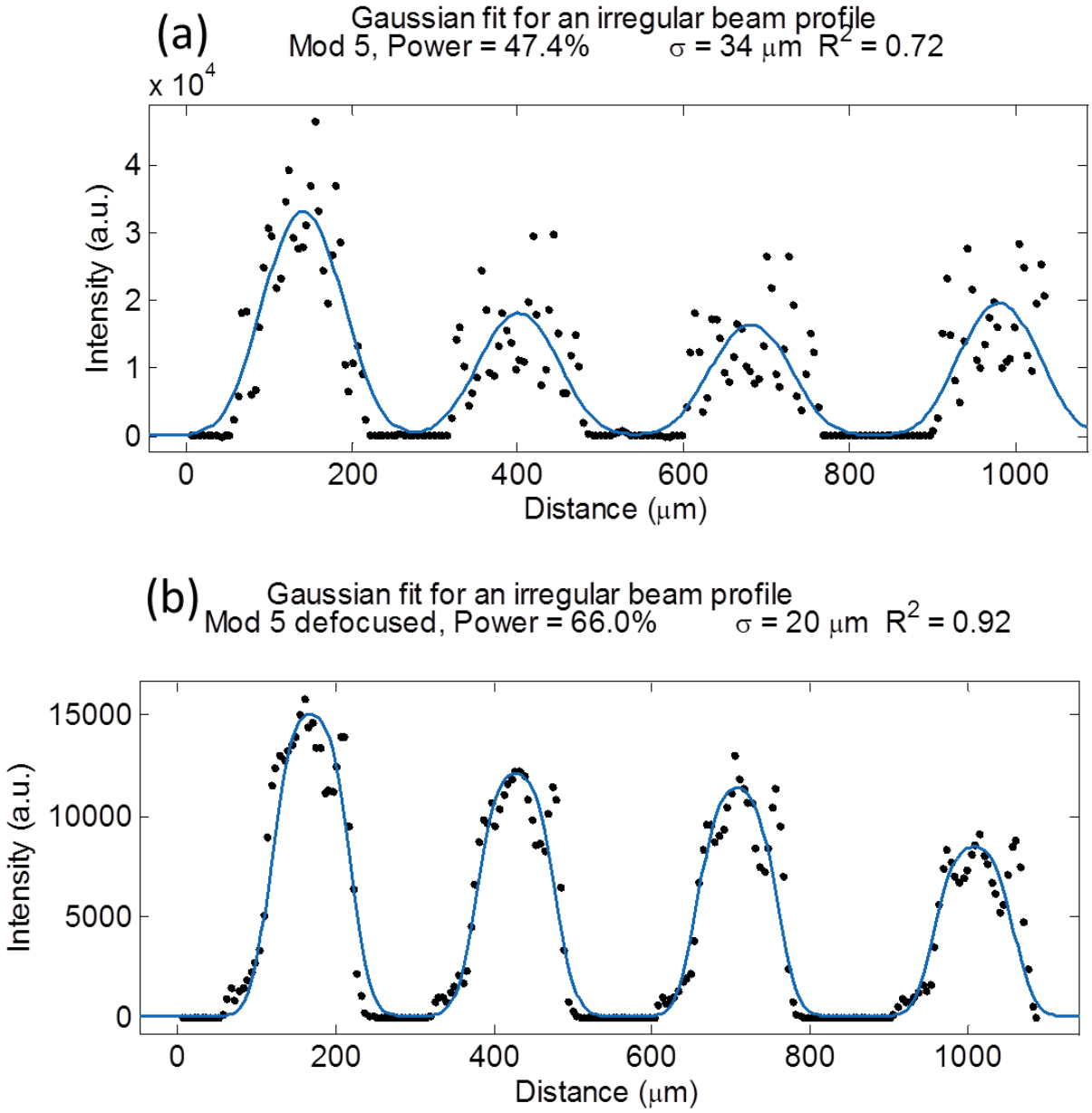

Figure 4.8. Application of a Gaussian model to the irregularly shaped beams. (a) Data corresponds to a 'Mod 5' beam as shown in Figure 4.7f. (b) Data corresponds to a 'Mod 5 defocused' beam as shown in Figure 4.7h.

4.3.6. Effect of Matrix Application on Spatial Resolution

The patterned organic material was used to test delocalization due to matrix application methods. Figure 4.11 compares an excessively wet spray-based method of matrix application

with a dry application process (sublimation). A lipid-soluble compound, Oil Red O, was patterned using diffusive stamping.[44] One slide was sprayed with sinapinic acid in 50% acetonitrile using an automated sprayer. A second slide was sublimated with a uniform coating of the same matrix material. The two slides were imaged using the Bruker Ultraflextreme MALDI-TOF instrument with a raster step size of 50 µm. The ion images show that the solvent based spray application caused extensive delocalization, essentially obliterating the Oil Red O pattern while the sublimated sample preserved the pattern. We can visually distinguish line widths up to 50 µm in the middle region. This experiment clearly shows the importance of carefully controlling the surface wetness with solvent spray devices. Drying periods of about 10 sec between spray deposits dramatically reduced this diffusion (data not shown).

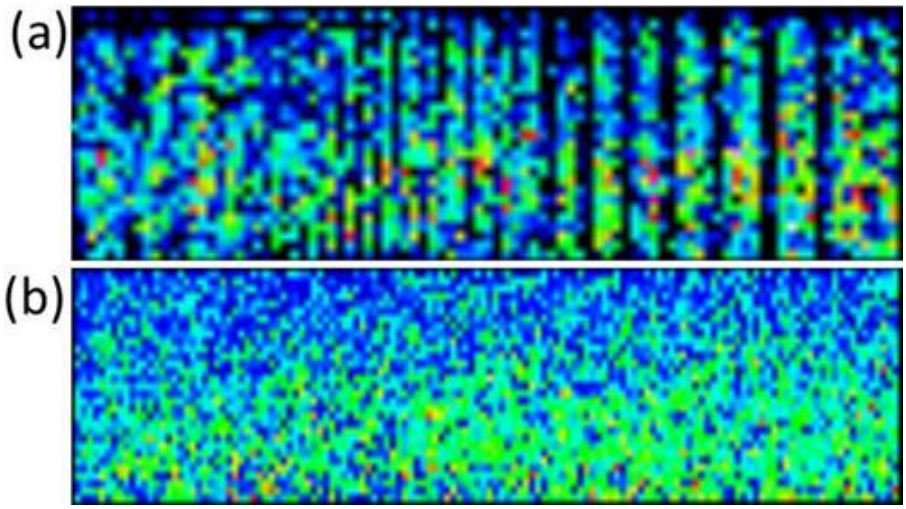

Figure 4.9. Evaluation of matrix application methods (a) Sublimation preserves the pattern of Oil Red O, and line-widths down to 50 µm are visible (b) Spray-based methods caused significant delocalization of the pattern due to wet spraying conditions.

4.3.7. Applications of the Reticle in Diagnosing Pixel Striping in High-throughput MS Instrumentation

Modern MS instruments can be operated at very rapid acquisition speeds (up to 100 pixels/sec). High throughput can be particularly useful when analyzing large tissue areas and for clinical studies that require the analysis of a large number of tissue specimens. In experimental tests with the reticle on a SimulTOF 300 Tandem instrument, we noticed that 'pixel striping' occurred at high acquisition rates (Figure 4.10a and 4.11b). The pixel striping manifested itself by the appearance of elongated pixels, that is, pixels that were longer than the defined instrumental spatial resolution of the experiment. Initially, we sought to quantify the degree of pixel striping by determining the number of pixels acquired in a constant area as a function of acquisition conditions (Figure 4.11). As the SimulTOF instrument utilizes continuous laser raster sampling, the spatial resolution is defined by:

$$Lateral\ Spatial\ Resolution = H.A.\left(\frac{v_{stage}}{f_{rep}}\right) \quad (4.2)$$

where v_{stage} is the sample stage velocity, f_{rep} is the laser repetition rate, and *H.A.* (hardware average) is the number of laser shots averaged for a single pixel.[53-54] In these experiments, the lateral spatial resolution and hardware averages were held constant (at 50 µm and 50 averages, respectively). The laser repetition rate and stage velocity were altered systematically to sample different pixel acquisition rates (*e.g.*, given the constant 50 hardware averages utilized, a stage velocity of 0.5 mm/s and a laser repetition rate of 500 Hz resulted in 50 µm pixels being acquired at 10 pixels/s). Solely based off of these initial pixel numbers reported in Figure 4.11, it was clear that elongated pixels were affecting the image quality at higher acquisition speeds. However, the source of these errors was unclear: were the errors occurring at the beginning or

end of each continuously scanned line as the stage accelerated and decelerated? Did the errors occur at regular intervals throughout the image? By using known pattern provided by the reticle, we were able to determine that these elongated pixels appeared more at less at random (Figure 4.10a).

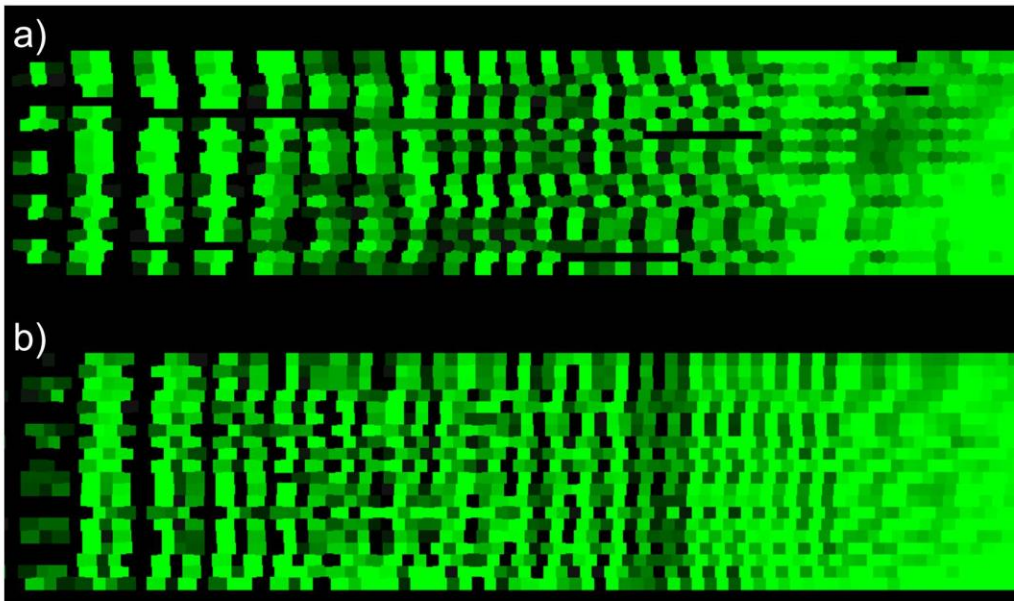

Figure 4.10. Display of 50 µm ion images of the reticle under instrumental conditions of (a) laser repetition rate of 4000 Hz, stage speed of 4 mm/s, 50 hardware averages, 80 pixel/s acquisition speed, 500 ps mass bin size and (b) laser repetition rate of 500 Hz, stage speed of 0.5 mm/s, 50 hardware averages, 10 pixel/s acquisition speed, 500 ps mass bin size. We note that the spatial resolution measured by the reticle in these examples will be larger than the spatial resolution defined by eq 4.2 because the instrument utilizes continuous raster sampling, and the employed laser power was insufficient to perform proper oversampling.

Through a series of investigations, we determined that the data acquisition step was responsible for the pixel elongations. Specifically, by varying the mass bin size at constant pixel acquisition speeds, we were able to alter the degree of pixel striping in the image. The mass bin size is the frequency at which data points are acquired across the mass spectrum. As the mass bin size was decreased, more data points across the mass range were sampled (and at a faster frequency) and the data size load on the digitizer was increased (Figure 4.11), which resulted in

an increase in pixel striping (Figure 4.10a versus 4.10b). As the data load was increased, the ability to efficiently write data from the digitizer to the computer hard disk was compromised. This information importantly allows us to determine under which instrumental operating conditions we can expect to obtain the highest quality MS images. Compared to the number of pixels theoretically required to sample the defined area (black dotted line in Figure 4.11), a threshold can be set for deeming the level of pixel striping satisfactory for quality IMS experiments. Setting this threshold at a pixel loss of 5%, at 10 pixels/s the mass bin size can be adjusted as small as 500 ps. At 20 pixels/s, the mass bin size must be 1000 ps or larger. At 40 pixels/s and above, the mass bin size must be at least 2000 ps.

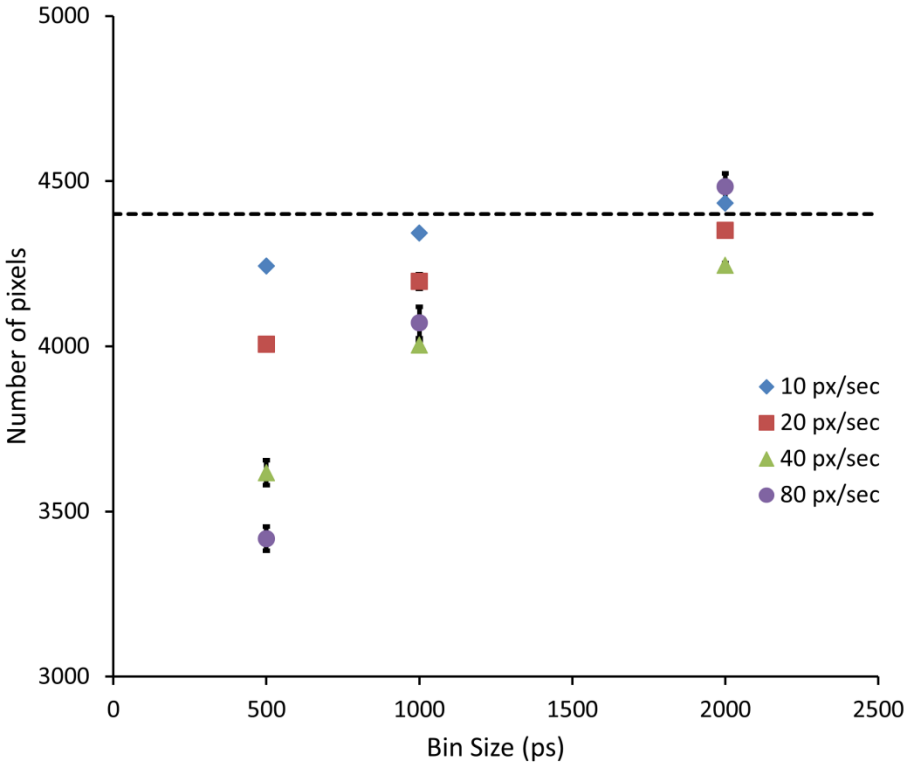

Figure 4.11. The number of pixels acquired in a defined 1 mm x 11 mm area as a function of mass bin size at different pixel acquisition rates. The theoretical number of pixels required to sample this 11 mm^2 area is shown as a black dotted line. Pixel numbers observed greater than this theoretical number are likely due to imperfect (smaller) pixel sizes being acquired at the beginning and end of each continuously scanned line as the stage is accelerated and decelerated.

4.4. Conclusions

A developed reticle consisting of patterned lines of crystal violet on a gold-coated slide provides a convenient method for measuring the beam diameter and spatial resolution for MALDI-IMS. The reticle is readily prepared using a combination of soft lithography to define and control feature sizes and selective dewetting to form a patterned coating of crystal violet on a conductive substrate. Crystal violet provides a suitable material for assessing spatial resolution in IMS as it is readily ionized and easily detected under conditions employed in MALDI IMS without requiring the presence of a supplemental matrix coating. The direct imaging of the crystal violet pattern avoids delocalizing effects that could affect the pattern upon matrix application. In contrast to other approaches, the described crystal violet-based reticle requires no overlay of a grid to mask off regions for presenting a pattern and thereby is not subject to the distorting effects that an applied grid can produce. The thickness of the crystal violet pattern is sufficient that its features and dimensions can be examined and verified by optical microscopy.

Various methods are presented that can be used with the reticle for measurement of spatial resolution in IMS in an objective manner. The edge spread method enables determination of the effective Gaussian-based full-width half-maximum of the incident beam by measuring the change in signal intensity from 12% to 88% across the edge of the crystal violet pattern. This approach has been generalized for use across a series of edges by convoluting the pattern of the object with a point spread function (PSF) to describe the beam profile. With the reticle, a one-dimensional PSF is employed for evaluating multiple edges simultaneously. The defined spacings on the reticle between separated edges are used to improve the effectiveness of this method as they reduce uncertainties in assigning the edge positions. In a direct test of spatial resolution, the various separation distances on the reticle between patterned crystal violet

features provide an outcome-based test that can distinguish the limits of spatial resolution under particular instrumental conditions. This line grating approach provides a direct demonstration of instrument performance. Both methods rely on the use of defined thresholds or mathematical fitting to provide objective measurements of spatial resolution that could be developed to allow automated operation. Their implementation requires no post-analysis of the reticle outside the mass spectrometer, in comparison with approaches that determine the size of ablated features by microscopy, which are often subjective. In contrast to such methods, the determined spatial resolution using the reticle relies on the analysis of obtained signal rather than on secondary factors such as beam size or ablation patterns that play a role in spatial resolution but are not direct measures of spatial resolution. For irregularly shaped laser beams, the reticle provides a measure of spatial resolution that factors in the area where the majority of the signal is generated.

The reticle has been used to obtain measurements of a spatial resolution under a variety of defined experimental conditions including different laser focus and power settings. The results exhibit qualitative agreement with changes in beam shape and size, providing a more relevant measurement. We note that while the spatial resolution measurements using the reticle may not be directly transferrable to the spatial resolution on tissue or other specimens (due to differences in ionization efficiency, the presence of matrix, etc.), the methods described here can provide an accurate evaluation of instrument setup They further allow assessment of differences in instrument performance that can influence image quality between different samples as well as between measurements performed on different dates or from different instruments. The determination of how the relative spatial resolution is affected as instrumental hardware and software conditions are varied is critical. In particular, instrumental conditions that cause unsatisfactory ‘pixel striping’ on a MALDI-TOF mass spectrometer were diagnosed. By

providing an objective evaluation of spatial resolution, the reticle will be exceedingly useful in the development of future IMS instruments and in benchmarking their performance. Future directions for this work include having feature sizes below 25 μm as needed for anticipated higher resolution IMS instruments under development.

CHAPTER 5. ENZYMATIC DIGESTION IN IONIC MATRIX

5.1. Background

Enzymatic digestion of proteins is critical for the analysis of large proteins that cannot be detected in intact form, the identification of proteins directly from tissue, and the analysis of formalin-fixed tissues where proteins are crosslinked. The current method for digestion of proteins within the tissue and their subsequent MALDI analysis involves serial spotting of enzyme and matrix.[55-56] This process takes a long time—4-8 hours for a single tissue section. Typically, trypsin is used as an enzyme requiring a pH of 7.5-8.5 for optimal activity. Common matrices for peptide analysis such as CHCA are acidic and thus spotted after trypsin application.

In this chapter, a method is developed whereby enzyme and matrix can be applied simultaneously. One-step application of all reagents will simplify the process and enable significant savings in time. As noted, the major challenge with the one-step application is that acidic matrix would inhibit trypsin activity. To address this challenge, CHCA is paired with a base resulting in an ionic matrix. The activity of trypsin in the ionic matrix is examined and the ability of the ionic matrix to generate ions for tryptic fragments is investigated.

5.2. Trypsin as an Enzyme

Trypsin is a serine protease that is found in digestive systems of many vertebrates and is frequently extracted from cow's or pig's pancreas. It is the most extensively used enzyme in proteomics applications because of its high specificity. Additionally, trypsin generates peptides in the mass range of 500-3000 that is amenable to mass spectrometry analysis. It cleaves mainly

at the carboxyl side of the amino acids lysine and arginine except when either if followed by proline.

The optimal pH for trypsin activity is between 7.5-8.5.[57] An aqueous buffer solution is used—typically 50 mM triethylammonium bicarbonate or 12.5 mM ammonium bicarbonate—to ensure optimal digestion conditions. Trypsin is added to the protein mixture in 1:20 mass ratio. The digestion can be in solution, in-gel or directly on tissue. Some of the trypsin may digest itself in a process known as autolysis.

Optimal temperature for both in-solution and in-gel digestion is 37 °C although trypsin that has been modified by reductive methylation has optimal activity between 50-60 °C with enzymatic digestion 12 times faster than that at 37 °C.[58-59] While aqueous buffer solution is typically used for digestion some studies claim that digestion is more efficient in organic solvents. In particular, Strader et al.[60] found that 80% acetonitrile consistently provided greater precent converage relative to any other solvent system.

5.3. Buffering Capacity of Ionic Matrix

The challenge in combining enzyme and matrix in the same solution is that typical matrices such CHCA and DHB are acidic inhibiting trypsin activity. A base was used to convert the matrix into its ionic form to overcome the acidic environment. Crank et al. [61] tested a range of bases and discovered several bulky bases can be paired with CHCA to form an ionic liquid matrix. Diisopropylethylamine (DIEA) was selected as a base because its bulky structure yielded an ionic liquid after reaction with CHCA.[62] Its hygroscopic environment would be favorable for the extraction of peptides and proteins from the tissue and could provide suitable conditions for trypsin activity. Additionally, DIEA is volatile and can be readily added to CHCA from the

vapor phase. The resulting liquid was found to have a compatible pH and a buffering capacity. Figure 5.1 compares the buffering capacity of this ionic matrix with ammonium bicarbonate, a common buffer used for tryptic digestion. 10 ml solutions of DIEA-CHCA and NH_4HCO_3 (both at 100 mM concentration) were used. Ionic matrix maintained pH between 6-9 as up to 2 mL of 1% base or acid was added. The buffering capacity of ionic matrix ensured stable pH as it was applied to the tissue.

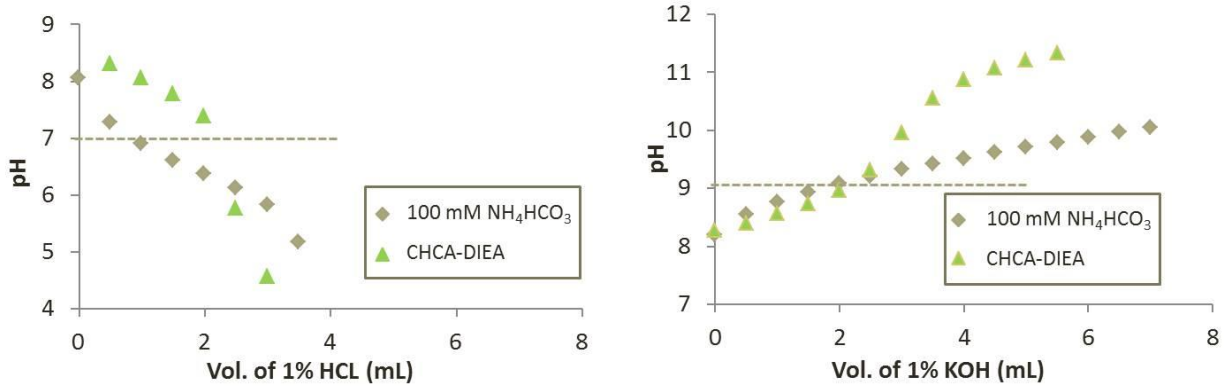

Figure 5.1. Comparison of the buffering capacity of DIEA-CHCA ionic matrix and ammonium bicarbonate buffer. 10 mL of each solution was used for titration and both solutions had a concentration of 100 mM. The ionic matrix maintained a pH between 6 and 9 through addition of 2 mL of 0.3 M HCl or 0.2 M KOH.

5.4. Detection of Tryptic Peptides in Ionic Matrix

While the ionic matrix provided a suitable pH for tryptic digestion, it was found to be unsuitable for detection of peptides using MALDI-MS. The MS signal was noisy in most locations on the target plate and only a few droplets provided a detectable MS signal. An acid rinse was deemed necessary to remove the base and convert the matrix into its crystalline form even though the rinse may dissolve the peptides. A number of solvent rinses were implemented including 1-25% trifluoroacetic acid (TFA) and 1-25% acetic acid (AcOH) to determine suitable conditions for the acid rinse. The slide was immersed in the acid solution for 1 min. After 1 min,

the slide was removed from the solvent and placed in a vertical position to allow the residual acid to trickle off. Finally, the slide was air dried, and optical images were acquired.

Figure 5.2 shows the results of these acid rinses. The control sample contained an equivalent amount of CHCA without any DIEA providing a basis of comparison for the amount of matrix lost during the rinse. The majority of the matrix was lost for acetic acid rinses. TFA performed significantly better in retaining the matrix. Some of the matrix was also lost in the case of 1% TFA and 5% TFA; concentrations of 10% or above showed a minimal loss. Since TFA is 1000 times more acidic than AcOH based on pK_a values, the rate of reaction between the acid and ionic matrix was expected to be much faster in the case of TFA. On the other hand, the rate of dissolution was expected to be comparable between the two acids. In the case of AcOH, the ionic matrix likely dissolved into the solution before it was converted to the crystalline state. On the other hand, TFA rapidly converted the ionic matrix into its crystalline form that was insoluble in the acidic solution.

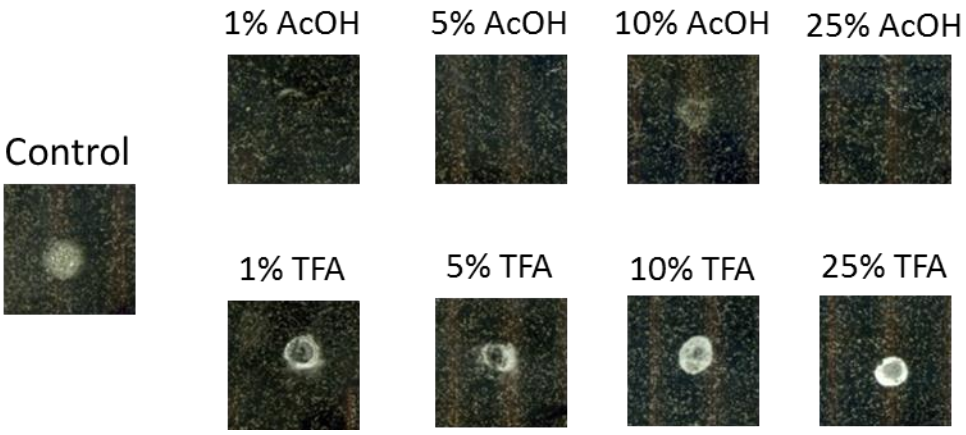

Figure 5.2. A hand-spotted droplet of CHCA (control sample) is shown on the left. Ionic matrix droplets (1 μL) were spotted onto the slides that were immersed in the acidic solutions for 1 min. The slides were dried after the acidic rinse and the optical images were acquired. The control sample had the same amount of CHCA but did not undergo the conversion and the rinse steps.

The optical images suggest that TFA at 10% or higher concentration provided maximum retention of the matrix post-rinse. The effect of acid rinse on the MS signal was also examined. Mass spectra were collected for three cases: (a) CHCA and standard peptides (control), (b) CHCA and standard peptides rinsed with TFA, (c) CHCA and standard peptides mixture that was converted to the ionic matrix and then rinsed with TFA. The standard peptides included Angiotensin II from humans at m/z 1046.54, [Glu1]-FibrinopeptideB at m/z of 1570.68 and Insulin Chain B at m/z of 3494.66.

Figure 5.3 shows the results of these experiments. The top panel illustrates the spectrum for the control experiment where the standard peptides and CHCA were mixed; all three standard peptides were observed. The intensity of the standard peptides decreases as m/z increases due to instrumentation bias against large peptides. The second panel shows the results after the spots containing matrix and standard peptides were rinsed. Visually, there was no major loss of CHCA crystals during the TFA rinse. An additional peak at m/z 644 was observed after washing that was due to the formation of matrix adduct corresponding to 3M + 2K.[63] The MS spectrum in the third panel corresponds to the experiment where the standard and CHCA mixture was hydrated with (DIEA) and then rinsed with TFA. All three peaks for the standard peptides as well as the matrix adduct at 644 Da were observed. An additional peak was observed at m/z of 3533 likely corresponding to insulin adduct with a potassium ion. These results suggest that conversion to the ionic matrix and the acid rinse does not remove peptides.

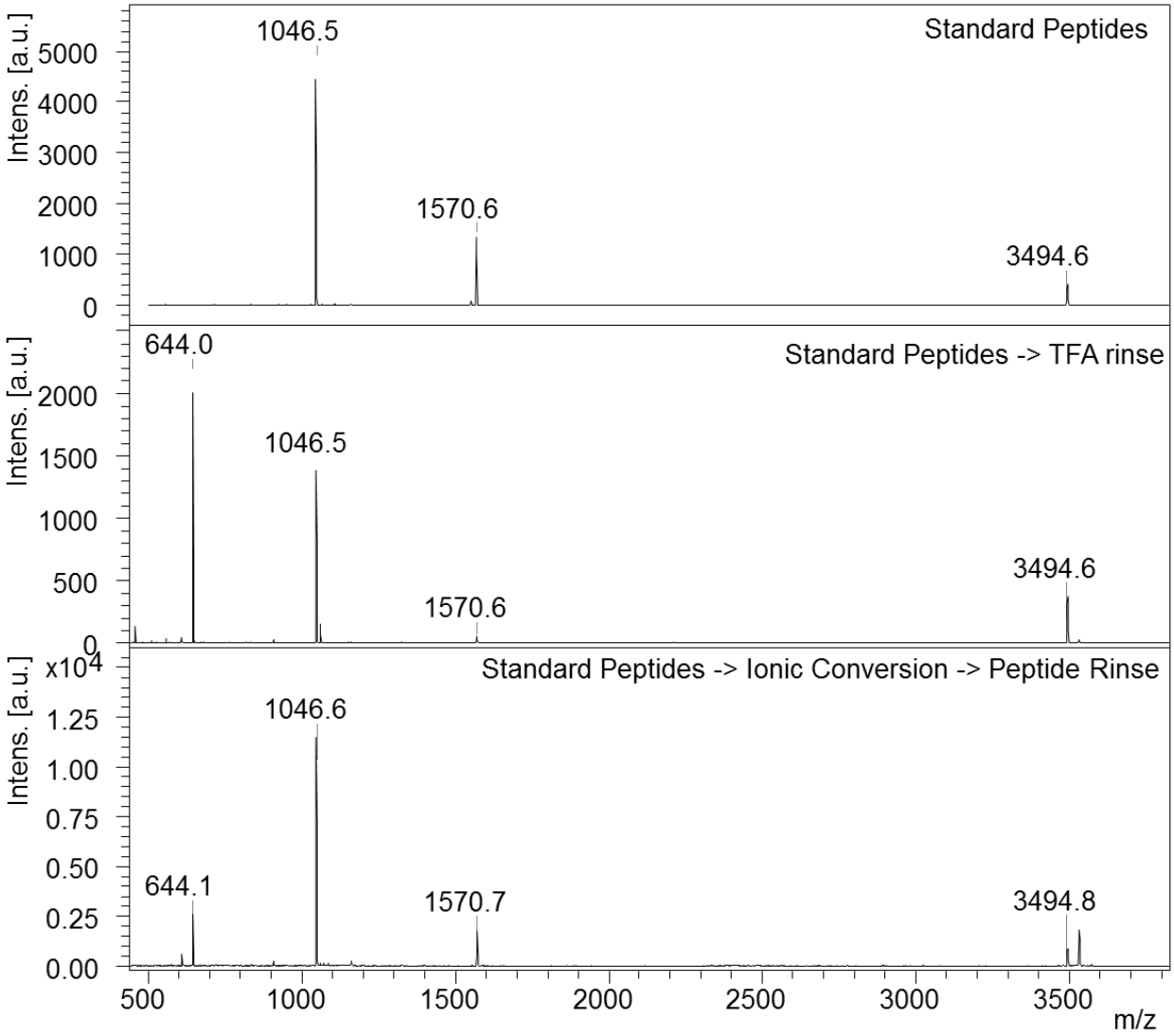

Figure 5.3. Effect of TFA rinses on mass spectrometry signal for standard peptides. Standard peptides include angiotensin II (1046.5 Da), fibrinopeptide B (1570.7 Da) and insulin chain B (3494.7 Da). The top panel shows the spectrum for control experiment with CHCA and standard peptides without an acidic rinse. The middle panel shows the spectrum after TFA rinse. The peak at 644 Da was due to the formation of matrix adduct (3M +2K). The bottom panel illustrates the spectrum after conversion of CHCA to the ionic matrix and TFA rinse. All three standard peptides were observed. The peak at m/z of 3533 was likely due to the formation of potassium adduct with insulin.

5.5. Digestion of a Protein Standard in Ionic Matrix

The optimal pH for trypsin activity is between 7.5-8.5.[57] As such, the ability to fabricate a functional pre-coated slide containing both matrix and trypsin poses a challenge as most MALDI matrices used for peptide analysis (such as CHCA and DHB) are acidic in nature and would therefore inhibit trypsin activity. To address this issue, previous studies involving *in situ* digestion by trypsin for MALDI-IMS have employed separate steps to apply the trypsin and the matrix to tissue samples.[64-65] In order to allow both matrix and trypsin, we used a base to neutralize the acidity of the CHCA to maintain trypsin activity. We selected diisopropylethylamine (DIEA) as the base because its bulky structure yields an ionic liquid upon reaction with CHCA.[61-62] We hypothesized that its hygroscopic environment would be favorable for the extraction of peptides and proteins from the tissue and provide suitable conditions for trypsin activity. DIEA offered other benefits as it is volatile and can be readily added to CHCA from the vapor phase. We measured the ionic liquid formed from CHCA and DIEA to have a pH of 8 and a buffering capacity similar to that of ammonium bicarbonate.

Using cytochrome c as a convenient protein of known sequence and readily identifiable fragments, we evaluated the activity of trypsin in the CHCA-DIEA ionic liquid medium. Ionic matrices have shown promise for the detection of lipids, proteins, and peptides by MALDI IMS from tissue samples.[62, 66] As we obtained low MS signals directly from the CHCA-DIEA ionic matrix, conversion to crystalline CHCA by a rinse with 10% TFA was necessary to detect peptides. Figure 5.4 compares mass spectral results for trypsin digestion of cytochrome c in the CHCA-DIEA ionic matrix with control experiments performed without trypsin or cytochrome c. In the case of CHCA-DIEA (Figure 5.4a), only matrix adducts were observed as expected. When trypsin was added to the ionic matrix (Figure 5.4b), trypsin autolysis peaks were present at m/z

659, 2163 and 2273 Da. When both trypsin and cytochrome c were present, several tryptic fragments from cytochrome c were observed in the mass spectrum (Figure 5.4c). These peaks highlighted in Figure 5.4c by asterisks were not observed in the control spectra. No autolysis peaks are evident in Figure 1c when both cytochrome c and trypsin were present as the signal due to digestion of the cytochrome c were much stronger than those in Figure 5.4b. The results show that CHCA-DIEA provides a suitable environment for trypsin digestion.

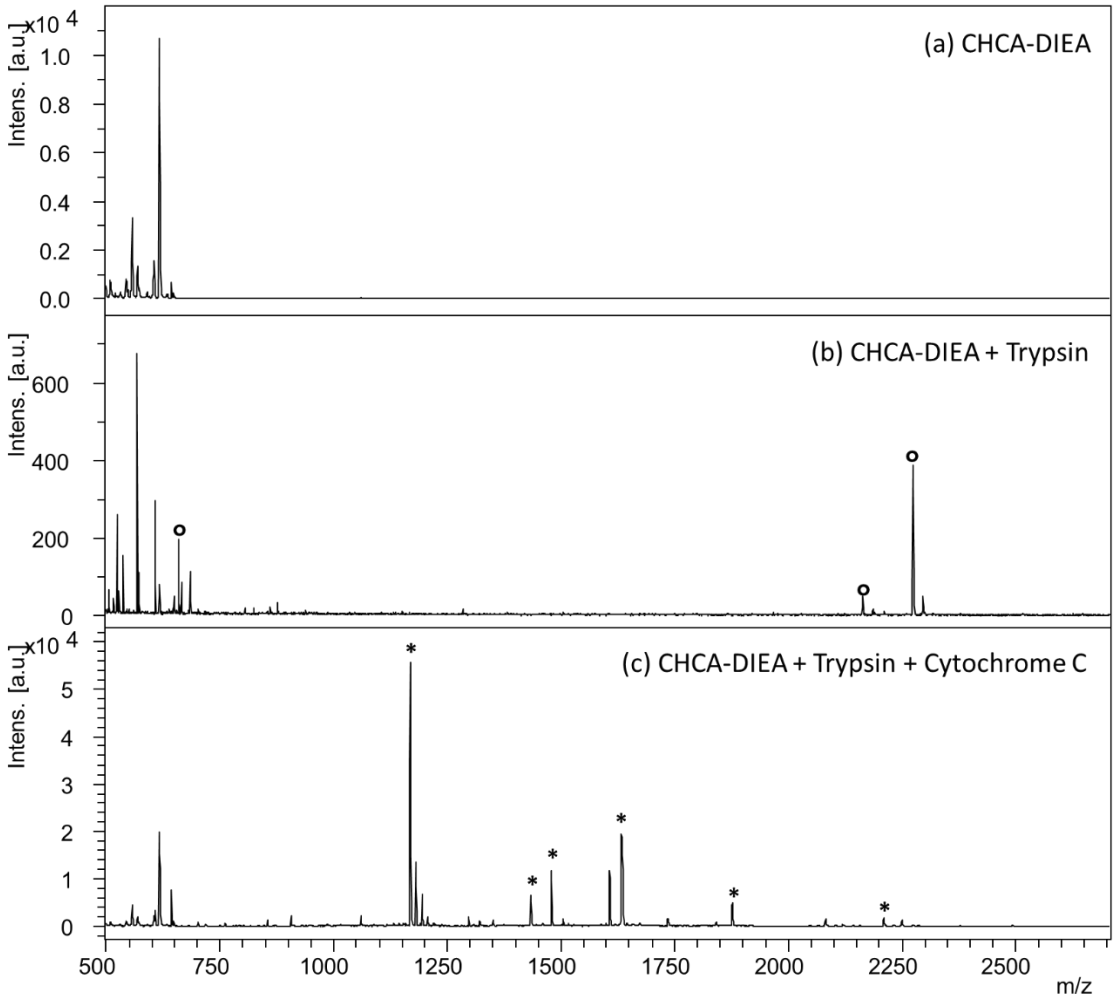

Figure 5.4. MALDI-TOF spectra show digestion of cytochrome c in ionic matrix medium. The mass spectra for (a) CHCA-DIEA, (b) CHCA-DIEA and trypsin, and (c) CHCA-DIEA, trypsin, and cytochrome c are shown above. The samples were incubated for 24 h at 37 °C. The autolysis products are marked with degree sign, and tryptic fragments of cytochrome c are marked with asterisks. In all cases, 1 µL of the solution was spotted on the plate; the plate was immersed in cold 10% TFA to convert the matrix into its crystalline form before MALDI analysis.

5.6. On-tissue Digestion Using the Ionic Matrix

After the successful digestion of cytochrome c, a similar spotting experiment was performed on rat brain tissue. 1 uL solutions of the ionic matrix with trypsin and ionic matrix without trypsin were separately spotted on the cerebellum of the serial rat brain sections. The

samples were incubated for 2 hours at 37 °C and spectra were collected using MALDI-TOF/TOF.

Figure 5.5 shows the result of this experiment. Figure 5.5a shows the control case of the ionic matrix without any trypsin. Only lipid signals were observed around 700 Da, and the rest of the spectrum was blank. Figure 5.5b shows the results for a spotting experiment using the conventional method of trypsin in buffer followed by matrix deposition. Additional peaks were seen in the peptide range in the spectra with trypsin; these new peaks did not match to any of the autolytic peaks so were likely tryptic fragments of proteins within the tissue. Figure 5.5c shows the results for the case of trypsin and ionic matrix deposited in a single step. Additional peaks were observed in this case suggesting successful digestion. None of these peaks match to autolysis products.

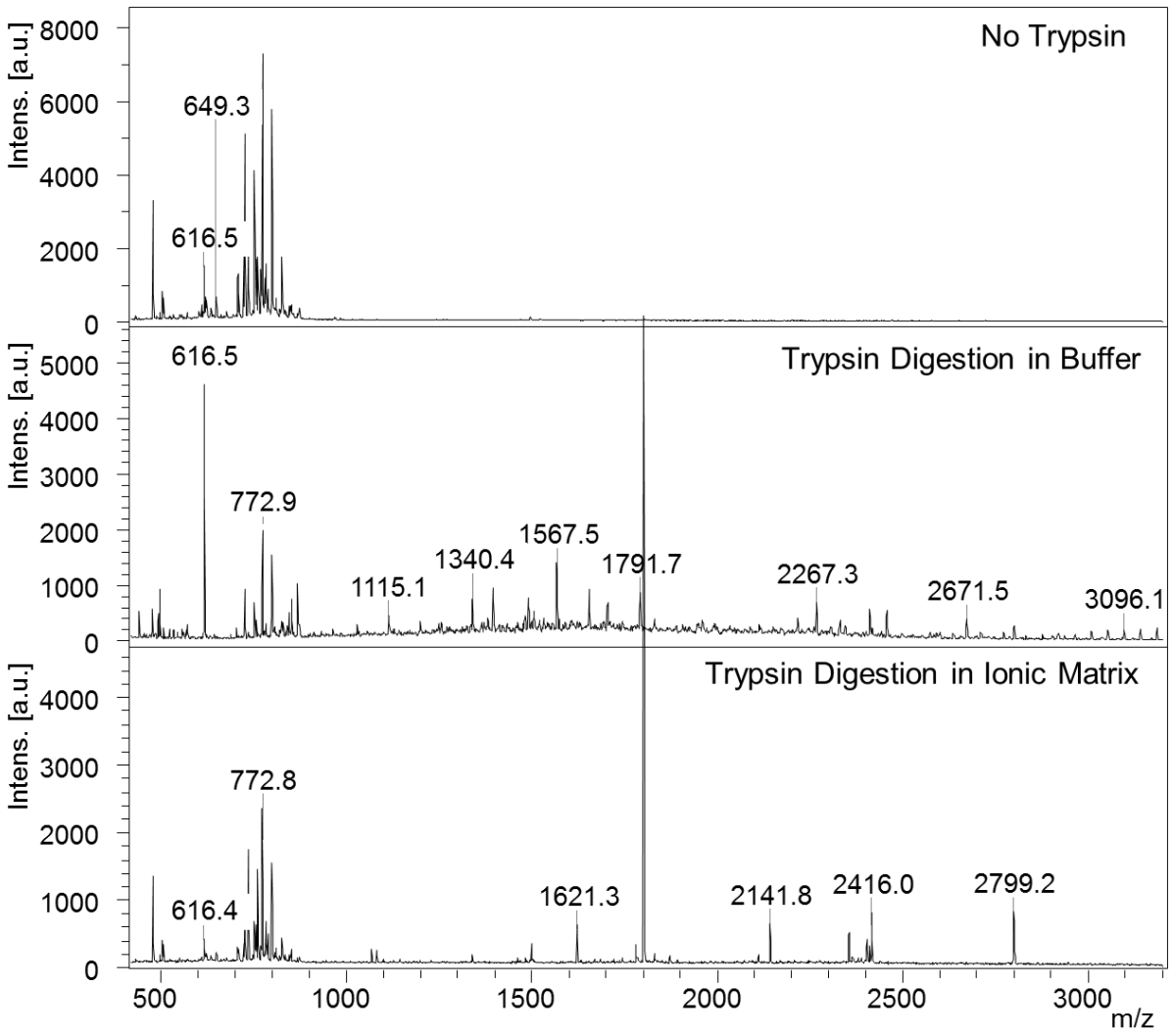

Figure 5.5. Hand-spotted experiments on rat brain tissue comparing tryptic digestion in a buffer solution with tryptic digestion in the ionic matrix. (a) A control experiment where only CHCA-DIEA was deposited without any trypsin. (b) Trypsin was deposited and after incubation matrix was spotted. (c) One-step process where trypsin and matrix were deposited simultaneously. After incubation, the slide was immersed in 10% TFA. In all cases, 1 μL solution was used, and digestion was conducted at 37 °C for 2 h. Serial sections of rat brain were used, and the solution was deposited in the similar area of the brain. Same concentration of trypsin was utilized in both (b) and (c).

CHAPTER 6. PRE-COATED SURFACES FOR PROTEIN DIGESTION AND PEPTIDE IMAGING

6.1. Introduction

Matrix-assisted laser desorption/ ionization imaging mass spectrometry (MALDI-IMS) is a powerful technology in biological research enabling imaging of biomolecules within thin tissue specimens. In a typical experiment, a thin tissue (3-12 um) is cryosectioned and placed on a conductive substrate. The tissue section is washed to remove salts and unwanted species, and then coated with a MALDI matrix that is typically a small organic molecule. The matrix aids in the desorption and ionization of the analytes. Analysis is performed by scanning a laser across the tissue section, acquiring mass spectral data at each defined x, y position. Two-dimensional maps of molecular distributions are generated from the spectral intensity for ions of interest across the sample.

In a typical MALDI imaging experiment, signals from proteins up to 25 kDa in molecular weight can be obtained directly from a tissue sample. Larger proteins are difficult to detect as the detection efficiency of a microchannel plate detector declines as the mass of the ion increases.[66] Additionally, larger proteins are difficult to solubilize and incorporate into the matrix crystals.[67] This limitation precludes the observation of higher molecular weight biological species such as cytokines, growth factors, enzymes, receptors, and other biomolecules. Specific sample preparation methods have been developed to detect proteins up to 70 kDa in mass. These include the application of ferulic acid as a matrix and use of Triton X-100 and xylene to solubilize large

proteins.[68-69] Due to inherent limitations in detection and ion optics, such large proteins are difficult to detect on a routine basis.[70]

An approach for measuring the distribution of large proteins (>25 kDa) in a tissue sample by MALDI-IMS involves their *in situ* tryptic digestion and subsequent MS imaging of generated fragments.[55] In this approach, trypsin is serially spotted onto a tissue section to digest the proteins. Robotic spotters are used to control the digestion conditions, and in a second step, spot matrix on top of these individual regions. These post-coating methods have been used for the analysis of both formalin-fixed[56, 71] and fresh-frozen tissues.[55] The advantages of this *in situ* digestion process include an on-tissue identification of proteins and a preservation of their spatial localization in contrast to LC-MS/MS approaches that are done on tissue homogenates where spatial information is limited. Further, the on-tissue analysis provides spatial distributions for the parent proteins and their daughter peptides that can be co-related and provide further verification in the identification. Despite these advantages, its use is challenged by a cumbersome process whereby sequentially spotting of matrix and trypsin onto a tissue sample can take hours for each tissue specimen. In addition, the robotic spotters needed for trypsin deposition are costly, and their spatial resolution is limited to 200-300 μm.

As an alternative to current post-tissue processing methods for MALDI-IMS, we are developing approaches that incorporate species such as matrix and enzymes onto targets prior to tissue availability. The goal is to simplify tissue preparation for MALDI-IMS and avoid time-consuming post-tissue deposition steps and the need for costly specialized equipment. In our lab, previous work has shown that matrix pre-coated targets can provide simple, standardized, and rapid methods for sample preparation. Grove et al. used pre-coated targets consisted of thin matrix films for the imaging of small molecules across a series of tissue sections.[72] Yang et al.

demonstrated the successful imaging of lipid and protein distributions in brain and kidney tissues using such pre-coated slides.[73-74] In this work, we detail the development of targets pre-coated with both an enzyme and matrix and their use for the indirect imaging of large proteins from generated tryptic fragments on frozen tissue samples.

The approach involves the sequential coating of an ITO slide with a matrix and trypsin using a robotic sprayer in advance of the tissue availability. Onto the pre-coated slide, a thin (3-4 μm) section of frozen tissue is then thaw-mounted directly. The slide is placed in a chamber saturated with diisopropylethylamine and water to allow the acidic matrix (CHCA) to convert into an ionic liquid. This conversion provides a suitable pH and liquid environment for tryptic digestion. The slide is then rinsed with a strong acid to return the CHCA matrix to its solid form. Peptides fragments generated during the trypsin digestion are then imaged directly from the slide using MALDI-IMS. Here we demonstrate the ability of matrix and trypsin pre-coated targets to digest proteins in rat brain samples and show the co-localization of generated daughter peptides as confirmation of the method.

6.2. Experimental Section

Materials

Acetonitrile (ACN), trifluoroacetic acid (TFA), α-cyano-4-hydroxycinnamic acid (CHCA), diisopropylethylamine (DIEA), trypsin from bovine pancreas, and cytochrome c from the equine heart were purchased from Sigma-Aldrich (St. Louis, MO). Conductive indium tin oxide (ITO)-coated microscope slides were purchased from Delta Technologies (Loveland, CO). Frozen rat brain was obtained from Pel-Freez (Rogers, AR) and stored at −80°C.

Digestion of Protein Standard

A test solution of ionic matrix consisting of 50 µM CHCA and 100 µM DIEA was prepared in water. Cytochrome C and trypsin at 10 µM and 0.5 µM, respectively, were added to allow digestion. After incubation for 24 h at 37 °C, 1 µL of the solution was spotted onto a MALDI target. Cold 10% TFA in water (0 °C) was spotted onto sample to convert the ionic matrix into its crystalline form. After 1 min of contact, the acid solution was decanted, and the MALDI plate was dried in a desiccator prior to analysis using a Bruker Ultraflextreme MALDI-TOF in reflectron mode.

Slide Fabrication

Matrix and trypsin are sequentially spray-coated on an ITO-coated glass slide using a HTX TM Sprayer (HTX Technologies, LLC, Chapel Hill, NC). CHCA was dissolved in a 9:1 acetonitrile:water solution at 10 mg/mL. To deposit the matrix, the sprayer was operated at a 0.2 mL/min flow rate using a HPLC pump, a 2 mm track spacing, a 1000 mm/min nozzle velocity, a 70 °C nozzle temperature, a 6 psig nebulizer pressure, and 90% ACN as a pushing solvent. The number of passes was varied between 10 to 20 to control the thickness of the matrix coating.

In a second step, trypsin as a 2 mg/mL solution in water was sprayed on top of the matrix coating. A syringe pump was used to accommodate the flow rate of 30 µL/min used for trypsin deposition. The sprayer conditions were 2 mm track spacing, 1000 mm/min nozzle velocity, 30 °C nozzle temperature, 6 psig nebulizer pressure, and water as a pushing solvent. The number of passes was varied between 4 to 12 to control the density of trypsin.

Tissue Mounting

Frozen rat brain tissue was sectioned to 4 µm at -20 °C using a Leica CM 3050S cryostat (Leica Microsystems GmbH, Wetzlar, Germany). A pre-coated slide in the cryostat chamber was

warmed for 2 s using a finger and placed directly on top of the sectioned tissue. The tissue adhered to the slightly warmer slide in preference to the cold metal plate. The tissue was then thaw-mounted on the slide using thermal energy from the finger.

In situ Tryptic digestion

The mounted tissue section was placed in a chamber saturated with diisopropylethylamine for 5 min to convert CHCA into its ionic liquid form. After conversion, the slide was placed in a plastic petri dish, sealed with tape, and kept in an oven for 3-16 h at 37 ℃. After cooling to room temperature, the slide was immersed in a solution of 10% TFA at 0 ℃ for 1 min to return the matrix to its crystalline form. The slide was dried in a desiccator before MALDI analysis.

MALDI IMS

Imaging experiments were performed using a 15T Bruker MALDI FTICR mass spectrometer (Bruker Daltonics, Billerica, MA, USA). The instrument is equipped with an Apollo II dual MALDI/ESI ion source and a Smartbeam II 2 kHz Nd:YAG (355 nm) laser. All images were collected using the small laser setting (~50 µm) with a pixel spacing of 100 µm in both x and y directions. Data were collected from m/z of 500 to 4000 with a resolving power of 130,000 at 1000 m/z. External calibration was performed prior to analysis using CsI clusters. FlexImaging 5.0 (Bruker Daltonics) was used to visualize ion images.

In-gel tissue extraction and LC-MS analysis

Polyacrylamide hydrogels were fabricated using the procedures described by Harris et al. and Taverna et al. [75-76] A cylindrical piece of polyacrylamide gel measuring 2 mm in diameter

and 2 mm in height was loaded with trypsin and placed onto the cerebellum region of a brain tissue section for 4 h. The gel was removed from the tissue and placed in an Eppendorf tube into which an extracting solution containing 50% ACN and 5% formic acid was pipetted to fully cover the hydrogel. After 15 min of gentle agitation, the solution was collected and replaced by a 100 mM ammonium bicarbonate solution. The Eppendorf tube was agitated for 15 min to re-swell the gel. This process of extraction and re-swelling was repeated 2 additional times. The extracts were dried down and reconstituted in 0.1% formic acid. The solution was analyzed using LC-MS/MS, and the results were analyzed using Scaffold 4.2.1(Proteome Software, Portland, Oregon).

Identification of tryptic peptides

Using the results from LC-MS/MS experiment, 20 most abundant proteins in the tissue sample were found based on unique spectra count. For each of the abundant proteins, tryptic peptide sequences were generated allowing for up to 2 missed cleavages using Mmass. Peak picking from FTICR average spectrum was performed in Mmass software, and this peak list was compared to the tryptic peptides list based on accurate mass allowing for up to 5 ppm error. Ion images were generated for selected matched peptides.

6.3. Results and Discussion

6.3.1. Fabrication and Application of the Pre-coated Slides

The advantage of pre-coated slides is that the matrix and enzyme can be applied prior to tissue. The slides can be prepared in batches and many samples prepared in a single experiment. In a typical preparation, matrix and trypsin were sequentially spray-coated onto an ITO-coated glass slide in two steps using a HTX TM Sprayer as shown schematically in Figure 6.1(a).

Typical CHCA and trypsin densities were ~0.35 mg/cm^2 and 30 µg/cm^2, respectively. Peptide signals from tissue samples were significantly lower when the enzyme and matrix were mixed and sprayed in one step compared to the case where enzyme and matrix were sprayed sequentially.

The amount of expected CHCA deposited on a slide was calculated based on instrumental conditions using the equation below:

$$Mass\ deposited\ = \frac{\#\ of\ passes\ x\ conc.x\ flow\ rate}{track\ spacing\ x\ stage\ velocity} \quad (6.1)$$

In practice, a fraction of the aerosolized matrix was deposited away from the slide. Table 6-1 compares the ratio of actual coverage of CHCA with that calculated using eq 6.1. The ratio of the actual and calculated coverages is defined as deposition efficiency. The deposition efficiency of the matrix application depended on both the nozzle temperature and the nebulizing pressure. The efficiency of the process increases from 44% to 74% as the pressure is reduced from 13 psig to 6 psig while the temperature is kept constant at 30 °C (cases 1 and 2). Again, the efficiency improves from 35% to 47% as the pressure is reduced from 13 psig to 10 psig while the temperature is kept constant at 70 °C (cases 3 and 4). As the nozzle temperature was increased from 30 °C to 70 °C while the pressure was kept constant at 13 psig, the efficiency of the process was reduced from 44% to 35%. Thus, lower temperature and pressure result in high efficiency.

Lower pressure and temperature resulted in wet spraying conditions which lead to inhomogeneous coating, particularly large crystal size. Due to a tradeoff between high efficiency and the homogeneity of the coating, a moderate pressure and temperature must be used. In

particular, a temperature of 70 °C and a pressure of 10 psig produced a homogenous coating with modest efficiency.

Table 6-1. Comparison of actual matrix density with calculated density for spray-coated slides. The ratio of actual and calculated density is defined as deposition efficiency. Flow rate was 0.2 mL/min in all cases.

Temp. (°C)	**Pressure (psig)**	**Deposition Efficiency**
30	13	44%
30	6	74%
70	13	35%
70	10	47%

The use of a pre-coated slide for tissue analysis is shown schematically in Figure 6.1(b). A thin tissue section was sectioned and thaw-mounted directly on top of a pre-coated slide. The slide was then placed in a chamber saturated with DIEA and water (5 min) during which the matrix turned into yellowish viscous liquid. After conversion to an ionic liquid, the slide was incubated in a sealed petri dish at 37 °C. Tryptic peptides were observed using incubation time as short as 3 hours; however, overnight incubation yielded greater extent of digestion as evidenced by greater signal intensities. After incubation, the slide was immersed in cold (~0 °C) 10% TFA for 1 min to remove DIEA and return CHCA to its crystalline state.

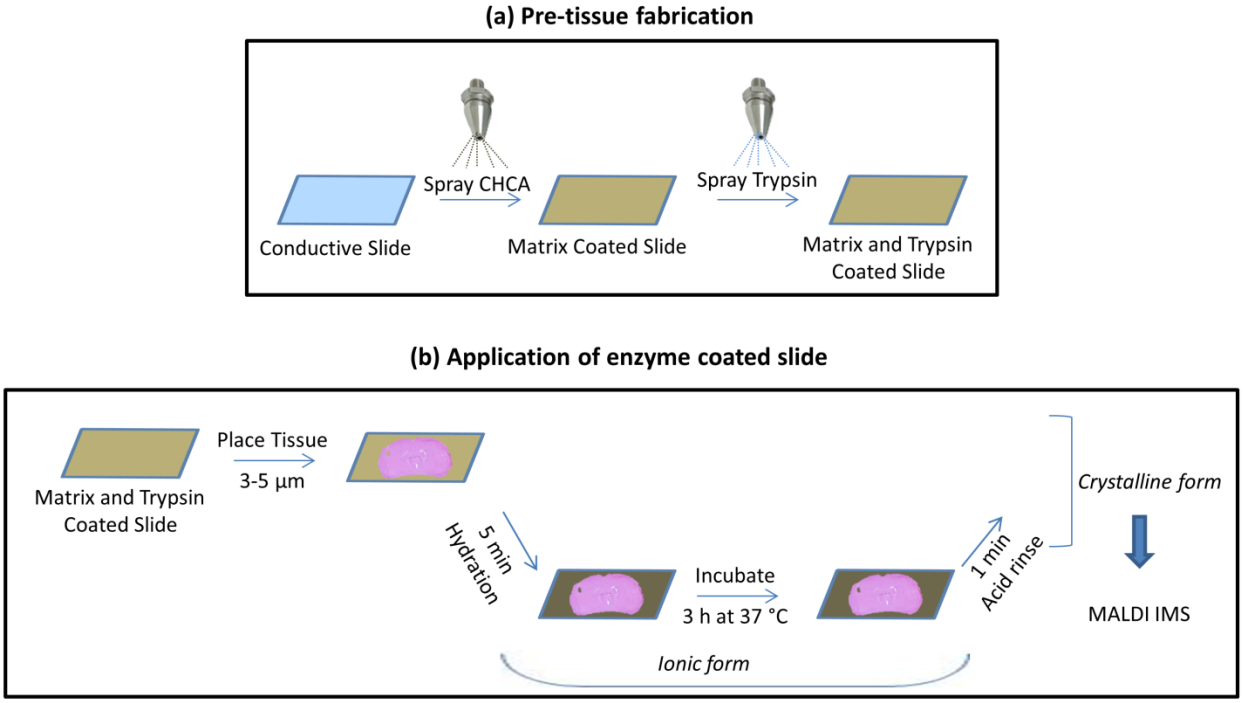

Figure 6.1. (a) Matrix and trypsin are sequentially sprayed onto a conductive substrate (b) General procedure for preparing a tissue sample for analysis using a pre-coated slide. The tissue sample is placed onto a pre-coated slide. It is hydrated by exposure to DIEA and water and then incubated in a sealed chamber for 3 to 16 h at 37 °C. Immersion in 10% TFA for 1 min returns the matrix to its crystalline form.

6.3.2. Effect of Matrix Concentration on the Peptide Spectra

Yang et al. found that matrix density on a pre-coated substrate affected the signal intensities for both proteins and lipids. For proteins, 1.1 mg/cm^2 or higher densities provided a good signal, but slides with lower matrix densities had reduced performance. For lipids, optimal matrix density was 0.3-0.4 mg/cm^2. Since peptides have mass ranges between proteins and lipids, we expected the optimal density to be between 0.3-1 mg/cm^2. In our experiments, CHCA concentrations in that range were examined as shown in Figure 6.2. Trypsin concentration was held constant at 15 µg/cm^2 and 4 µm thick rat brain sections were used in all three cases. Strong lipid signals between m/z 600-800 were observed for all three conditions. We were particularly interested in peptide signals between 900-3000 Da. We found that concentration between 0.3 –

0.4 mg/cm^2 provided the best peptide signals. Further reduction in matrix concentration was not feasible as the coverage becomes incomplete after conversion to the crystalline matrix. We hypothesize that the additional matrix reduces the effective trypsin concentration and thus lowers peptide signals. Alternatively, the thicker coatings are not fully converted to ionic matrix after 5 minutes causing non-optimal pH for digestion.

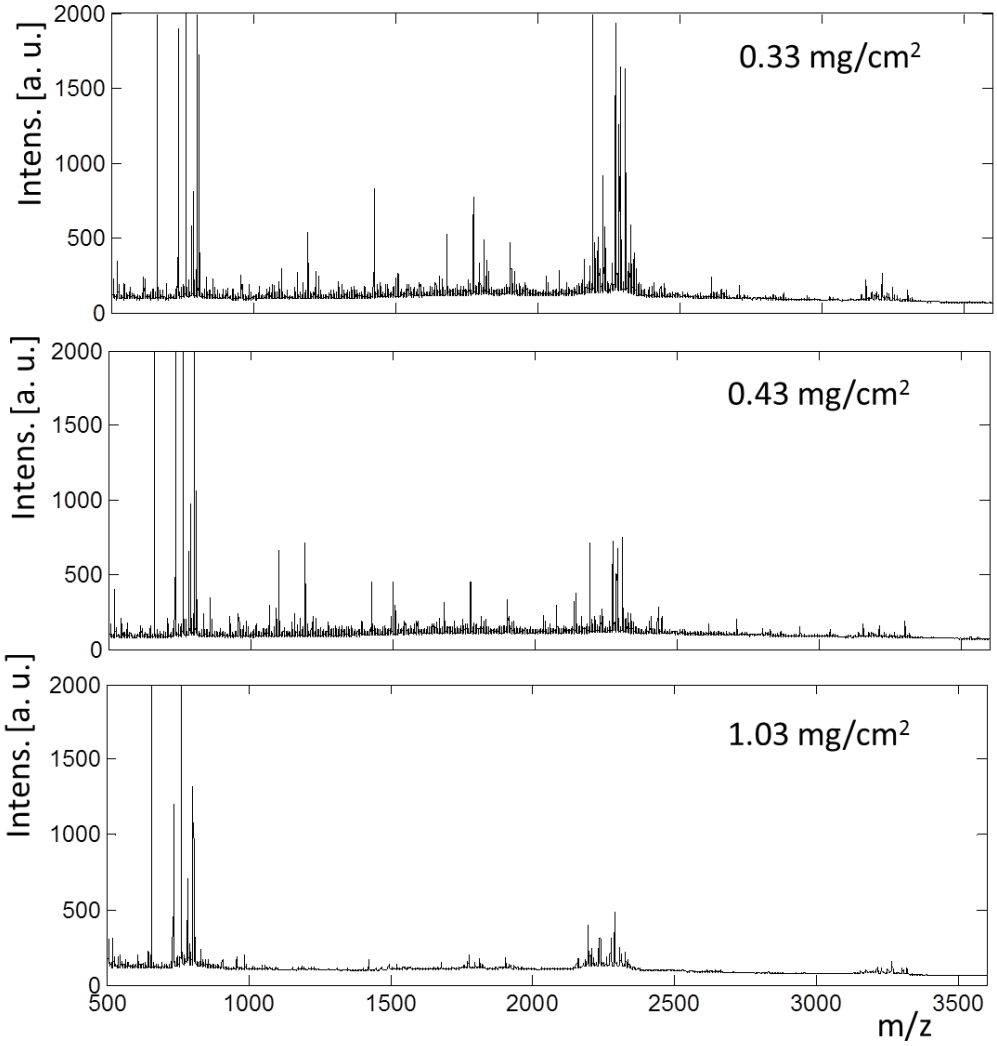

Figure 6.2. Effect of matrix concentration on peptide signal from rat brain tissue. Trypsin concentration was 15 µg/cm^2 in each case, and the tissue thickness was 4 µm. Digestion was done for 3 h at 37 °C. Data were collected on Bruker Rapiflex MALDI-TOF.

6.3.3. Effect of Trypsin Concentration on Peptide Signal

The amount of trypsin is an important parameter in controlling the rate and extent of digestion. Previous studies employing robotic spotters to deposit matrix and trypsin on tissue samples found that the optimal trypsin concentration was in the range 2 – 5 μg/cm^2.[77] Multiple passes of trypsin spotting were employed to enable optimal extraction. Since repeated extraction is not possible with pre-coated slides, we anticipated that higher concentration of trypsin would be needed. To address this issue, we investigated a range of enzyme concentrations from 0 to 30 μg/cm^2, where the matrix density (0.37 mg/cm^2) and digestion conditions (4 h at 37 °C) were held constant. Representative average spectra in Figure 6.3 show the changes effected by trypsin concentration. Without any enzyme, some signals are seen on m/z values between 700 and 900 Da that correspond to lipids. The strongest signals in the spectrum are from lipid dimers and appear between 1400 and 1700. As the trypsin concentration was increased from 0 to 30 μg/cm^2, the relative intensity of the lipid dimers decreased in the spectra. This decrease is due to an increased intensity of other signals from generated peptides. In the spectra, the peptide signals were strongest with an enzyme concentration of 30 μg/cm^2, although a trypsin concentration of 15 μg/cm^2 also yielded good signal. Increases in trypsin concentration above 30 μg/cm^2 are not recommended due to disproportionate increases in signals due to autolysis signals that complicate measurement of peptide signals from tissue.

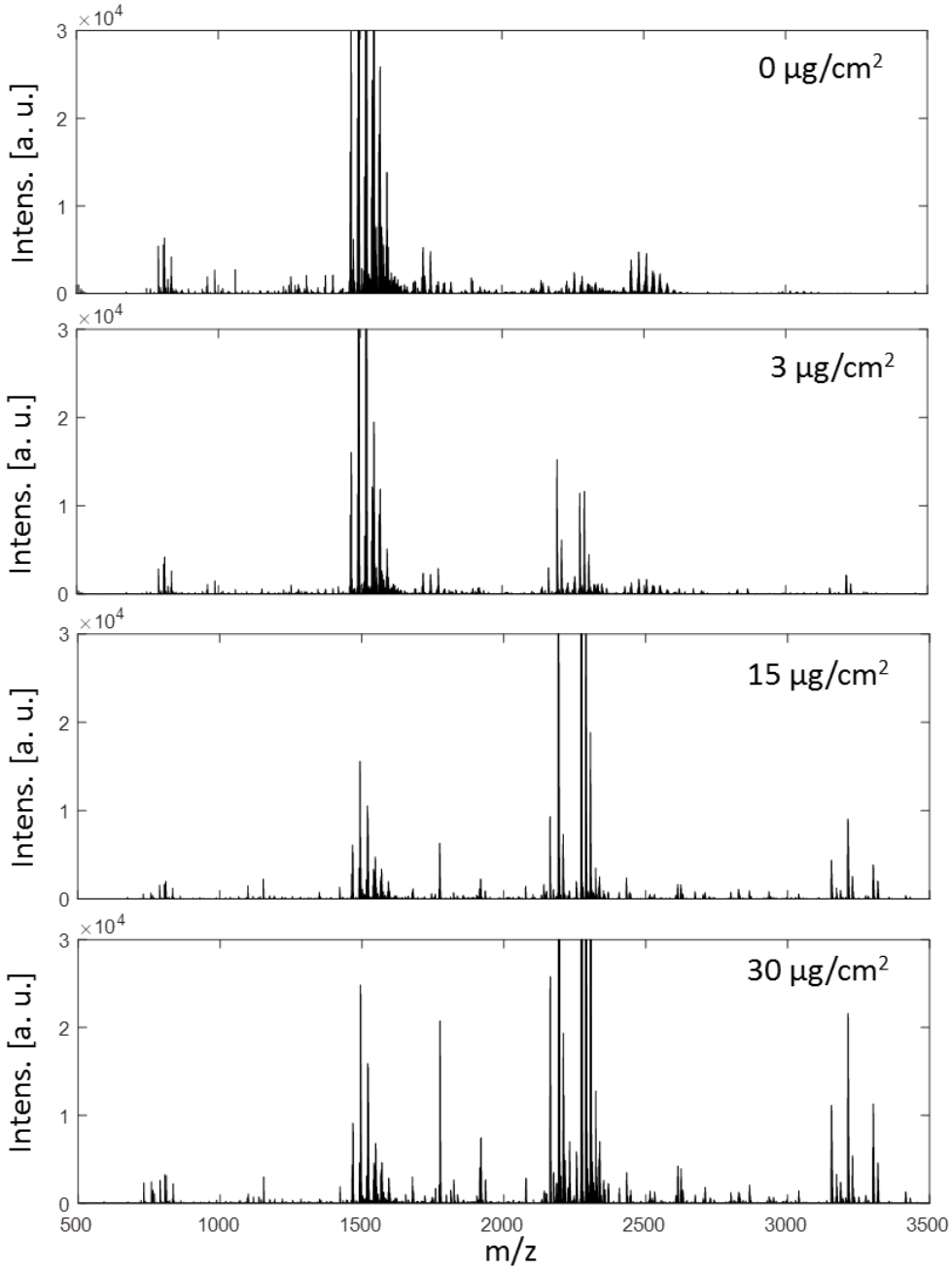

Figure 6.3. Effect of trypsin concentration on mass spectra obtained from rat brain tissue sections prepared using the pre-coated slides. Trypsin densities at the surface were: 0 μg/cm^2, 3 μg/cm^2, 15 μg/cm^2, and 30 μg/cm^2; CHCA density was 0.37 mg/cm^2. Digestions were conducted at 37 °C for 4 h.

6.3.4. Optimizing Hydration Time On-Tissue

The pre-coated slides are inserted in a glass container that is saturated with DIEA vapor to convert the acidic matrix to ionic matrix. The extent of conversion is directly dependent on the time in the hydration chamber. If the hydration time is too short, then the pH is likely acidic preventing activation of trypsin. If the hydration time is too long, the peptides may delocalize reducing the spatial resolution. Slides were placed in hydration chamber for a time ranging from 1 to 15 min to determine the optimal hydration time. Figure 6.4 shows the optical images for each condition after 20 hours of digestion with a 4 μm tissue section. After 1 min of hydration, the top layer of the matrix is converted to ionic liquid while the majority of the matrix remains in the crystalline form. The optical image shows dark tissue on top of the matrix coating. As the time of hydration increases, greater fraction of the crystalline matrix is converted into the ionic liquid promoting greater mixing between the tissue and the liquid. In the presence of ionic liquid, the tissue appears more transparent.

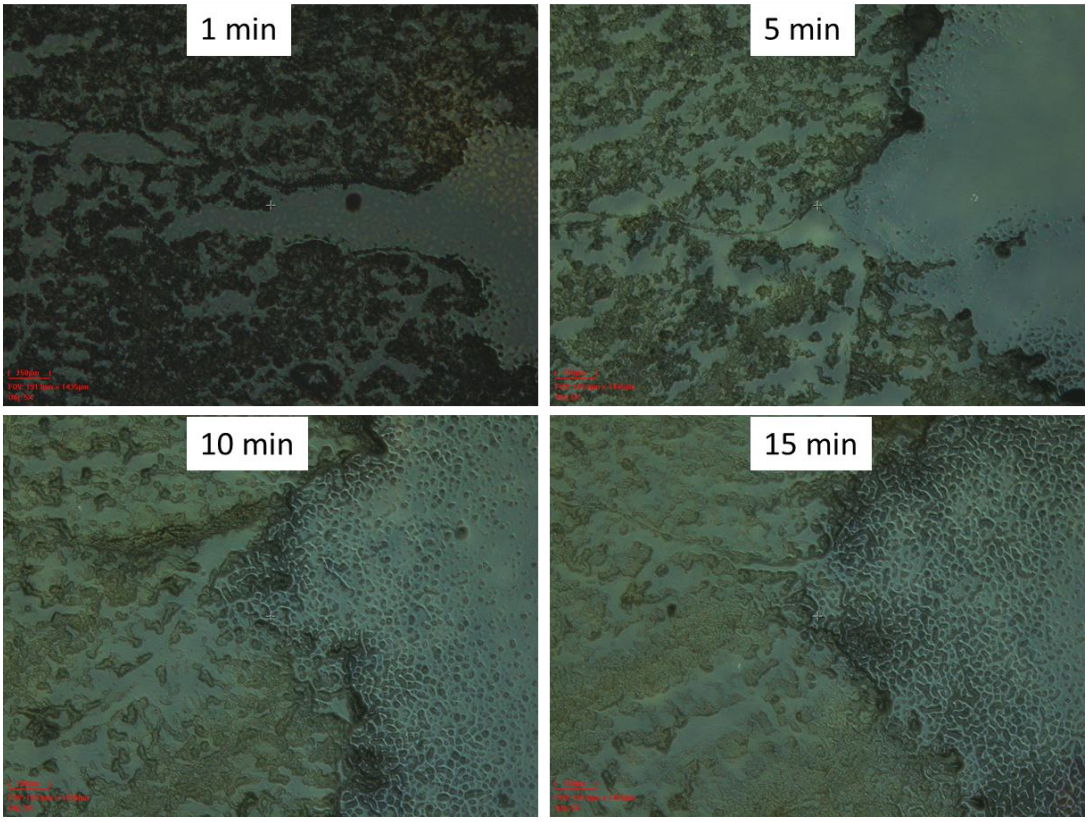

Figure 6.4. Optical images of the serial rat brain tissue sections after hydration for different lengths of time.

Figure 6.5 shows the mass spectrum for each of the conditions acquired using a MALDI-TOF/TOF instrument. After 1 min of hydration, very few peaks are observed. After 5 min, significantly more peaks were observed between m/z 800-4000. After 10 min, the peak intensity increased further for some of the peptides. We compared the relative ion intensity of tryptic peptides from myelin basic protein to make a more detailed comparison. The results are shown in Table 6-2 for 5 min and 10 min hydration. For the four selected peptides, 10 min hydration yields higher signal-to-noise ratio. In particular, for m/z at 1502.77 and 2141.08, the signal-to-noise ratio was about 3 times greater for the 10 min hydration relative to 5 min hydration. Based on the spectral quality and the tabulated data, we can conclude that 1 min hydration provided

minimal digestion, and 10 min hydration yielded greater extent of digestion relative to 5 min hydration.

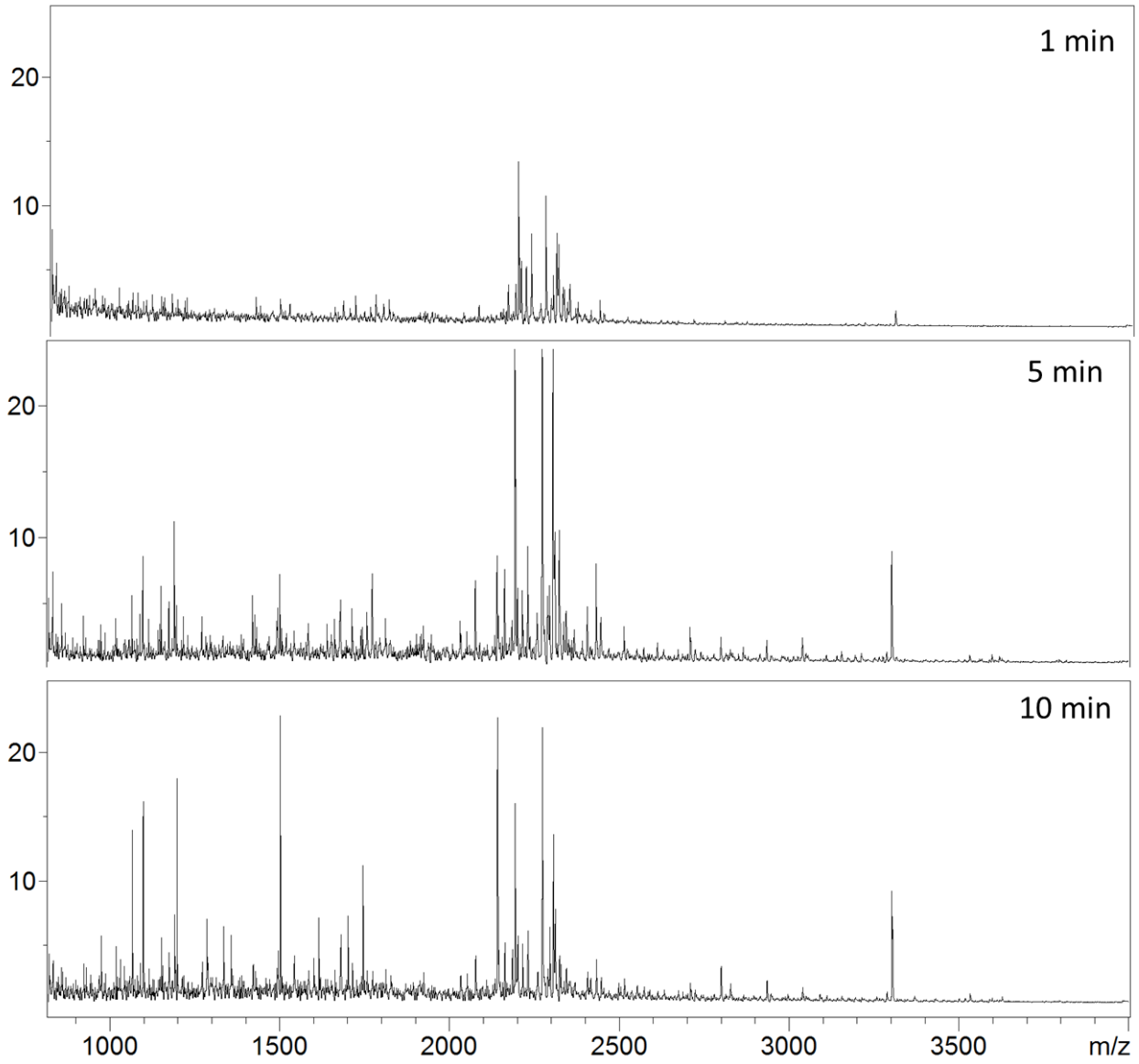

Figure 6.5. Mass spectra acquired from rat brain tissue sections using the pre-coated slides after hydration for different lengths of time.

Table 6-2. Tryptic fragments of myelin basic protein.

5 min		10 min	
m/z	S/N,	m/z	S/N, 10 min
861.44	4.6	1019.55	5.2
1502.77	8.8	1502.77	25.8
2141.08	6.1	2141.11	22.6
2933.50	4.9	2933.50	4.1

Figure 6.6 compares the spatial localization after 5 min and 10 min hydration of the tissue section. The finger-like structures in the cerebellum region of the brain are well defined for 5 min hydration. However, for 10 min hydration, these structures have poor localization. Thus, 5 min hydration provides a good balance between localization and extent of digestion.

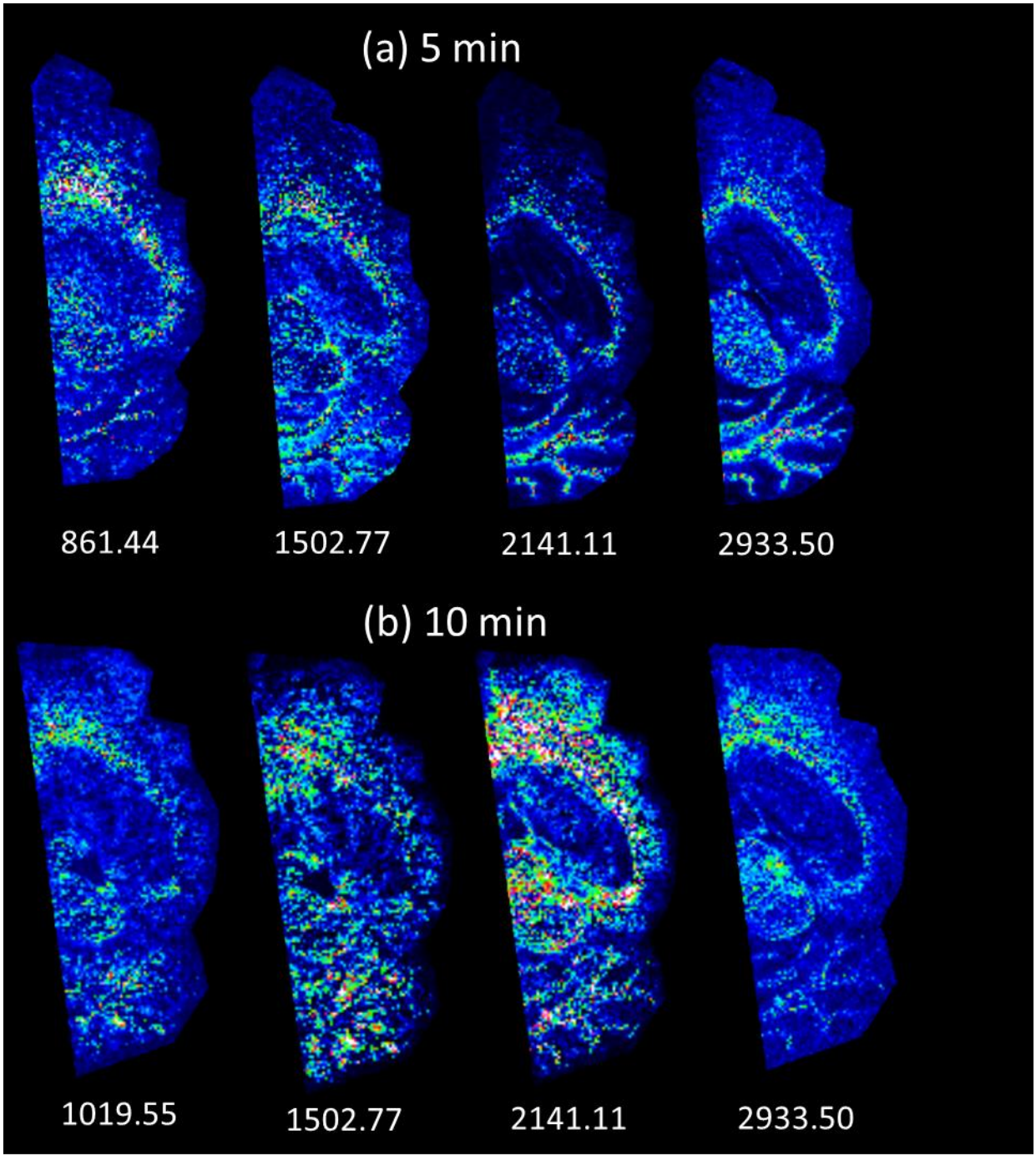

Figure 6.6. Tryptic peptides of myelin basic protein imaged directly from serial rat brain tissue sections after 5 min (a) and 10 min (b) of hydration. Hydration was conducted in a chamber saturated with DIEA and water.

6.3.5. Hydration During Incubation

In a conventional post-coated experiment, moist conditions are used within the incubation chamber. A wet paper towel is typically included to provide a source of moisture. For pre-coated slides, experiments with and without water in the incubation chamber were conducted. In one experiment, a dry incubation was used, and the temperature was maintained at 37 °C. In the second experiment, same incubation conditions were used except that 2 mL of water was spotted on a wet paper towel. The slide placed in wet incubation chamber looked visibly wet after removal from oven.

Figure 6.7 compares the average mass spectra for both cases. The spectrum corresponding to the dry incubation was dominated by lipid signals. Peptide signal was only observed when the spectrum was enlarged as shown in the inset. The spectrum corresponding to a wet incubation chamber showed significantly more peptides without any zoom indicating that the relative concentration of tryptic peptides was much higher.

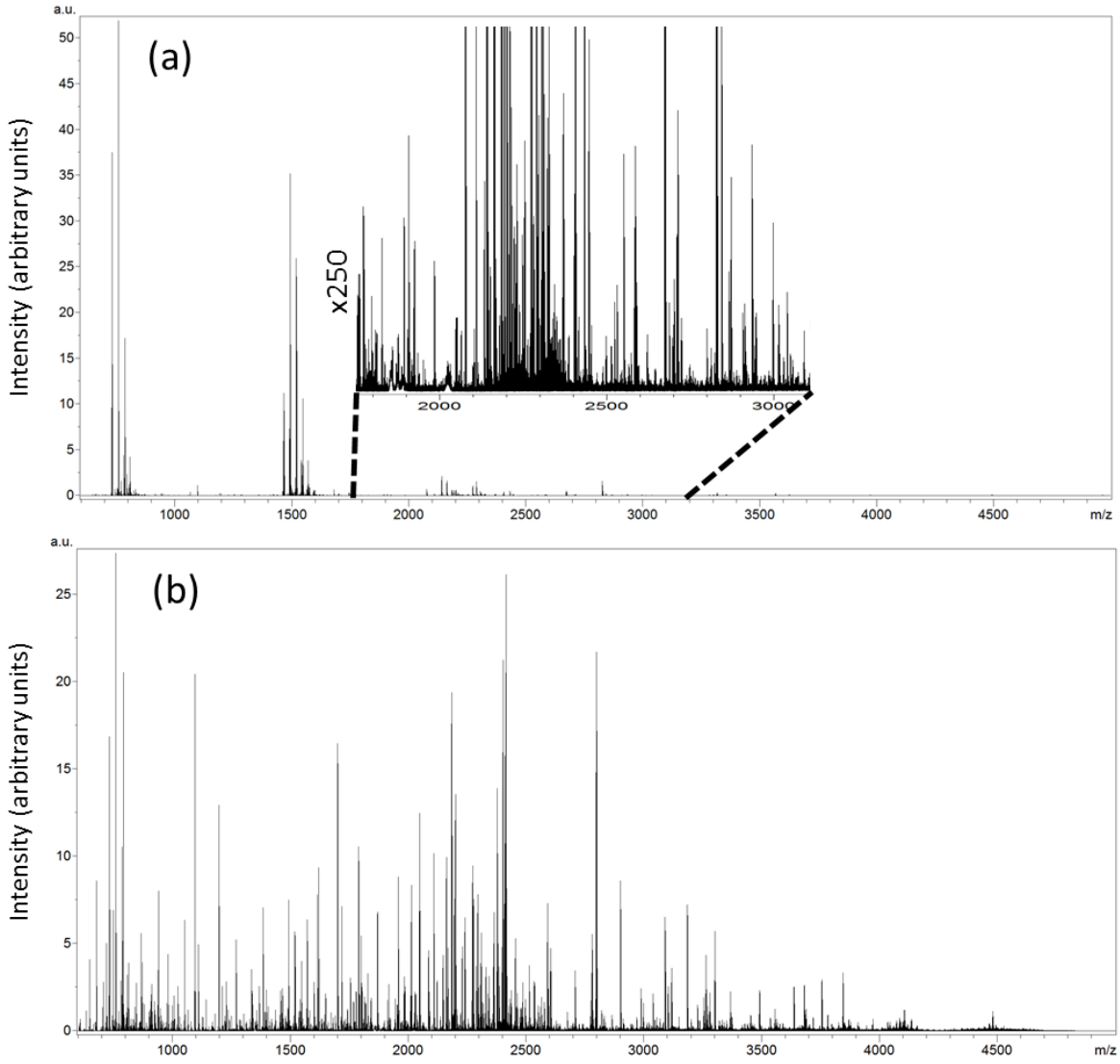

Figure 6.7. Average mass spectra acquired from serial rat brain tissues sections. (a) Digestion was conducted in a dry incubation chamber. (b) Digest was conducted in a wet incubation chamber.

Figure 6.8 compares peptide localization between the two experiments. Dry incubation showed nice localization for tryptic fragments corresponding to myelin basic protein. Ion images were also plotted for experiments with wet incubation chamber at the same m/z. Wet incubation showed no discernible localization. Thus, while wet incubation shows higher quality spectrum it causes extensive delocalization and is not recommended

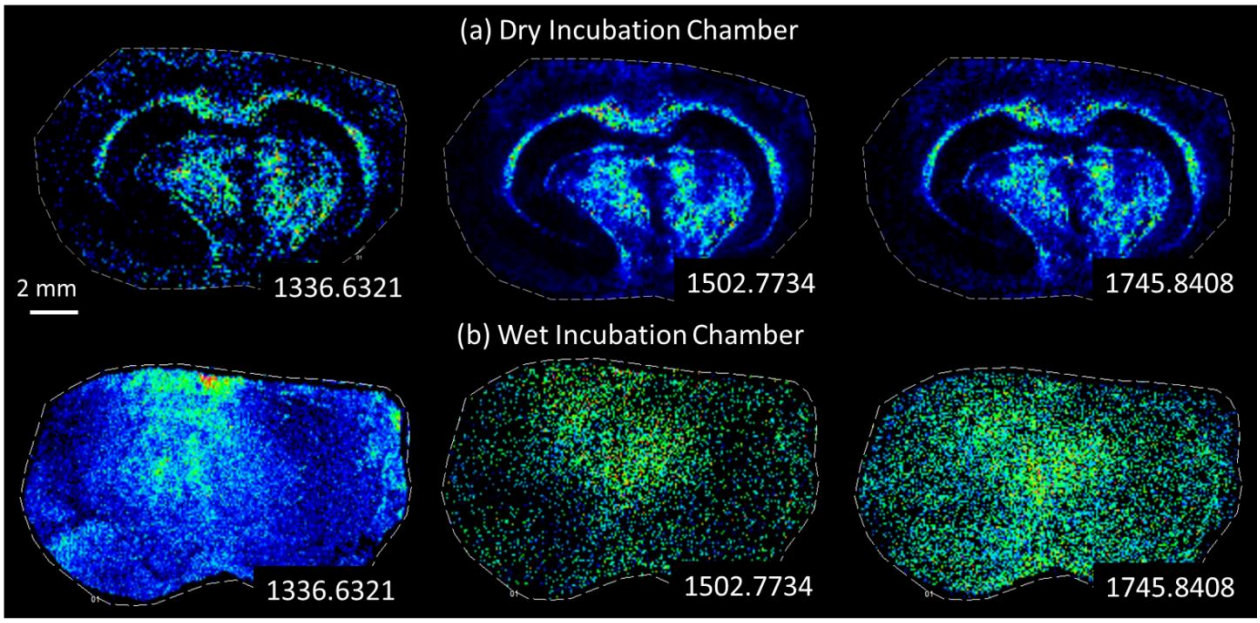

Figure 6.8. Comparison of spatial localization in experiments done in dry vs. wet incubation chamber. (a) Ion images show clear localization (b) Extensive delocalization is observed.

6.3.6. FTICR Imaging of Coronal Section of Rat Brain

Once the feasibility of the digestion in the ionic matrix was established, and the optimal trypsin and matrix densities were determined, the usefulness of these pre-coated substrates for MALDI IMS was demonstrated using rat brain tissue. The rat brain tissue section was cut at 4 μm and prepared using the procedure described in Figure 6.1. The digestion was conducted for 4 h at 37 °C. Analysis by MALDI FTICR generated hundreds of signals in 1000-5000 m/z range as shown in Figure 6.9. The mass resolution was 130,000 at m/z of 1000. Many of the detected signals were matched to tryptic fragments of the proteins found in rat brain using LC-MS/MS analysis.

Myelin basic protein, essential in the formation of central nervous system and neuronal transmission, was identified using this method.[78] The major isoform in adult rat brains has been reported to have a molecular weight of 14.2 kDa. Theoretical tryptic peptides of 14.2 kDa

isoform of myelin basic protein were generated in mMass software. Comparison of the experimental peaks in the average spectrum with the calculated masses yielded 13 matches within 1 ppm. Ion images corresponding to all of those peaks show co-localization providing further verification in the identification. Selected images are shown in Figure 6.10. These images indicate that the myelin basic protein is localized in corpus callosum and thalamus. A similar distribution was observed in the previous study.[55]

PEP-19 and neurogranin were also identified using a similar procedure of mass matching. Figure 6.11 shows that neurogranin is localized in the cerebral cortex and hippocampal region. PEP-19 is localized with high intensity in the thalamus and with reduced intensity in the cerebral cortex. These distributions are in agreement with the previous study.[79] Table 6-3 includes the data for these three proteins. The highest error observed in any of these matches was 1.3 ppm suggesting a high level of confidence in our identifications.

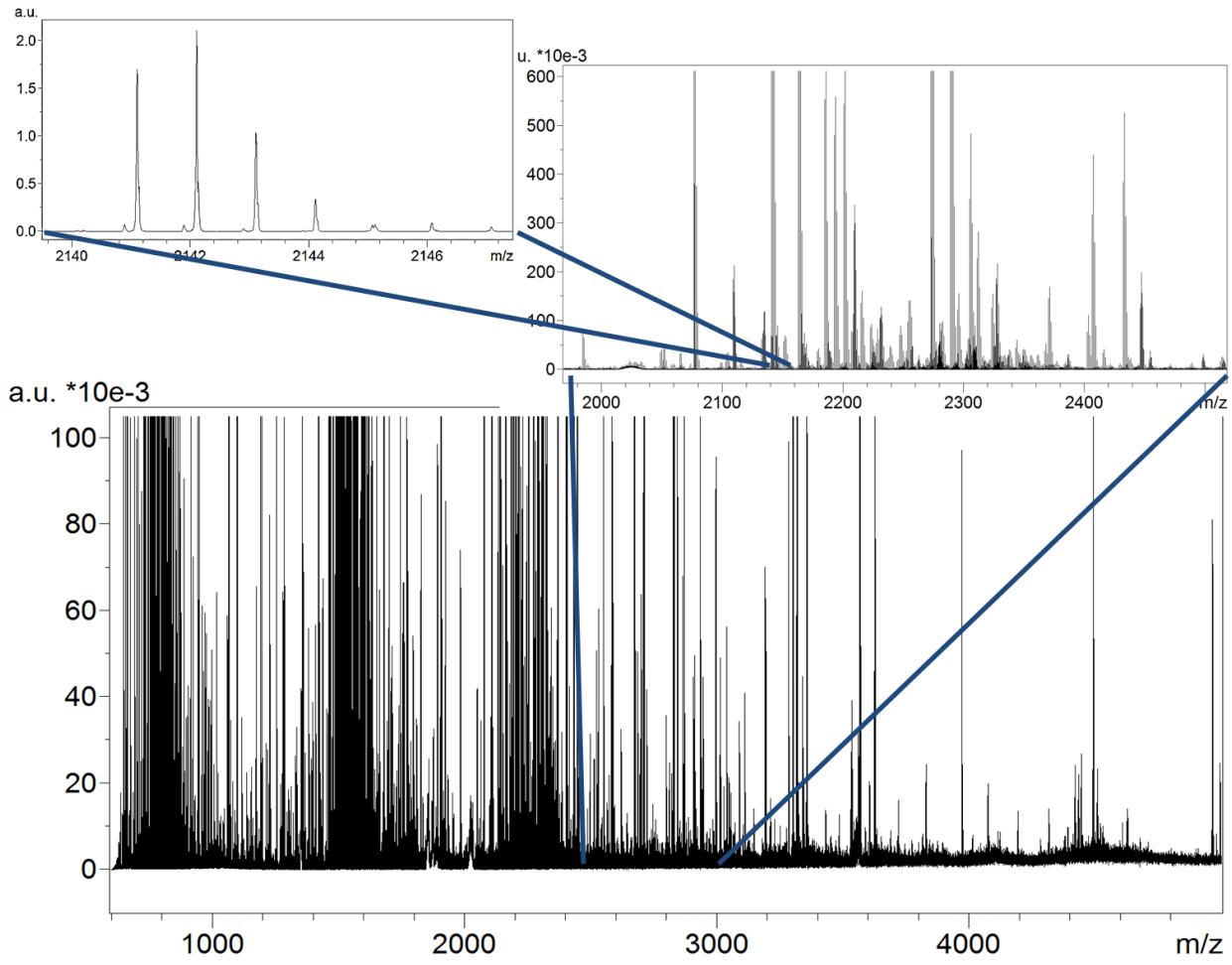

Figure 6.9. Average spectrum acquired from rat brain tissue section using the pre-coated slide. Tissue thickness was 4 µm and digestion was conducted for 4 h at 37 °C. The spectrum shows hundreds of signals are detected. The insets demonstrate the high resolution of the detected signals.

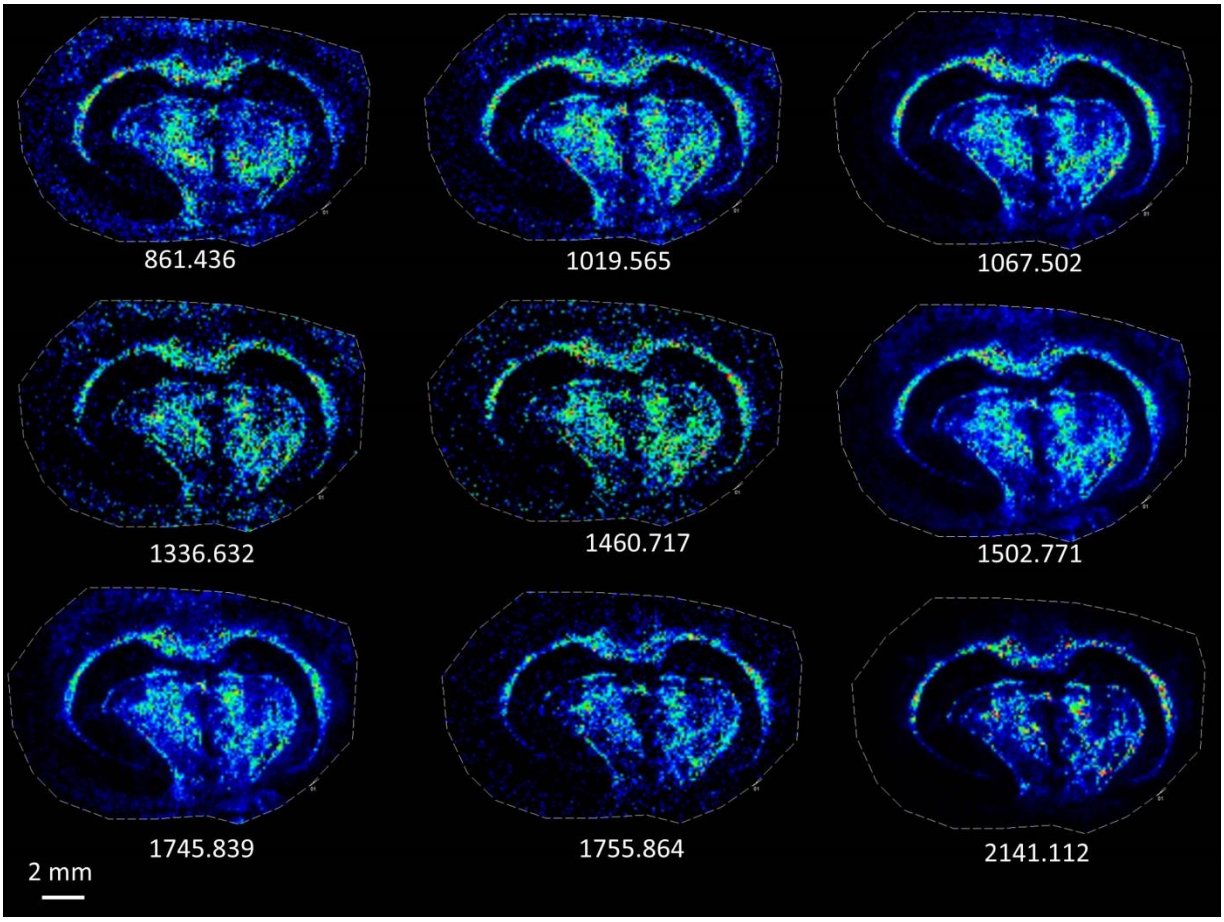

Figure 6.10. Selected ion images for tryptic fragments of 14.2 kDa isoform of myelin basic protein. Rat brain tissue section was prepared using pre-coated approach and the data were acquired using 15 T MALDI-FTICR instrument. The images were acquired at 100 μm spatial resolution. All nine signals were matched to theoretical masses within 1 ppm.

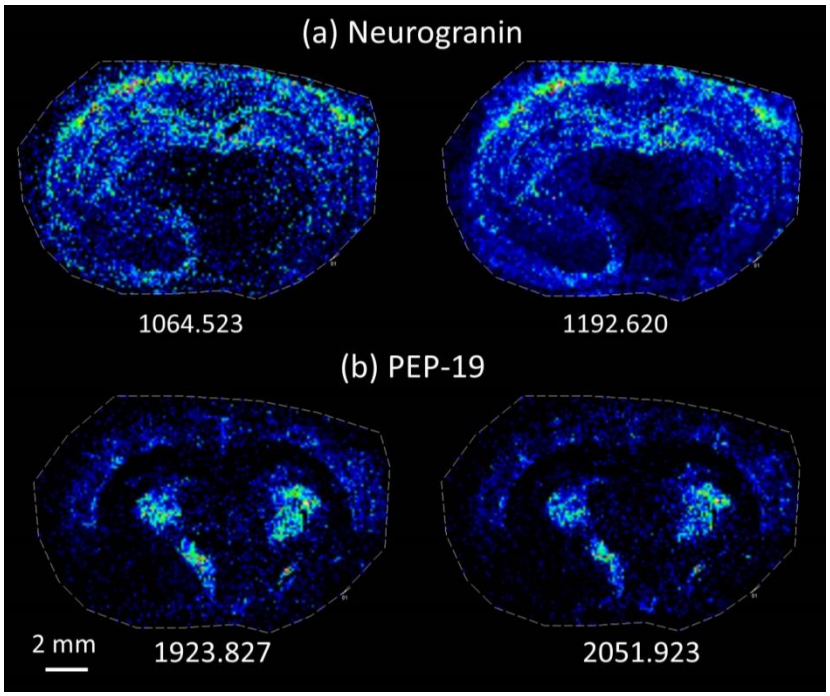

Figure 6.11. Tryptic fragments from a rat brain tissue section are displayed for (a) Neurogranin (7.5 kDa) and (b) PEP-19 (6.8 kDa). Neurogranin is localized in the cerebral cortex and hippocampal region of the brain. PEP-19 is localized in the thalamus and the cerebral cortex.

Table 6-3. List of proteins detected in a coronal rat brain section, including molecular weight of intact protein (MW), the MW for observed tryptic peptides, and the sequence determined using accurate mass matching.

Protein detected in the tissue	Tryptic peptides from In Situ Digest			
	$[M + H]^+_{exp}$	$[M + H]^+_{cal}$	ppm	Sequence
Myelin Basic Protein (14.2 kDa)				
	861.4358	861.4360	-0.2	r.SGSPMARR.
	1019.5651	1019.5646	0.5	r.HGFLPRHR.d
	1067.5023	1067.5017	0.6	r.FSWGGRDSR.s
	1336.6318	1336.6314	0.3	k.YLATASTMDHAR.h
	1460.7168	1460.7169	-0.1	r.TQDENPVVHFFK.n
	1502.7709	1502.7710	-0.1	r.TTHYGSLPQKSQR.t
	1745.8385	1745.8388	-0.1	r.HGSKYLATASTMDHAR.h
	1755.8643	1755.8660	-1.0	r.DTGILDSIGRFFSGDR.g
	2141.1123	2141.1138	-0.7	r.TQDENPVVHFFKNIVTPR.t
Neurogranin (7.5 kDa)				
	1064.5233	1064.5232	0.1	k.GPGPGGPGGAGGAR.g
	1192.6200	1192.6181	1.5	r.KGPGPGGPGGAGGAR.g
PEP-19 (6.8 kDa)				
	1923.8266	1923.8277	-0.6	k.VQEEFDIDMDAPETER.a
	2051.9231	2051.9226	0.2	k.KVQEEFDIDMDAPETER.a

6.3.7. FTICR Imaging of Horizontal Section of Rat Brain

A horizontal rat brain section was also prepared using the pre-coated approach. Figure 8 shows the obtained ion images. Image data were collected at a spatial resolution of 100 µm (pixel spacing) with ~16,000 pixels. Even at this modest resolution, substructures within the brain (white matter and molecular layer) are clearly resolved. To minimize interferences from

overlapping isotopic patterns, images were plotted by selecting only the highest intensity isotope for each peptide. All peptides corresponding to the same protein show co-localization. Myelin basic protein was localized in the corpus callosum and the white matter in the cerebellum region. Neurogranin is present in the cerebral cortex and absent from the cerebellum region. Brain acid soluble protein 1 was localized fairly uniformly in the brain except for cerebellum region. Myristoylated alanine-rich C-kinase substrate was present in high concentration in the molecular layer and in lower concentration in the cerebral cortex and the thalamus. It was absent from the white matter and the corpus callosum.

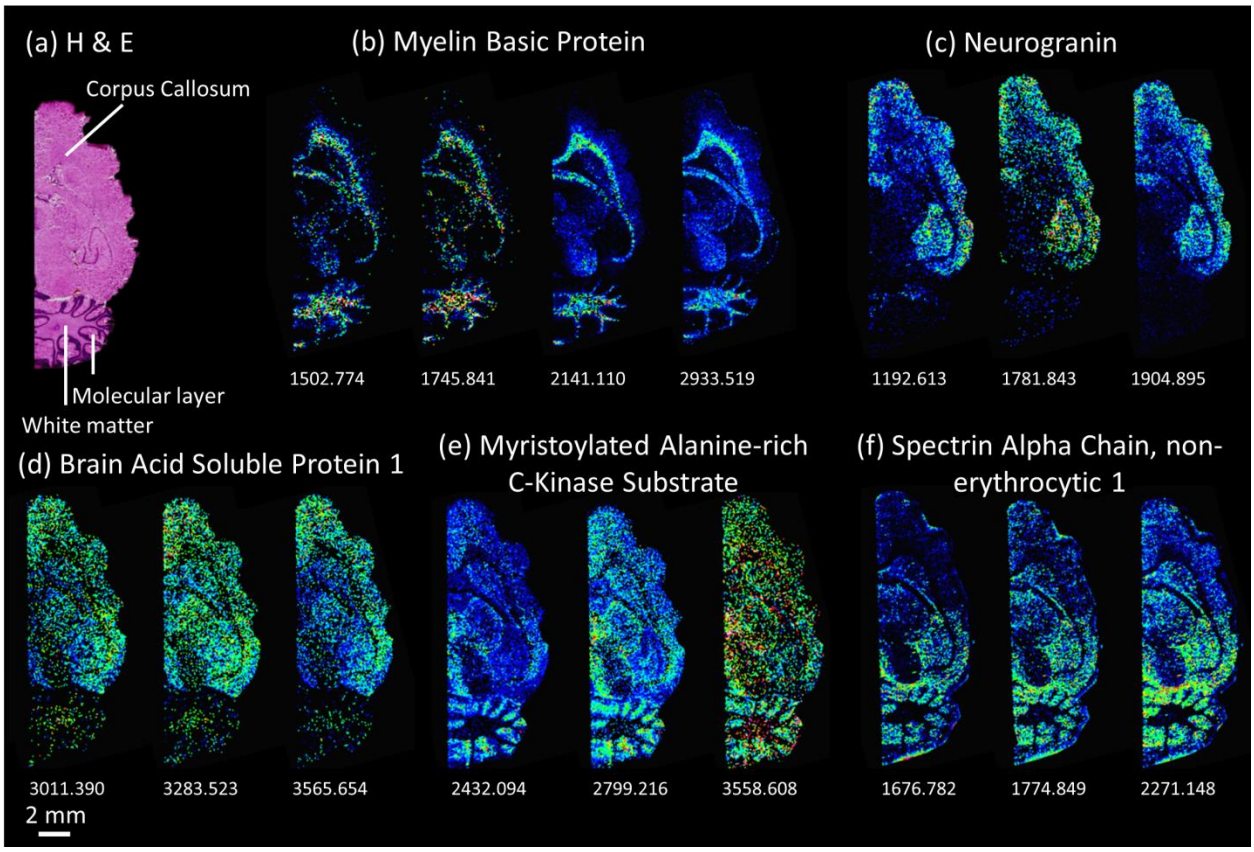

Figure 6.12. MALDI ion images of horizontal rat brain tissue section. (a) Serial section stained using hematoxylin and eosin (H&E). Peptides corresponding to (b) Myelin basic protein (c) Neurogranin (d) Brain acid soluble protein 1 (e) Myristoylated alanine-rich C-kinase substrate (f) Spectrin alpha chain, non-erythrocytic 1. Digestion was conducted at 37 °C for 15 h.

Table 6-4. List of proteins detected in a horizontal rat brain section, including molecular weight of intact protein (MW), the MW for observed tryptic peptides, and the sequence determined using accurate mass matching.

	Tryptic peptides from In Situ Digest			
Protein detected in the tissue	$[M + H]^+_{exp}$	$[M + H]^+_{cal}$	ppm	Sequence
Myelin Basic Protein (21.5 kDa)				
	1081.5472	1081.5425	4.4	r.FFSGDRGAPK.r
	1502.7742	1502.7710	2.1	r.TTHYGSLPQKSQR.t
	1745.8407	1745.8388	1.1	r.HGSKYLATASTMDHAR.h
	2141.1096	2141.1138	-2.0	r.TQDENPVVHFFKNIVTPR.t
	2933.5194	2933.5268	-2.5	r.TQDENPVVHFFKNIVTPRTPPPSQGK.g
Neurogranin (7.5 kDa)	1192.6125	1192.6181	-4.7	r.KGPGPGGPGGAGGAR.g
	1781.8427	1781.8460	-1.9	k.SGECGRKGPGPGGPGGAGGAR.g
	1904.8947	1904.8958	-0.6	r.KGPGPGGPGGAGGARGGAGGGPSGD.
Brain Acid Soluble Protein 1 (21.8 kDa)				
	2132.9216	2132.9214	0.1	k.AGEASAESTGAADGAPQEEGEAK.k
	2673.3394	2673.3366	1.1	k.APAPAAPAAEPQAEAPVASSEQSVAVKE.
	3011.3897	3011.3865	1.1	k.SEGAAEEQPEPAPAPEQEAAAPGPAAGGEAPK.a
	3283.5230	3283.5197	1.0	k.AGEASAESTGAADGAPQEEGEAKKTEAPAAGPEAK.s
	3565.6542	3565.6565	-0.6	k.AEPEKSEGAAEEQPEPAPAPEQEAAAPGPAAGGEAPK.a
Myristoylated Alanine-rich C-Kinase Substrate (29.8 kDa)				
	2432.0937	2432.0848	3.6	r.EAEAAEPEQPEQPEQPAAEEPR.a
	2799.2164	2799.2048	4.1	k.DEAAAAAGGDAAAAPGEQAGGAGAEGAEGGESR.e
	3558.6081	3558.5991	2.6	r.EAEAAEPEQPEQPEQPAAEEPRAEEPSEAVGEK.a
Spectrin Alpha Chain, Non-erythrocytic 1 (284 kDa)				
	1676.7818	1676.7762	3.3	k.HEDFEKSLSAQEEK.i
	1774.8493	1774.8541	-2.7	k.LIQNNHYAMEDVATR.r
	2271.1482	2271.1490	-0.3	k.HQKHQAFEAELHANADRIR.g

6.3.8. Imaging Lipids Using the Pre-coated Slides

In a typical post-coated preparation for protein or peptide analysis, organic washes are typically used to remove lipids.[21] After these organic washes, lipids signals in the mass spectrum are greatly reduced. Since no organic washes are utilized in the pre-coated approach, lipid signals can also be detected along with the peptides. Figure 6.13 shows selected ion images for major lipids found in rat brain. Tentative identifications based on mass accuracy are also listed. These lipids have been previously identified in our lab.

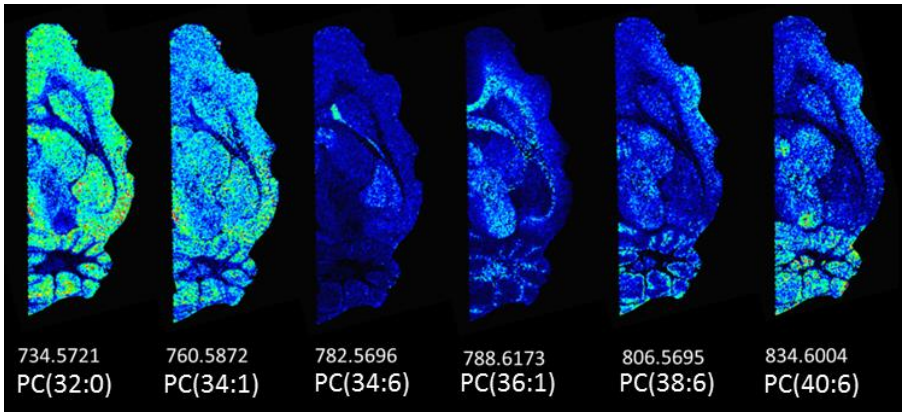

Figure 6.13. Lipid ion images acquired simultaneously using the pre-coated slides for a rat brain tissue section. Tentative identifications were based on mass accuracy.

6.3.9. Storage Conditions

Ideally, trypsin pre-coated slides would be prepared in batches and used as needed. Thus, it is important to establish the performance of trypsin pre-coated slides after storage. The slides were stored at 4 ℃ for 6 months and 18 months, and their performance was compared with a freshly prepared slide. In all three cases, standard preparation protocol was employed including 4 μm tissue thickness, 5 min hydration, incubation at 37 ℃ overnight (~16 h) and 10% TFA rinse. Figure 6.14 compares the mass spectra generated from each of the three slides using serial rat brain tissue sections. Since the data for these slides was acquired separately, the absolute ion

intensity is not directly comparable. However, relative ion intensity can be compared by examining the peptide signals between m/z 1700-4000 and the broad lipid peaks around m/z 800 and 1500. In the case of freshly prepared slides, the peptide signal was relatively strong between 1700-4000. For 6- and 18-month-old slides, the signal was dominated by lipid peaks although some peptides were seen. Thus, we conclude that the performance of the stored slides was reduced after storage.

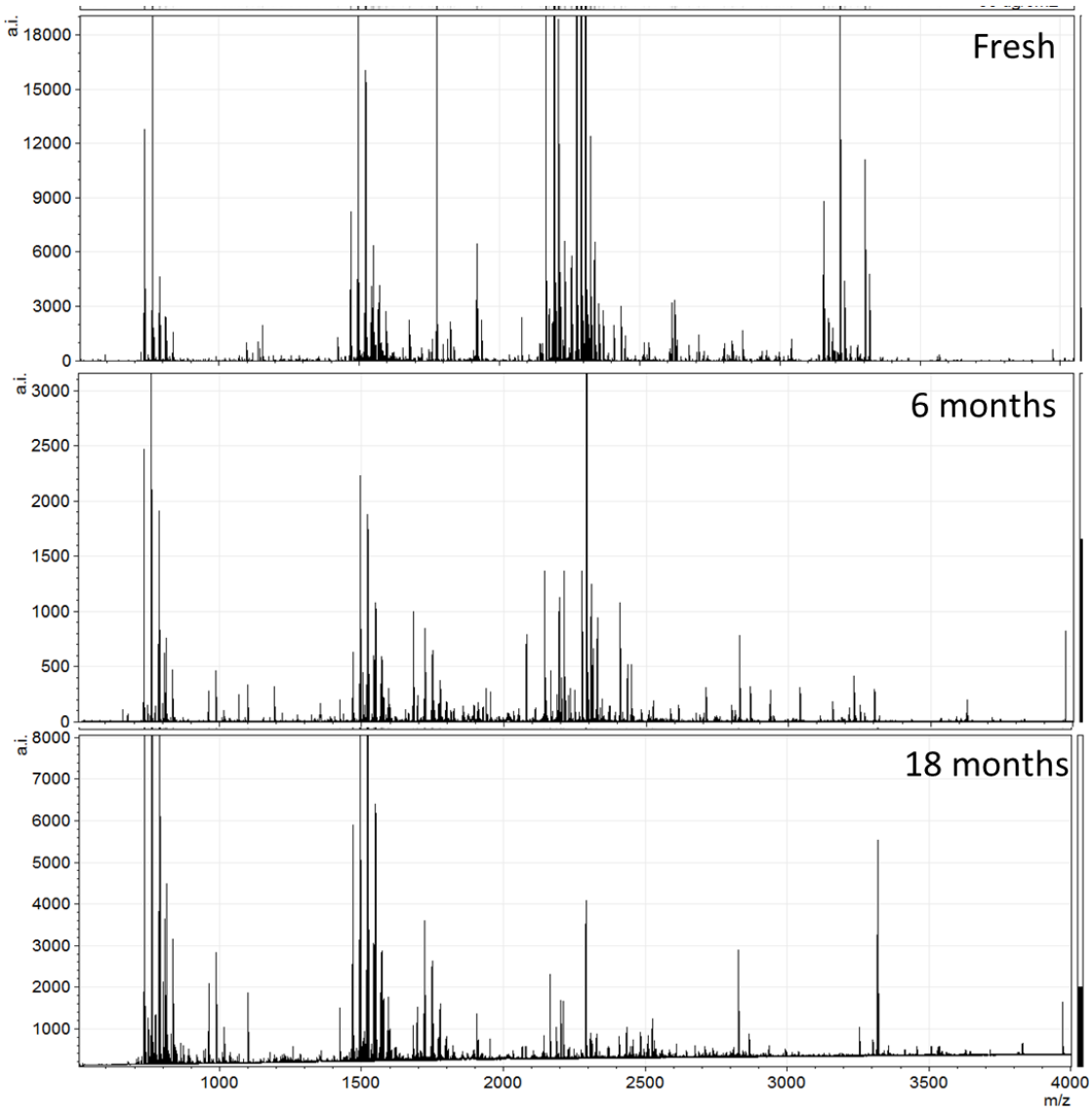

Figure 6.14. Average mass spectra acquired from serial rat brain tissue sections using a freshly prepared pre-coated slide, a 6-month-old slide, and a 8-month-old slide. Serial rat brain tissue sections were mounted on the pre-coated slides and incubated overnight at 37 °C. The relative amount of lipid and peptide signal are compared to evaluate the overall performance. Lipid signals are located at m/z 600-750 and 1450-1600. Peptide signals appear between m/z 1600 – 4000, although some peptides signals are interspersed with the lipid signals. The relative amount of peptide signal is highest in the freshly prepared slides and is lower in the 6- and 18-month-old slides.

Figure 6.15 compares the ion images obtained from the three slides. Most abundant tryptic fragments of myelin basic protein from each experiment are chosen. Freshly prepared slides performed the best with crisp ion images and clear spatial localization, especially in the cerebellum region. For 6- and 18-month-old slides, the quality of the ion images deteriorated in two aspects. First, the ion images were noisier for older slides. Secondly, the finger-like structures in the cerebellum region were poorly defined.

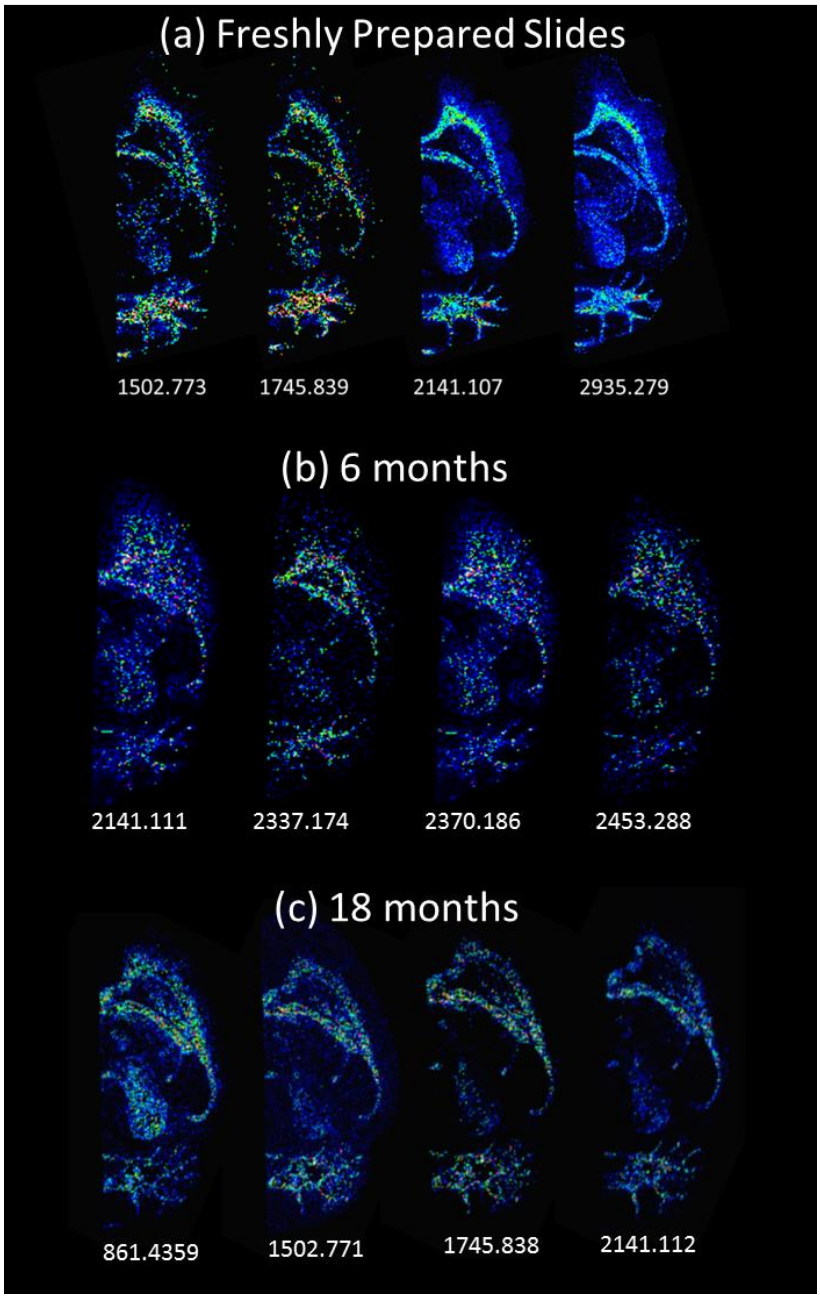

Figure 6.15. Ion images of myelin basic protein acquired using a freshly prepared pre-coated slide are compared with those obtained using slides stored for 6 months and 18 months. Serial rat brain tissue sections were mounted onto the pre-coated slides and incubated overnight at 37 °C. Ion images corresponding to tryptic fragments of myelin basic protein are shown here. Freshly prepared slides show higher quality images and the finger-like structures in the cerebellum regions are fully resolved. Older slides show noisier images and finger-like structures are poorly resolved.

Table 6-5 compares the signal-to-noise (S/N) ratio for the three data sets of tryptic fragments of myelin basic protein. We find that the S/N ratio was between 200 and 700 for a freshly prepared slide. For a 6-month slides, the S/N ratio is below 100 except for the m/z of 2141.109. For a 18-month-slide, the S/N ratio was even lower ranging between 10 – 70.

Table 6-5. Comparison of signal-to-noise ratio for three sets of slides

Myelin Basic Protein							
m/z	S/N, Fresh		m/z	S/N, 6 months		m/z	S/N,18 months
1081.548	280.3		1019.567	31.9		861.436	61.2
1502.771	589.4		1336.625	34.3		1013.590	13.3
1745.839	249.2		2141.109	575.0		1502.771	33.8
2141.112	703.9		2370.187	79.4		1745.839	15.6
2933.516	205.8		2453.229	19.6		2141.112	25.9

6.3.10. Development of Microarrays to Minimize Analyte Delocalization

As discussed in section 6.3.4., hydration of the tissue can induce analyte delocalization causing a loss in spatial information of biomolecules. Matrix microarrays have been fabricated using the lithographic procedures described in Chapter 3 to minimize delocalization of analytes. Figure 6.16 illustrates the employed workflow using arrayed targets. Trypsin was manually sprayed onto the matrix array, and thin tissue sections (3- 5 μm) were thaw-mounted on this slide. After the tissue was mounted, the slide was placed in a chamber saturated with DIEA and water for 2 min. The acidic matrix absorbed the amine forming an ionic matrix. After digestion for 2 h at 37 °C, the slide is rinsed with 2% TFA to remove the DIEA and recast the matrix as crystals.

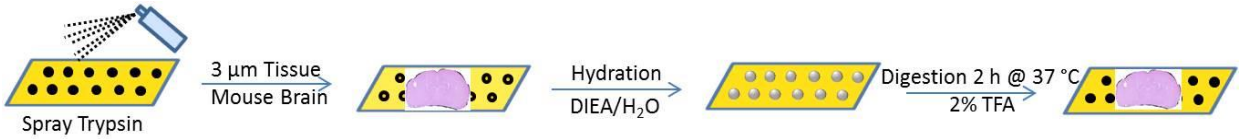

Figure 6.16. Workflow for on-tissue digestion and peptide imaging.

After the rinsing step, the sample was ready to be analyzed using mass spectrometry. Using this approach, we imaged the coronal section of the rat brain using a Bruker Daltonics Autoflex Speed MALDI-TOF. Fig 6.17 shows the obtained imaging results. Ion images corresponding m/z of 789.0 and 793.7 show high intensity in the corpus callosum region whereas ion images corresponding m/z of 862 and 1857 show localization in the thalamus.

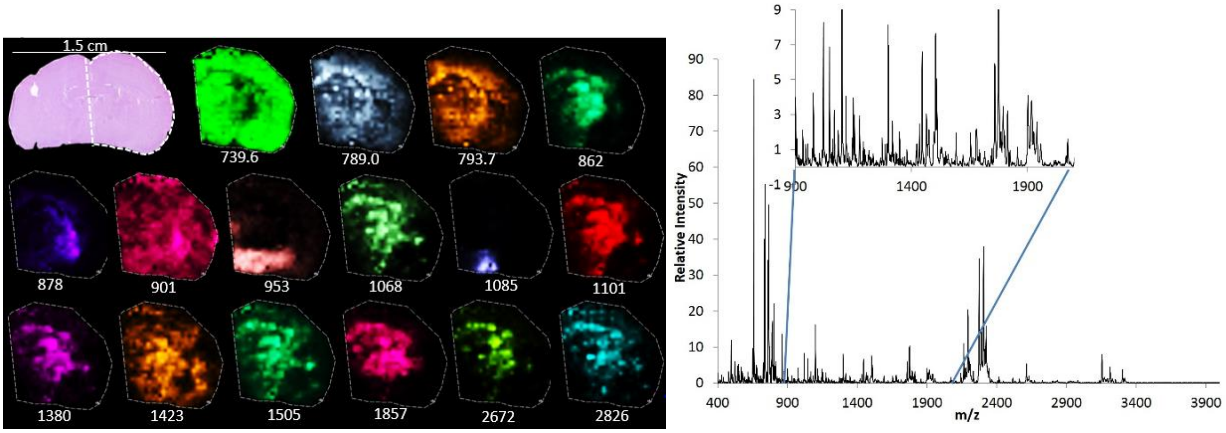

Figure 6.17. Peptide imaging of a coronal section of rat brain using a pre-coated array containing both matrix and trypsin. The right half of the tissue section was imaged. The average spectrum is shown on the right.

The results in Figure 6.17 are a promising start towards the development of and application of microarray slides, but a direct comparison with homogeneous targets is yet to be done. Additionally, microarray technology requires alignment of the laser with the matrix spots. Figure 6.18 illustrates this problem. The middle figure shows the optical image of the target after laser interrogation. The top zoomed-in inset indicates that the laser ablation crater is aligned with the matrix spot generating an optimal signal. However, the lower inset indicates that laser

ablation was at the edge of matrix spot generating a non-optimal signal. At 100 µm pitch distance, rotational and translational alignment of the laser with matrix spots becomes challenging. Presently, the FlexImaging software only allows for step size adjustment in increments of 1 µm and does not allow for rotational adjustment which is dictated by teaching points. Thus, for this approach to work modifications need to be made to the software acquisition system

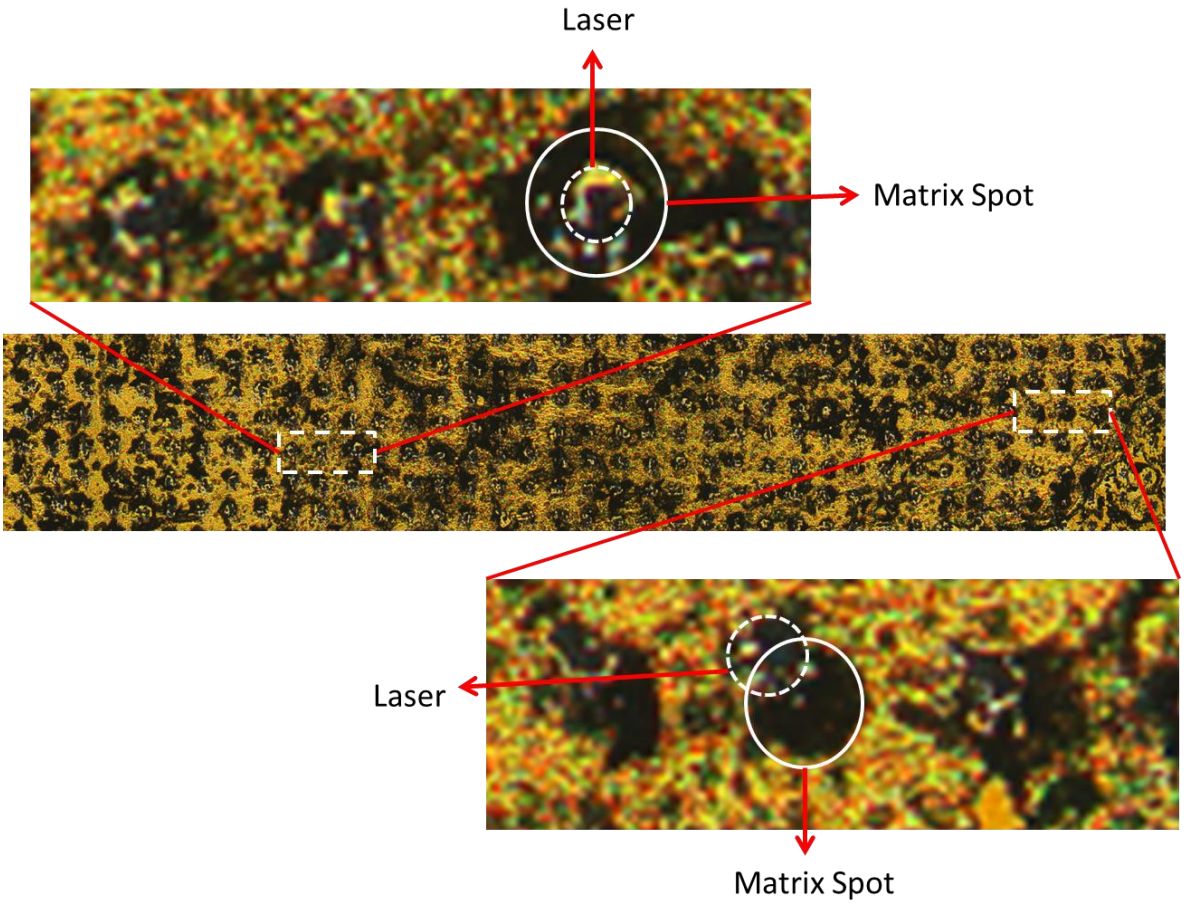

Figure 6.18. The challenge of aligning laser with matrix array. The middle figure shows the optimal image of the arrayed target after MALDI analysis. The laser ablation craters are superimposed on top of the matrix spots. The top inset indicates that the laser spot is aligned with the matrix spot in certain locations. The bottom inset indicates that in certain locations ablation craters and matrix spots are misaligned.

6.4. Conclusions

Matrix and trypsin pre-coated slides provide a simple approach to image proteins and lipids within biological tissues. The pre-coated method reduces the burden of sample preparation from the end user and allows faster sample preparation. The pre-coated slides could be stored in a freezer and can be used to prepare multiple tissue samples at the same time. The tissues are simply mounted on the pre-coated substrate, hydrated and then incubated in the oven.

The molecular information can be identified by linking MALDI imaging data to LC-MS/MS using accurate mass. The co-localization of peptides coming from the same parent protein provides additional verification in the identification. Some large proteins were identified using MALDI-IMS including myristoylated alanine-rich C-kinase substrate (29.8 kDa) and spectrin alpha chain, non-erythrocytic 1 (284 kDa).

One challenge to the pre-coated methodology is that the tissue section cannot be washed after mounting onto the pre-coated slides as that might dissolve the trypsin and matrix coating. Thus, peptide sensitivity is reduced due to the presence of lipids. The advantage here is that lipids can also be imaged in addition to peptides on the same tissue section. Future approaches may investigate washing lipids from the tissue immediately after extraction from the animal and before freezing.

CHAPTER 7. CONCLUSIONS AND PERSPECTIVES

7.1. Development of Standard Reticle Slide

The first major accomplishment of this work was the development of a standard reticle pattern for quantifying spatial resolution in MALDI-IMS. Lithographic techniques were used to fabricate stamps with features ranging between 25 and 200 μm in size. High-throughput patterning methods were developed to shape hydrophobic and polar dyes into a specified pattern. A single SU-8 master was used to produce tens of PDMS stamps, and each stamp was used more than 20 times for functionalizing gold surfaces making this process inexpensive. Self-assembly process to form the crystal violet pattern is rapid; the process of contact printing and self-assembly was completed in less than 5 min.

In addition to a MALDI-compatible pattern, computational models were developed for quantifying beam size and spatial resolution of the ion images. Image functions were derived for model beams and boundary conditions from the pattern were applied to determine the expected image. Subsequently, the determined image function was fit to the experimental data to determine beam sizes along with their corresponding uncertainties. For a Gaussian beam, the accuracy of FWHM measurement was better than 2 μm provided sufficient laser energy was used to give an acceptable signal. The accuracy of the measurement was largely dependent on the step size; a smallest possible step size of 5 μm was implemented. For measurements of FWHM for smaller beams (FWHM < 5 μm) and for higher precision in measurement, steps sizes will need to be reduced proportionally.

The overall spatial resolution of the imaging instrument under the operating conditions was quantified using a line grating of crystal violet. Several scan lines were acquired across the crystal violet lines, and their ion intensities were added together. A resolution threshold was specified at 10% of ion signal; in other words, a gap size between adjacent crystal violet lines is said to be resolved when the MS signal in the 'empty' region dips below 10% of the maximum signal. The advantage of the line grating method is that it can be applied to irregular beam profiles whereas the measurement of spot sizes is presently limited to model beam profiles.

7.2. Next Generation of the Reticle

The current version of the reticle is limited to measuring spatial resolution down to 30 μm. Next generation of the reticle will require sub-micron features to quantify resolution in the state of the art MS instruments. Working towards this goal fabrication tools within the VINSE clean room were used to fabricate features below 10 μm. The new version of the reticle is designed to have features ranging from 1 μm to 100 μm divided into 3 segments: 1 – 10 μm, 10 – 50 μm, and 50 – 100 μm. The 50 – 100 μm regions consisted of features in 5 μm increments, and each feature had five replicates to enable confident identification (see Figure 7.1). The second region from 10 to 50 μm also consisted of 5 lines for each dimension but the increments were 2 μm. Thus, within this range, the accuracy will be +/- 2 μm. The third region contained features from 1 to 10 μm in increments of 1 μm.

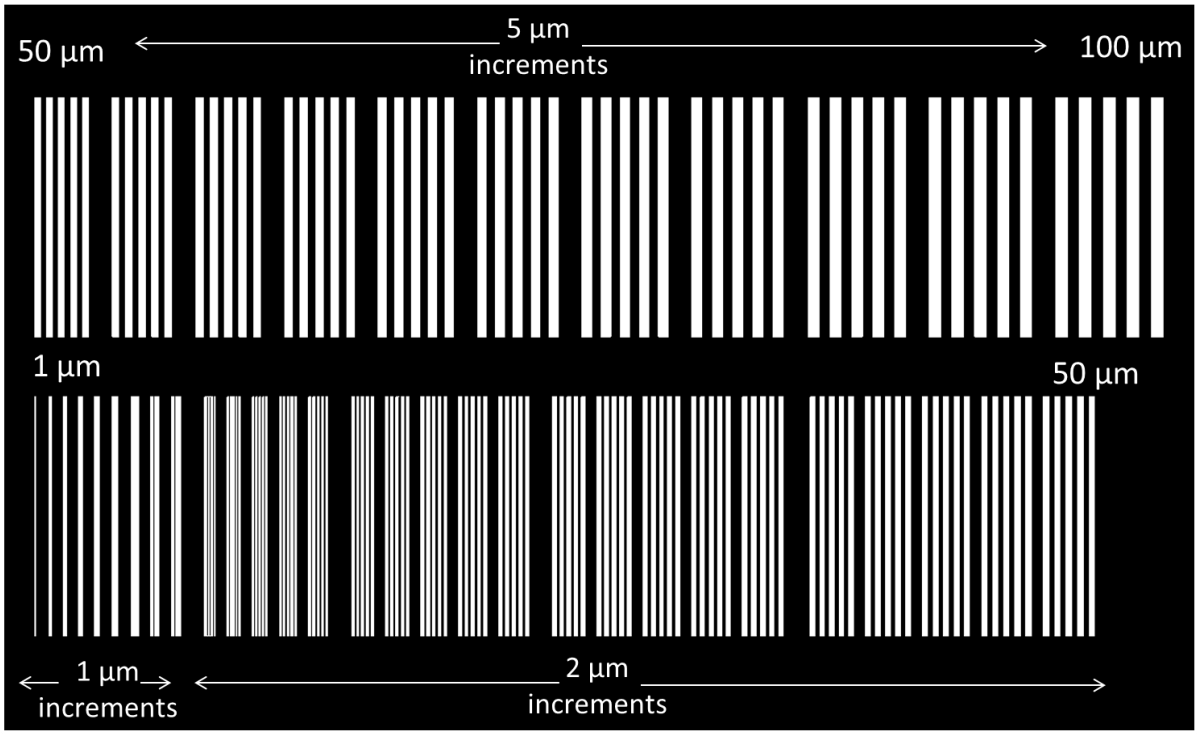

Figure 7.1. Photomask design for the next generation of the reticle contains three regions for testing: 1-10 µm, 10-50 µm, and 50-100 µm. The 1-10 µm region contains features in 1 µm increments, the 10-50 µm region contains features in 2 µm increments, and the 50-100 µm region contains features in 5 µm increments. For each feature, five replicates are included to enable confident measurement of spatial resolution. In the figure, features smaller than 20 µm are not apparent. White areas in the photomask represent transparent regions that allow UV light transmission through the photoresist.

The photomask design was printed onto a chrome-coated substrate as shown in Figure 7.2. Heidelberg laser writer (µPG 101) with a 405 nm diode laser was used to irradiate the photoresist, and the pattern was developed in MF319 solution to remove the exposed photoresist. The substrate was then inserted in etchant 9030 for 1 min to remove the exposed chrome. Finally, oxygen plasma was used to remove the remaining photoresist.

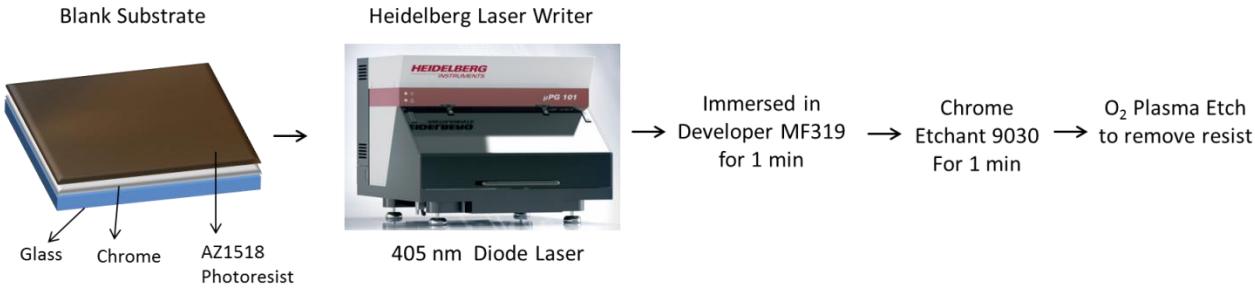

Figure 7.2. Process for designing the chrome mask. A glass substrate is coated with chrome, and a AZ1518 photoresist layer is patterned using a Heidelberg Laser Writer. The exposed photoresist is developed in MF319 solution. Etchant 9030 is used to remove the exposed chrome followed by an O_2 plasma to remove remaining photoresist.

The fabricated photomask is shown in Figure 7.3. Figure 7.3a shows the 1" x 1" region on the photomask that was patterned. Figure 7.3b-c shows the 1 μm features were barely resolved on the photomask whereas 2 μm features were clearly resolved. In both cases, the line width was enlarged.

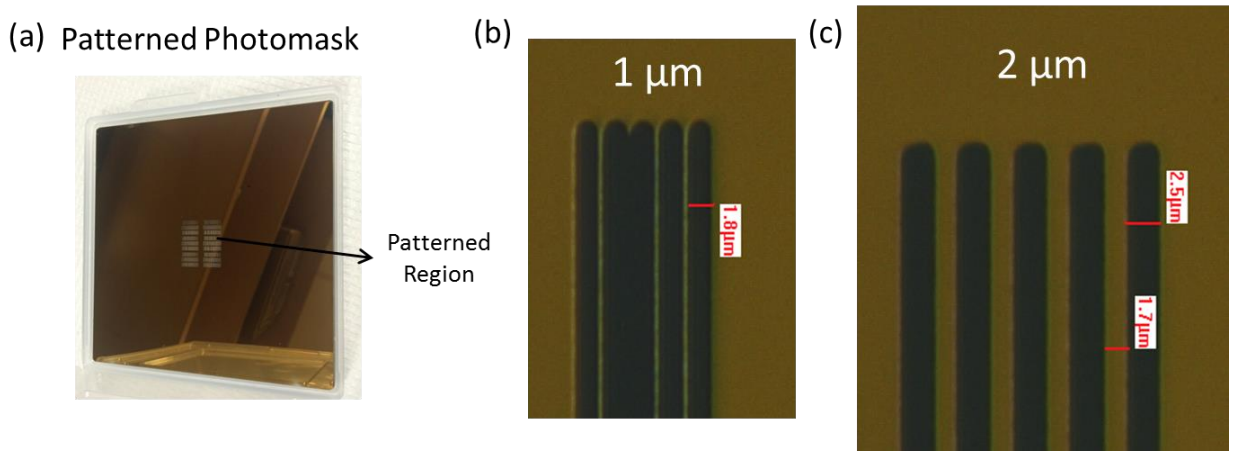

Figure 7.3. Photomask fabricated using a Heidelberg laser writer. (a) The substrate measured 5" x 5" and a small region is used for printing (1" x 1") (b) An expected 1 μm line width was enlarged to 1.8 μm, and two of the lines coalesced together. (c) Expected 2 μm lines were enlarged to about 2.4 μm. The tan color corresponds to non-transparent chrome layer, and the darker color is due to a black background.

Photolithography process was implemented using the new mask with features down to 2 µm in size (see Figure 7.4a). As the UV light is transmitted through the mask it diffracts producing features that are larger than intended sizes. As shown in Figure 7.4d, the broadening of the feature can cause individual lines to merge together. The angle of diffraction is directly dependent on the size of the aperture and the extent of line broadening can be calculated by the product of the diffraction angle and the thickness of the photoresist using the small angle approximation. The employed photoresist (SU-8 3025) was 25 µm thick when spin-coated onto the substrate. Using this photoresist, distinct features down to 8 µm can be produced as shown in Figure 7.4. To enable fabrication of smaller features, a photoresist with lower viscosity should be employed to generate thinner coating. For example, SU-8 3005 will lead to coatings that are 5 µm in thickness so that the process can be scaled down to 2 µm features.

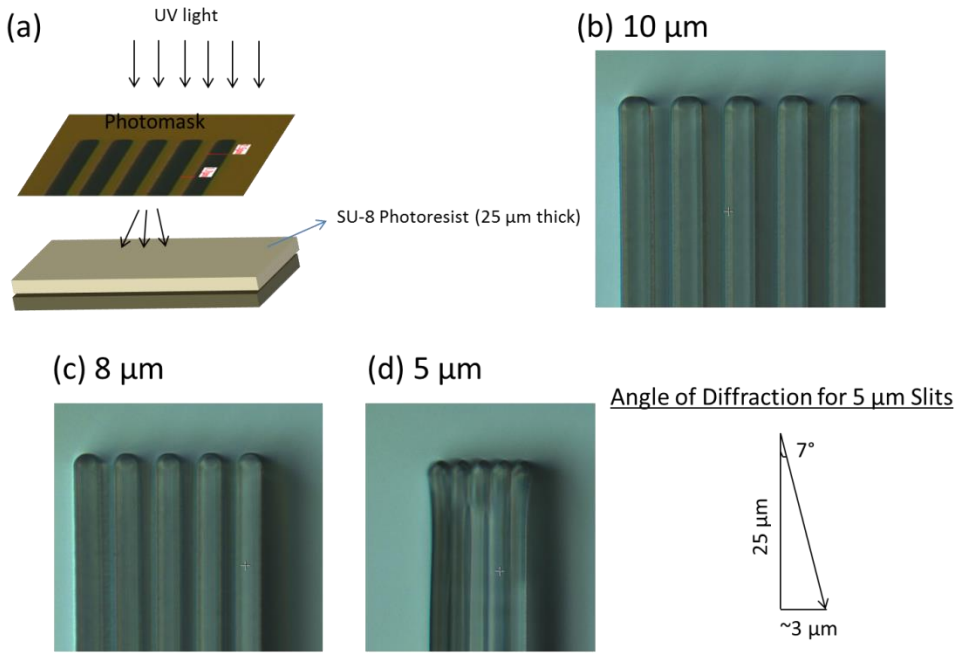

Figure 7.4. Fabrication of the next generation of the reticle. (a) Photolithography process that exposes the photoresist through a photomask. (b) Generated 10 µm features.

Figure 7.5 demonstrates the image of crystal violet pattern produced using the developed stamp. Line with widths of 9 µm or smaller coalesced together suggesting that the gap between the lines was insufficient to ensure distinct features. The density of crystal violet shows gradient corresponding to the size of the features. As the feature size increases, the thickness of crystal violet increases. Due to these reasons adhesive/ diffusive printing is recommended for dimensions below 10 µm.

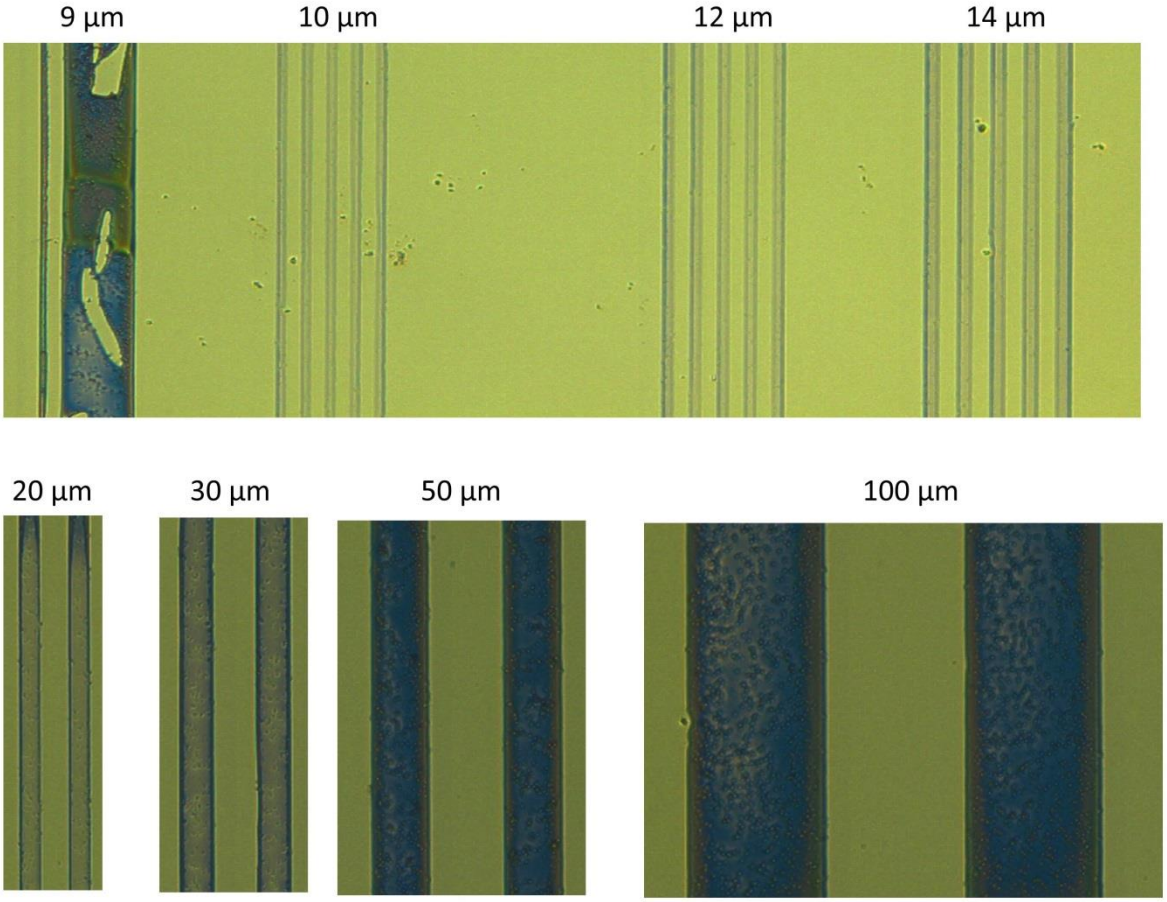

Figure 7.5. Crystal violet lines produced using the next generation stamp. Lines with widths of 9 µm or smaller coalesce together suggesting that the gap between the lines was insufficient. 10 µm lines were isolated. The thickness of the lines increases as the width of the line increases.

Three major improvements were made in this new version of the reticle. First, the smallest feature on this version was 10 μm in size compared to 25 μm in the previous version. Secondly, 5 replicates were included for each dimension enabling a higher degree of confidence in our measurements whereas previously only two or three replicates existed. Thirdly, finer increments were employed in this version allowing for a higher precision in the measurement of resolution. The fabrication process has to be tailored to the size range of the features precluding the possibility of including the full range of features sizes on a single reticle slide. The fabrication process has to be separately optimized for three set of ranges: 100 nm – 1 μm, 1 - 10 μm, 10 - 200 μm.

7.3. Development of the Pre-coated Slides

The second major accomplishment of this work was the fabrication of trypsin pre-coated substrates for high-throughput proteomic analysis. Trypsin and matrix were spray-coated onto ITO-coated slides, and a tissue was thaw-mounted onto these pre-coated slides. The peptides can be digested, imaged and identified based on mass accuracy. These targets streamline the process for preparing tissue samples, minimize the burden of sample preparation on the end user and improve spatial resolution from 200 μm to 75 μm.

One of the challenges with the pre-coated slides is that the tissue cannot be solvent-washed to remove unwanted species once it is placed onto the pre-coated slide. As a result, lipids and lipid dimers were dominant in the obtained mass spectra. A couple of approaches are suggested to address this issue. First, whole organs could be immersed in ethanol solution immediately after extraction from the animal to remove lipids prior to freezing the sample. A second approach would involve chemically linking the trypsin to the surface making it resistant

to solvent washes. Ma et al. have suggested the fabrication scheme for such a surface.[80] Tetraethoxysilane and 3-amino-propyltriethoxysilane were reacted together to form a monolith network. Glutaraldehyde was used to couple the monolith support with trypsin. The immobilized trypsin had significantly higher activity relative to trypsin in-solution. These surfaces can be adapted for the pre-coated approach whereby tissue section is mounted onto these immobilized surfaces, and the slide is solvent washed to remove lipids and salts, incubated to digest proteins, and coated with matrix.

The second major challenge was the inability to store pre-coated slides at 4 °C due to reduced performance after storage for 6 to 18 months. The storage ability needs to be investigated in more detail by using an assay to measure the trypsin activity on the pre-coated surface. Standard substrates such as p-nitroaniline or nα-benzoyl-DL-arginine 4-nitroanilide hydrochloride could be used to measure trypsin activity after it is deposited on the surface.[81]

7.4. Application of Pre-coated Slides to Formalin-fixed Paraffin-Embedded Tissues

Formalin-fixed paraffin embedded (FFPE) tissues are tremendously important in the clinical environment given the vast repositories of such samples in tissue banks with associated pathological, clinical, and patient outcome information.[56, 64, 82] Multiple groups have developed methods imaging FFPE tissues by IMS that involve laborious antigen retrieval and on-tissue digestion methods. [58, 64, 71, 83] The application of enzyme and matrix pre-coated slides will be particularly useful for FFPE tissues.

In a proof-of-principle experiment, the ability of the ionic matrix to enable digestion of FFPE tissues was tested. The FFPE rat brain tissue underwent typical processing conditions

including sectioning, mounting on an ITO-coated glass substrate, paraffin removal, and antigen retrieval. After these processing steps trypsin in ionic matrix was spotted on top of the tissue to digest the proteins. A serial tissue section was prepared using the conventional approach using trypsin in ammonium buffer solution. Figure 7.6 below compares the mass spectral results. Several peaks were observed in both cases showing efficient digestion. Ionic matrix preparation provided richer spectra with more peaks and higher intensities.

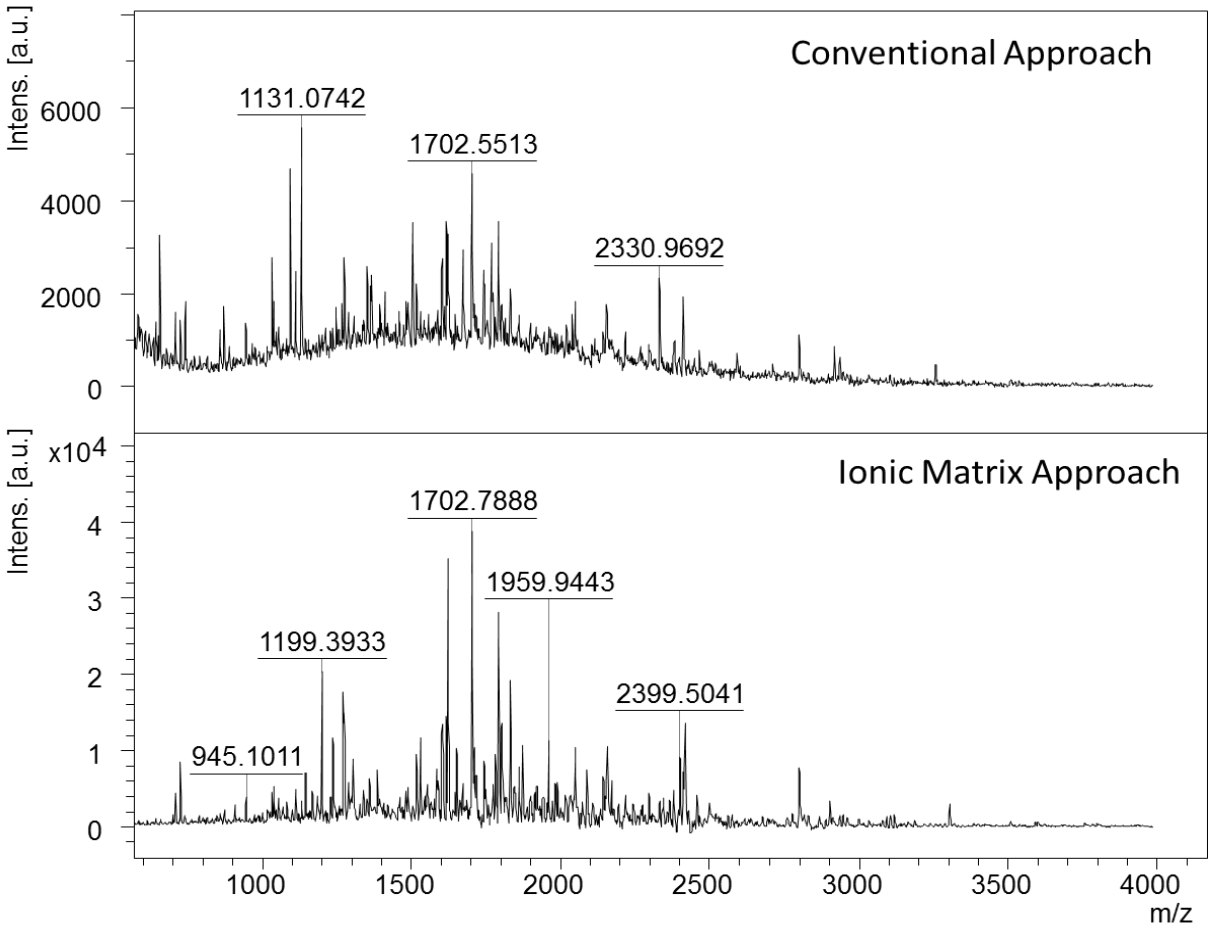

Figure 7.6. Digestion of FFPE rat brain tissue by hand-spotting trypsin in the ionic matrix and trypsin in 100 mM ammonium bicarbonate buffer solution on serial tissue sections. The trypsin concentration was the same in both cases, and the same region of the tissue was used.

An additional advantage of the ionic matrix preparation is that smaller spot sizes were obtained due to a higher surface tension and a single step deposition. Figure 7.7 shows the spot sizes as measured after robotic deposition. The average spot diameter for a preparation involving buffer solution was 210 µm compared to 164 µm using ionic matrix approach. This reduction in spot size will be especially beneficial for histology directed analysis where the area of analysis is directly limited by the spot size.

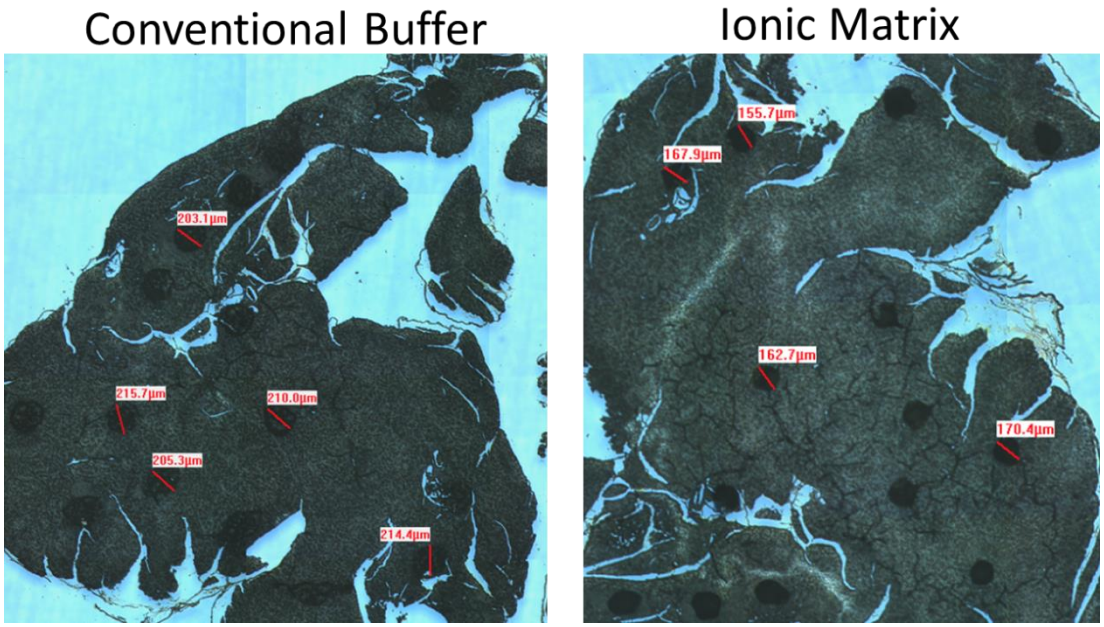

Figure 7.7. Comparison of spot sizes using conventional buffer approach and ionic matrix approach.

Lastly, the applicability of pre-coated slides towards analysis of FFPE tissues was evaluated for an imaging experiment. Sagittal mouse brain tissue sections were prepared using conventional robotic spotting methods and the pre-coated methods. Figure 7.8 compares the representative mass spectra obtained from these two experiments. Pre-coated slides showed better signal-to-noise ratio suggesting improved digestion although these peaks need to be identified to make conclusive statements.

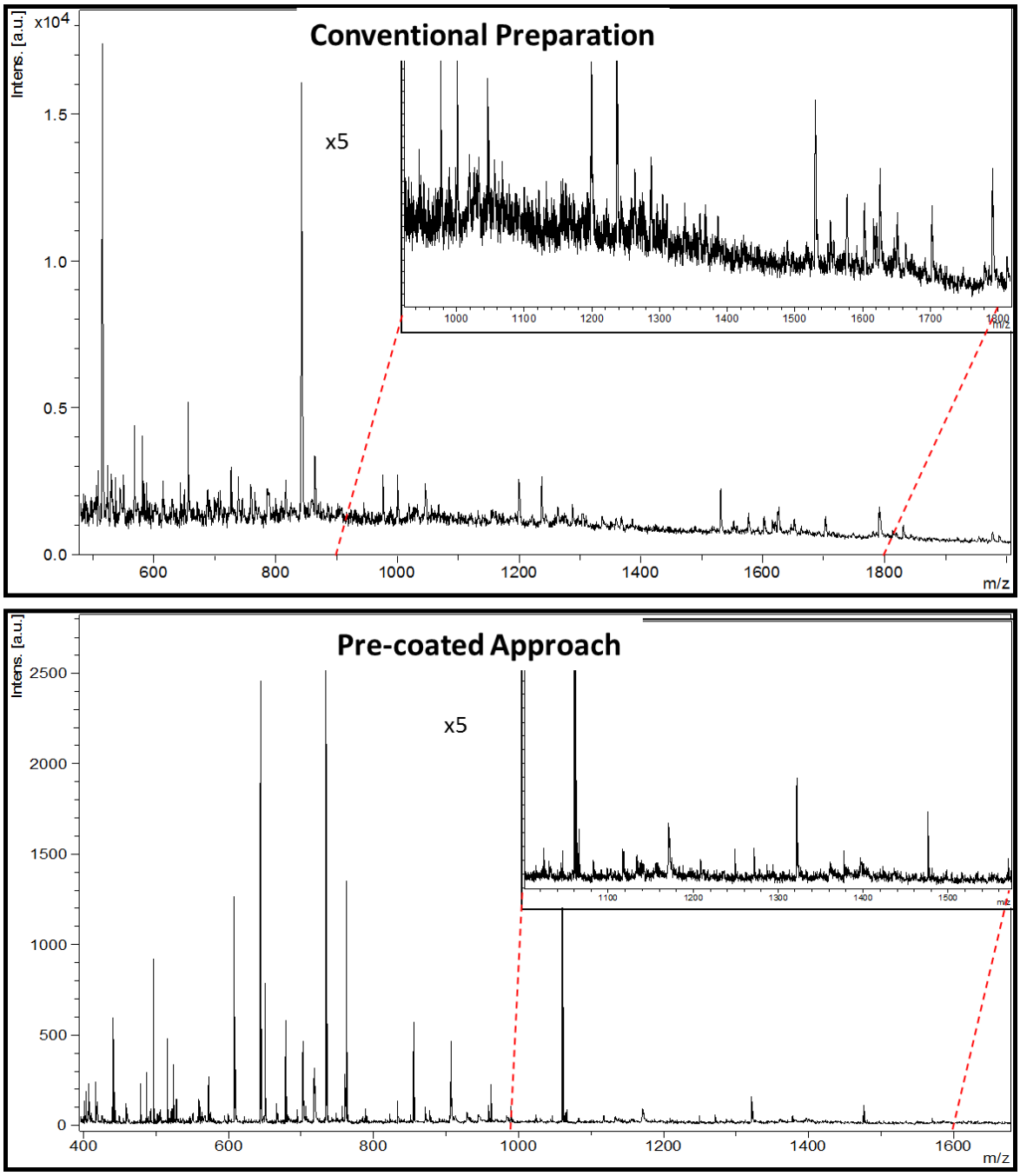

Figure 7.8. Digestion of FFPE rat brain tissue using conventional approach employing a robotic spotter and the pre-coated approach. Presented representative spectra were obtained using MALDI-TOF/TOF.

Figure 7.9 compares the ion images acquired using the conventional methods and the pre-coated approach. Due to different extraction medium, a different selection of ions was observed in each case. A step size of 300 µm was used in the case of conventional preparation. For the pre-coated approach, a step size of 100 µm was used allowing observation finer biological detail. These experiments show the promise of pre-coated slides in preparing clinically significant FFPE samples.

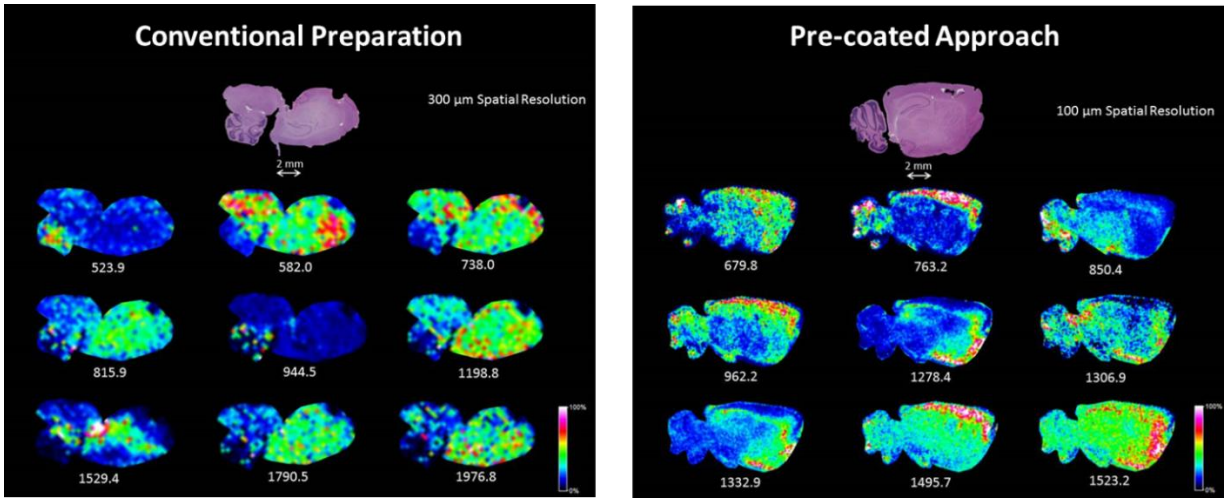

Figure 7.9. Digestion of FFPE rat brain tissue by trypsin in the ionic matrix and trypsin in 100 mM ammonium bicarbonate buffer solution. A 1 uL solution was hand-spotted onto serial tissue sections. The trypsin concentration was the same in both cases (0.1 mg/mL).

APPENDIX A. MATLAB DESCRIPTIONS OF MODEL BEAM PROFILES

2D Top-hat Profile

```
% Top-hat 2D

x = -5:0.05:5;
y = -5:0.05:5;
a = 1;
% y = -5:0.05:5;

i = find (x <= a & x >= -a);
j = find (x > a | x < -a);
k = find(x > a);


z = zeros(201,201);
for m = 1:201
    for n = 1:201
if x(m)^2 + y(n)^2 < 1
    z(m,n) = 1/pi;
else
    z(m,n) = 0;
end
    end
end

% Probability density function


surf(x,y,z,'EdgeColor','flat')

% Line spread function

pdf(i) = 1/pi*2*sqrt(a^2 - x(i).^2);
pdf (j) = 0;
figure; plot(x,pdf)

% Cumulative density function

cdf(i) = 1/pi*[x(i).*sqrt(a^2 - x(i).^2) + a^2*atan(x(i)./sqrt(a^2 -
x(i).^2)) + pi*a^2/2];
cdf(j) = 0;
cdf(k) = 1;

figure;
```

```
plot(x,cdf)
```

2D Gaussian Profile

```
sigma = 1;
mu = 0;
x = -5:0.05:5;
y = -5:0.05:5;

% Probability density function

PDF_2D = zeros(201);
for i = 1:201
PDF_2D(:,i)    =    1/(sigma^2*2*pi)*exp(-(x-mu).^2/(2*sigma^2)    -    (y(i)-
mu).^2/(2*sigma^2));
end

surf(x,y,PDF_2D,'edgecolor','none')

% Line spread function

LSF = 1/(sigma*sqrt(2*pi))*exp(-(x-mu).^2/(2*sigma^2));
figure; plot(x, LSF)

% Cumulative density function

CDF = 1/2*(1 + erf(x/(sqrt(2)*sigma)));
figure; plot(x, CDF)
```

1D Lorentzian Profile

```
% Lorentzian 1-D

x = -5:0.05:5;
gamma = 1;
x0 = 0;


% Probability density function

figure; pdf = 1./[pi*gamma*(1 + ((x - x0)/gamma).^2)];
plot(x,pdf)

% Cumulative density function

cdf = 1/pi*atan((x-x0)/gamma) + 1/2;
figure; plot(x,cdf)
```

APPENDIX B. MATLAB CODE FOR CALCULATION OF IMAGES FROM A TEST PATTERN

Test pattern with increment features ranging from 1 to 100 um, separated groupings

The following code describes the test pattern presented in Figure 2.13

```
% i = feature size
% j = number for each feature including blanks
% k = to the space counter

k = 100;
z(1:k) = 0;
for i = 1:10
    for j = 1:10
        k = k + i;
        if mod(j,2) == 0
            z(k:k+i-1) = 1;
        else
            z(k:k+i-1) = 0;
        end
    end
    k = k +20;
end

for i = 11:50
    if mod(i,2) == 0
   for j = 1:10
        k = k + i;
        if mod(j,2) == 0
            z(k:k+i-1) = 1;
        else
            z(k:k+i-1) = 0;
        end
    end
    k = k +50;
    end
end

for i = 51:100
    if mod(i,5) == 0
   for j = 1:10
        k = k + i;
        if mod(j,2) == 0
```

```
            z(k:k+i-1) = 1;
        else
            z(k:k+i-1) = 0;
        end
    end
    k = k +100;
    end
end

for i = 2:600
    z(i,:) = z(1,:);
end

% surf(z,'edgecolor','none')
imagesc(z)
```

2D Gaussian Function

```
% output is the value of Gaussian function at each value of x and y
% mat is the matrix of 2D space defined by x and y
% Sigma controls the width of the Gaussian beam
% center = [center_x center_y] is the position of the beam center

function [mat] = gauss2d(mat, sigma, center)
gsize = size(mat);
[R,C] = ndgrid(1:gsize(1), 1:gsize(2));
mat = gaussC(R,C, sigma, center);

function val = gaussC(x, y, sigma, center)
xc = center(1);
yc = center(2);
exponent = ((x-xc).^2 + (y-yc).^2)./(2*sigma^2);
val       = (exp(-exponent));
end

end
```

Convolution of the test pattern with a 2D Gaussian

```
% Convolution of pattern and Gaussian Function

% x is the distance in x-direction
% y is the value of -1 and +1

clear i j k

[dim1 dim2] = size(z);

ss = 5; %Step Size
sigma = 5;

x = ss:ss:(dim2-100);
```

```
y = ss:ss:(dim1-100);

image = zeros(dim1,dim2);

mat = zeros(101);
gauss_array = gauss2d(mat, sigma, [50 50]);

k = randi([0 3], 1,600/ss);

for i = 1:(dim2-100)/ss
    for j = 1:(dim1-100)/ss
            z_ROI = z(y(j):y(j)+ 100, x(i) - k(j):x(i)+100 - k(j));
            conv = z_ROI.*gauss_array;
            image(j*ss+50:j*ss+ss+49, i*ss+50:i*ss+ss+49) = sum(sum(conv));
    end
end

figure;plot(1:dim2,sum(image,1), 'b')
str = sprintf('Image: Step size = %d and Sigma = %d',ss, sigma);
title(str)
xlabel('x-distance (\mum)')
ylabel('Intensity (arbitrary units)')

a = sum(image,1);
y = zeros(1,dim2) + mean(a(200:dim2))*0.1/0.5;
hold on; plot(1:dim2,y, 'r')
set(gca,'fontsize',14)
```

APPENDIX C. LINE SCAN DATA FOR A BRUKER ULTRAFLEX TOF/TOF

Table C-1. Effect of laser focus setting on the spatial resolution. Three different focus settings were tested: 51% (Medium), 70% (Small) and 100% (Minimum). Power was adjusted individually for each setting to ensure comparable MS signal. Results shown for Ultraflex TOF/TOF, positive reflectron mode, 40 laser shots, 1000 Hz laser frequency, and 10 μm stage step size. In the computation of average signal, the blank pixels was excluded. About 10 adjacent scan lines were averaged in each case.

Laser Focus (%)	Average Signal/Pixel (x 10^4)	Minimum Resolved Feature (μm)
51	3.33	60
51	3.10	60
51	3.71	60
70	1.91	45
70	1.69	45
70	1.93	45
100	3.82	<30
100	4.34	<30
100	4.58	<30

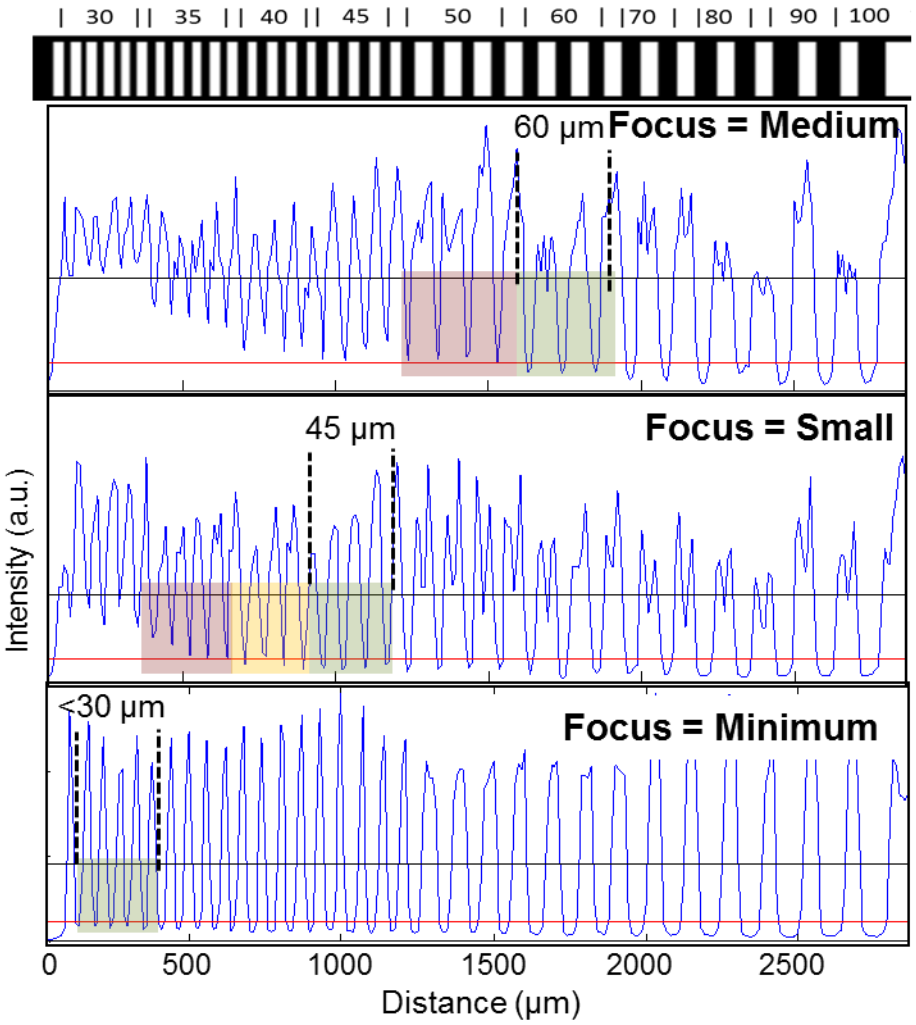

Figure C.1. Effect of laser focus setting on the spatial resolution. As the focus setting was changed from 'medium' to 'minimum', the spatial resolution increased from 60 µm to below 30 µm. Results shown for Ultraflex TOF/TOF, positive reflectron mode, 40 laser shots, 1000 Hz laser frequency, and 10 µm stage step size. In the computation of average signal, the blank pixels was excluded. About 10 adjacent scan lines were averaged in each case.

Table C-2. Effect of laser power setting on the spatial resolution. Focus setting was set constant at 80% for all three cases. Results shown for Ultraflex TOF/TOF, positive reflectron mode, 40 laser shots, 1000 Hz laser frequency, and 10 μm stage step size. In the computation of average signal, the blank pixels were excluded. About 10 adjacent scan lines were averaged in each case.

Total Power (%)	Average Signal/Pixel ($\times 10^4$)	Minimum Resolved Feature (μm)
80.5	0.344	35
81.4	1.78	50
82.3	4.88	90

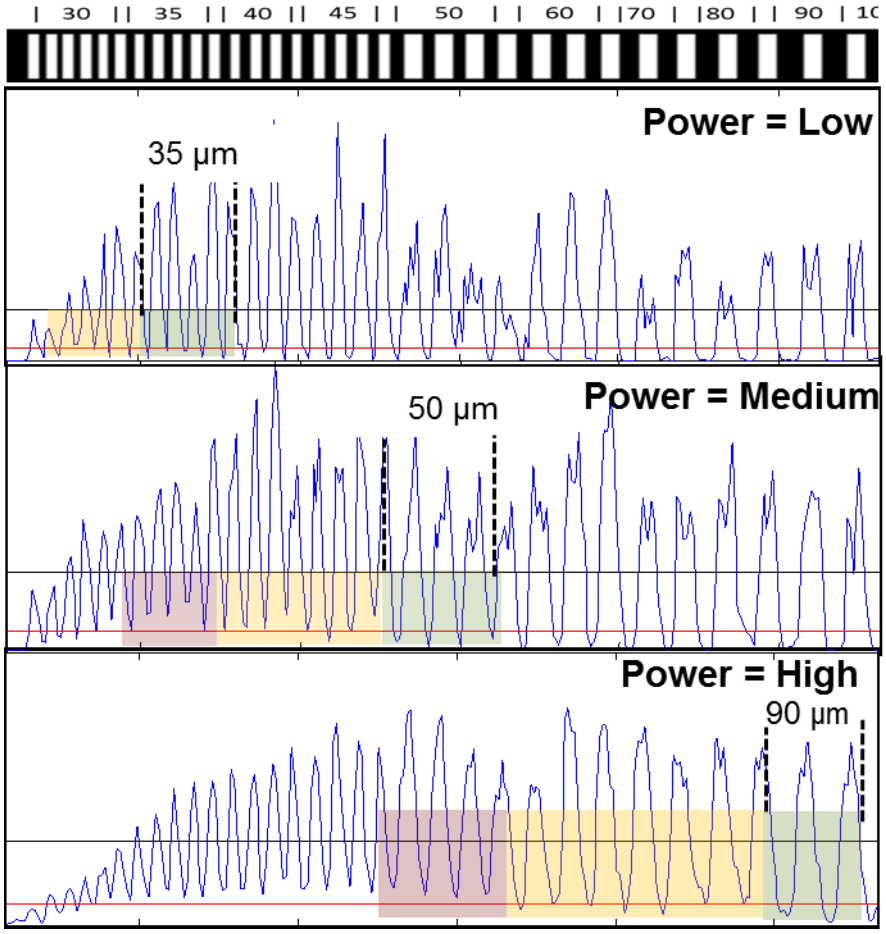

Figure C.2. Effect of power setting on the spatial resolution. As the beam power was increased from the low to the high setting, the spatial resolution decreased from 35 to 90 µm. Results shown for Ultraflex TOF/TOF, positive reflectron mode, 40 laser shots, 1000 Hz laser frequency, and 10 µm stage step size. In the computation of average signal, the blank pixels were excluded. About 10 adjacent scan lines were averaged in each case.

REFERENCES

1. Caprioli, R. M.; Farmer, T. B.; Gile, J., Molecular imaging of biological samples: Localization of peptides and proteins using MALDI-TOF MS. *Anal Chem* **1997,** *69* (23), 4751-4760.

2. Murphy, R. C.; Hankin, J. A.; Barkley, R. M., Imaging of lipid species by MALDI mass spectrometry. *J Lipid Res* **2009,** *50*, S317-S322.

3. Spraggins, J. M.; Rizzo, D. G.; Moore, J. L.; Rose, K. L.; Hammer, N. D.; Skaar, E. P.; Caprioli, R. M., MALDI FTICR IMS of Intact Proteins: Using Mass Accuracy to Link Protein Images with Proteomics Data. *J Am Soc Mass Spectr* **2015,** *26* (6), 974-985.

4. Buck, A.; Ly, A.; Balluff, B.; Sun, N.; Gorzolka, K.; Feuchtinger, A.; Janssen, K. P.; Kuppen, P. J.; van de Velde, C. J.; Weirich, G.; Erlmeier, F.; Langer, R.; Aubele, M.; Zitzelsberger, H.; Aichler, M.; Walch, A., High-resolution MALDI-FT-ICR MS imaging for the analysis of metabolites from formalin-fixed, paraffin-embedded clinical tissue samples. *The Journal of pathology* **2015**.

5. McDonnell, L. A.; Heeren, R. M., Imaging mass spectrometry. *Mass Spectrom Rev* **2007,** *26* (4), 606-43.

6. Cornett, D. S.; Reyzer, M. L.; Chaurand, P.; Caprioli, R. M., MALDI imaging mass spectrometry: molecular snapshots of biochemical systems. *Nat Methods* **2007,** *4* (10), 828-33.

7. Tanaka, K.; Waki, H.; Ido, Y.; Akita, S.; Yoshida, Y.; Yoshida, T.; Matsuo, T., Protein and polymer analyses up to m/z 100 000 by laser ionization time-of-flight mass spectrometry. *Rapid Communications in Mass Spectrometry* **1988,** *2* (8), 151-153.

8. Knochenmuss, R.; Zenobi, R., MALDI ionization: The role of in-plume processes. *Chem Rev* **2003,** *103* (2), 441-452.

9. Muddiman, D. C.; Bakhtiar, R.; Hofstadler, S. A.; Smith, R. D., Matrix-assisted laser desorption/ionization mass spectrometry - Instrumentation and applications. *J Chem Educ* **1997,** *74* (11), 1288-1292.

10. Karas, M.; Gluckmann, M.; Schafer, J., Ionization in matrix-assisted laser desorption/ionization: singly charged molecular ions are the lucky survivors. *J Mass Spectrom* **2000,** *35* (1), 1-12.

11. Belu, A. M.; Graham, D. J.; Castner, D. G., Time-of-flight secondary ion mass spectrometry: techniques and applications for the characterization of biomaterial surfaces. *Biomaterials* **2003,** *24* (21), 3635-3653.

12. Fletcher, J. S.; Vickerman, J. C., Secondary ion mass spectrometry: characterizing complex samples in two and three dimensions. *Analytical chemistry* **2013,** *85* (2), 610-39.

13. Herzog, R. F. K.; Viehböck, F. P., Ion Source for Mass Spectrography. *Physical Review* **1949,** *76* (6), 855-856.

14. Takats, Z.; Wiseman, J. M.; Gologan, B.; Cooks, R. G., Mass spectrometry sampling under ambient conditions with desorption electrospray ionization. *Science* **2004,** *306* (5695), 471-473.

15. Campbell, D. I.; Ferreira, C. R.; Eberlin, L. S.; Cooks, R. G., Improved spatial resolution in the imaging of biological tissue using desorption electrospray ionization. *Analytical and bioanalytical chemistry* **2012,** *404* (2), 389-398.

16. Van de Plas, R.; Yang, J. H.; Spraggins, J.; Caprioli, R. M., Image fusion of mass spectrometry and microscopy: a multimodality paradigm for molecular tissue mapping. *Nature methods* **2015,** *12* (4), 366-U138.

17. Gessel, M. M.; Norris, J. L.; Caprioli, R. M., MALDI imaging mass spectrometry: Spatial molecular analysis to enable a new age of discovery. *J Proteomics* **2014,** *107*, 71-82.

18. Schwartz, S. A.; Reyzer, M. L.; Caprioli, R. M., Direct tissue analysis using matrix-assisted laser desorption/ionization mass spectrometry: practical aspects of sample preparation. *J Mass Spectrom* **2003,** *38* (7), 699-708.

19. Wiangnon, K.; Cramer, R., Sample Preparation: A Crucial Factor for the Analytical Performance of Rationally Designed MALDI Matrices. *Anal Chem* **2015,** *87* (3), 1485-8.

20. Angel, P. M.; Spraggins, J. M.; Baldwin, H. S.; Caprioli, R., Enhanced sensitivity for high spatial resolution lipid analysis by negative ion mode matrix assisted laser desorption ionization imaging mass spectrometry. *Analytical chemistry* **2012,** *84* (3), 1557-64.

21. Seeley, E. H.; Oppenheimer, S. R.; Mi, D.; Chaurand, P.; Caprioli, R. M., Enhancement of protein sensitivity for MALDI imaging mass spectrometry after chemical treatment of tissue sections. *J Am Soc Mass Spectr* **2008,** *19* (8), 1069-1077.

22. Yang, J. H.; Caprioli, R. M., Matrix Sublimation/Recrystallization for Imaging Proteins by Mass Spectrometry at High Spatial Resolution. *Analytical chemistry* **2011,** *83* (14), 5728-5734.

23. Laiko, V. V.; Baldwin, M. A.; Burlingame, A. L., Atmospheric pressure matrix assisted laser desorption/ionization mass spectrometry. *Analytical chemistry* **2000,** *72* (4), 652-657.

24. Zubarev, R. A.; Makarov, A., Orbitrap Mass Spectrometry. *Analytical chemistry* **2013,** *85* (11), 5288-5296.

25. Plass, W. R.; Dickel, T.; Scheidenberger, C., Multiple-reflection time-of-flight mass spectrometry. *Int J Mass Spectrom* **2013,** *349*, 134-144.

26. Mann, M.; Hendrickson, R. C.; Pandey, A., Analysis of proteins and proteomes by mass spectrometry. *Annu Rev Biochem* **2001,** *70*, 437-473.

27. Marshall, A. G.; Hendrickson, C. L.; Jackson, G. S., Fourier transform ion cyclotron resonance mass spectrometry: A primer. *Mass Spectrometry Reviews* **1998,** *17* (1), 1-35.

28. Alexandrov, T., MALDI imaging mass spectrometry: statistical data analysis and current computational challenges. *Bmc Bioinformatics* **2012,** *13*.

29. Deininger, S. O.; Cornett, D. S.; Paape, R.; Becker, M.; Pineau, C.; Rauser, S.; Walch, A.; Wolski, E., Normalization in MALDI-TOF imaging datasets of proteins: practical considerations. *Analytical and bioanalytical chemistry* **2011,** *401* (1), 167-181.

30. Castellino, S.; Groseclose, M. R.; Wagner, D., MALDI imaging mass spectrometry: bridging biology and chemistry in drug development. *Bioanalysis* **2011,** *3* (21), 2427-2441.

31. Walch, A.; Rauser, S.; Deininger, S. O.; Hofler, H., MALDI imaging mass spectrometry for direct tissue analysis: a new frontier for molecular histology. *Histochem Cell Biol* **2008,** *130* (3), 421-434.

32. Croxatto, A.; Prod'hom, G.; Greub, G., Applications of MALDI-TOF mass spectrometry in clinical diagnostic microbiology. *Fems Microbiol Rev* **2012,** *36* (2), 380-407.

33. Ha, M.; Kwak, J. H.; Kim, Y.; Zee, O. P., Direct analysis for the distribution of toxic glycoalkaloids in potato tuber tissue using matrix-assisted laser desorption/ionization mass spectrometric imaging. *Food Chem* **2012,** *133* (4), 1155-1162.

34. Senoner, M.; Wirth, T.; Unger, W. E. S., Imaging surface analysis: Lateral resolution and its relation to contrast and noise. *J Anal Atom Spectrom* **2010,** *25* (9), 1440-1452.

35. Passarelli, M. K.; Wang, J.; Mohammadi, A. S.; Trouillon, R.; Gilmore, I.; Ewing, A. G., Development of an Organic Lateral Resolution Test Device for Imaging Mass Spectrometry. *Analytical chemistry* **2014,** *86* (19), 9473-9480.

36. Senoner, M.; Maassdorf, A.; Rooch, H.; Osterle, W.; Malcher, M.; Schmidt, M.; Kollmer, F.; Paul, D.; Hodoroaba, V. D.; Rades, S.; Unger, W. E., Lateral resolution of nanoscaled images delivered by surface-analytical instruments: application of the BAM-L200 certified reference material and related ISO standards. *Analytical and bioanalytical chemistry* **2014**.

37. Gates, B. D.; Xu, Q. B.; Stewart, M.; Ryan, D.; Willson, C. G.; Whitesides, G. M., New approaches to nanofabrication: Molding, printing, and other techniques. *Chem Rev* **2005,** *105* (4), 1171-1196.

38. Reichmanis, E.; Thompson, L. F., Polymer Materials for Microlithography. *Chem Rev* **1989,** *89* (6), 1273-1289.

39. Biebuyck, H. A.; Larsen, N. B.; Delamarche, E.; Michel, B., Lithography beyond light: Microcontact printing with monolayer resists. *Ibm J Res Dev* **1997,** *41* (1-2), 159-170.

40. Biswal, D.; Chirra, H. D.; Hilt, J. Z., Fabrication of hydrogel microstructures using polymerization controlled by microcontact printing (PC mu CP). *Biomed Microdevices* **2008,** *10* (2), 213-219.

41. Qin, D.; Xia, Y. N.; Whitesides, G. M., Soft lithography for micro- and nanoscale patterning. *Nat Protoc* **2010,** *5* (3), 491-502.

42. Choi, J. H.; Kim, D.; Yoo, P. J.; Lee, H. H., Simple detachment patterning of organic layers and its application to organic light-emitting diodes. *Adv Mater* **2005,** *17* (2), 166-+.

43. Wang, Z.; Xing, R. B.; Yu, X. H.; Han, Y. C., Adhesive lithography for fabricating organic electronic and optoelectronics devices. *Nanoscale* **2011,** *3* (7), 2663-2678.

44. Packard, C. E.; Aidala, K. E.; Ramanan, S.; Bulovic, V., Patterned Removal of Molecular Organic Films by Diffusion. *Langmuir* **2011,** *27* (15), 9073-9076.

45. Yunker, P. J.; Still, T.; Lohr, M. A.; Yodh, A. G., Suppression of the coffee-ring effect by shape-dependent capillary interactions. *Nature* **2011,** *476* (7360), 308-311.

46. Holle, A.; Haase, A.; Kayser, M.; Hohndorf, J., Optimizing UV laser focus profiles for improved MALDI performance. *J Mass Spectrom* **2006,** *41* (6), 705-716.

47. Senoner, M.; Wirth, T.; Unger, W.; Osterle, W.; Kaiander, I.; Sellin, R. L.; Bimberg, D., BAM-L002 - a new type of certified reference material for length calibration and testing of lateral resolution in the nanometre range. *Surf Interface Anal* **2004,** *36* (10), 1423-U9.

48. Senoner, M.; Unger, W. E. S., Lateral resolution of secondary ion mass spectrometry-results of an inter-laboratory comparison. *Surf Interface Anal* **2007,** *39* (1), 16-25.

49. Stephan R. Fagerer, A. R., Konstantins Jefimovs, Gerd Hayenga, Robert Steinhoff, Jasmin Krismer, Martin Pabst, Alfredo J. Ilbanez and Renato Zenobi, Resolution pattern for mass spectrometry imaging. *Rapid Communications in Mass Spectrometry* **2015,** *29*, 1-6.

50. Rolland, J. P.; Hagberg, E. C.; Denison, G. M.; Carter, K. R.; DeSimone, J. M., High-resolution soft lithography: Enabling materials for nanotechnologies. *Angew Chem Int Edit* **2004,** *43* (43), 5796-5799.

51. Ishii, Y.; Isoya, A.; Kojima, T.; Arakawa, K., Estimation of keV submicron ion beam width using a knife-edge method. *Nucl Instrum Meth B* **2003,** *211* (3), 415-424.

52. Khosrofian, J. M.; Garetz, B. A., Measurement of a Gaussian Laser-Beam Diameter through the Direct Inversion of Knife-Edge Data. *Appl Optics* **1983,** *22* (21), 3406-3410.

53. Prentice, B. M.; Chumbley, C. W.; Caprioli, R. M., High-speed MALDI MS/MS imaging mass spectrometry using continuous raster sampling. *J Mass Spectrom* **2015,** *50* (4), 703-710.

54. Spraggins, J. M.; Caprioli, R., High-Speed MALDI-TOF Imaging Mass Spectrometry: Rapid Ion Image Acquisition and Considerations for Next Generation Instrumentation. *J Am Soc Mass Spectr* **2011,** *22* (6), 1022-1031.

55. Groseclose, M. R.; Andersson, M.; Hardesty, W. M.; Caprioli, R. M., Identification of proteins directly from tissue: in situ tryptic digestions coupled with imaging mass spectrometry. *J Mass Spectrom* **2007,** *42* (2), 254-262.

56. Groseclose, M. R.; Massion, P. R.; Chaurand, P.; Caprioli, R. M., High-throughput proteomic analysis of formalin-fixed paraffin-embedded tissue microarrays using MALDI imaging mass spectrometry. *Proteomics* **2008,** *8* (18), 3715-3724.

57. Koutsopoulos, S.; Patzsch, K.; Bosker, W. T. E.; Norde, W., Adsorption of trypsin on hydrophilic and hydrophobic surfaces. *Langmuir* **2007,** *23* (4), 2000-2006.

58. Havlis, J.; Thomas, H.; Sebela, M.; Shevchenko, A., Fast-response proteomics by accelerated in-gel digestion of proteins. *Analytical chemistry* **2003,** *75* (6), 1300-1306.

59. Finehout, E. J.; Cantor, J. R.; Lee, K. H., Kinetic characterization of sequencing grade modified trypsin. *Proteomics* **2005,** *5* (9), 2319-2321.

60. Strader, M. B.; Tabb, D. L.; Hervey, W. J.; Pan, C. L.; Hurst, G. B., Efficient and specific trypsin digestion of microgram to nanogram quantities of proteins in organic-aqueous solvent systems. *Analytical chemistry* **2006,** *78* (1), 125-134.

61. Crank, J. A.; Armstrong, D. W., Towards a Second Generation of Ionic Liquid Matrices (ILMs) for MALDI-MS of Peptides, Proteins, and Carbohydrates. *J Am Soc Mass Spectr* **2009,** *20* (10), 1790-1800.

62. Armstrong, D. W.; Zhang, L. K.; He, L. F.; Gross, M. L., Ionic liquids as matrixes for matrix-assisted laser desorption/ionization mass spectrometry. *Analytical chemistry* **2001,** *73* (15), 3679-3686.

63. Harris, W. A.; Janecki, D. J.; Reilly, J. P., Use of matrix clusters and trypsin autolysis fragments as mass calibrants in matrix-assisted laser desorption/ionization time-of-flight mass spectrometry. *Rapid Communications in Mass Spectrometry* **2002,** *16* (18), 1714-1722.

64. De Sio, G.; Smith, A. J.; Galli, M.; Garancini, M.; Chinello, C.; Bono, F.; Pagni, F.; Magni, F., A MALDI-Mass Spectrometry Imaging method applicable to different formalin-fixed paraffin-embedded human tissues. *Mol Biosyst* **2015,** *11* (6), 1507-14.

65. Gessel, M.; Spraggins, J. M.; Voziyan, P.; Hudson, B. G.; Caprioli, R. M., Decellularization of intact tissue enables MALDI imaging mass spectrometry analysis of the extracellular matrix. *J Mass Spectrom* **2015,** *50* (11), 1288-1293.

66. Gilmore, I. S.; Seah, M. P., Ion detection efficiency in SIMS: dependencies on energy, mass and composition for microchannel plates used in mass spectrometry. *Int J Mass Spectrom* **2000,** *202* (1-3), 217-229.

67. Franck, J.; Longuespee, R.; Wisztorski, M.; Van Remoortere, A.; Van Zeijl, R.; Deelder, A.; Salzet, M.; McDonnell, L.; Fournier, I., MALDI mass spectrometry imaging of proteins exceeding 30 000 daltons. *Med Sci Monitor* **2010,** *16* (9), Br293-Br299.

68. Mainini, V.; Bovo, G.; Chinello, C.; Gianazza, E.; Grasso, M.; Cattoretti, G.; Magni, F., Detection of high molecular weight proteins by MALDI imaging mass spectrometry. *Mol Biosyst* **2013,** *9* (6), 1101-1107.

69. Leinweber, B. D.; Tsaprailis, G.; Monks, T. J.; Lau, S. S., Improved MALDI-TOF Imaging Yields Increased Protein Signals at High Molecular Mass. *J Am Soc Mass Spectr* **2009,** *20* (1), 89-95.

70. Chen, X. Y.; Westphall, M. S.; Smith, L. M., Mass spectrometric analysis of DNA mixtures: Instrumental effects responsible for decreased sensitivity with increasing mass. *Anal Chem* **2003,** *75* (21), 5944-5952.

71. Casadonte, R.; Caprioli, R. M., Proteomic analysis of formalin-fixed paraffin-embedded tissue by MALDI imaging mass spectrometry. *Nat Protoc* **2011,** *6* (11), 1695-1709.

72. Grove, K. J.; Frappier, S. L.; Caprioli, R. M., Matrix Pre-Coated MALDI MS Targets for Small Molecule Imaging in Tissues. *J Am Soc Mass Spectr* **2011,** *22* (1), 192-195.

73. Yang, J. H.; Caprioli, R. M., Matrix Precoated Targets for Direct Lipid Analysis and Imaging of Tissue. *Anal Chem* **2013,** *85* (5), 2907-2912.

74. Yang, J. H.; Caprioli, R. M., Matrix pre-coated targets for high throughput MALDI imaging of proteins. *J Mass Spectrom* **2014,** *49* (5), 417-422.

75. Harris, G. A.; Nicklay, J. J.; Caprioli, R. M., Localized in Situ Hydrogel-Mediated Protein Digestion and Extraction Technique for on-Tissue Analysis. *Analytical chemistry* **2013,** *85* (5), 2717-2723.

76. Taverna, D.; Norris, J. L.; Caprioli, R. M., Histology-Directed Microwave Assisted Enzymatic Protein Digestion for MALDI MS Analysis of Mammalian Tissue. *Analytical chemistry* **2015,** *87* (1), 670-676.

77. Andersson, M.; Groseclose, M. R.; Deutch, A. Y.; Caprioli, R. M., Imaging mass spectrometry of proteins and peptides: 3D volume reconstruction. *Nat Methods* **2008,** *5* (1), 101-108.

78. Boggs, J. M., Myelin basic protein: a multifunctional protein. *Cell Mol Life Sci* **2006,** *63* (17), 1945-1961.

79. Seeley, E. H.; Caprioli, R. M., Molecular imaging of proteins in tissues by mass spectrometry. *P Natl Acad Sci USA* **2008,** *105* (47), 18126-18131.

80. Ma, J. F.; Liang, Z.; Qiao, X. Q.; Deng, Q. L.; Tao, D. Y.; Zhang, L. H.; Zhang, Y. K., Organic-inorganic hybrid silica monolith based immobilized trypsin reactor with high enzymatic activity. *Analytical chemistry* **2008,** *80* (8), 2949-2956.

81. Erlanger, B. F.; Kokowsky, N.; Cohen, W., The preparation and properties of two new chromogenic substrates of trypsin. *Arch Biochem Biophys* **1961,** *95*, 271-8.

82. Maes, E.; Broeckx, V.; Mertens, I.; Sagaert, X.; Prenen, H.; Landuyt, B.; Schoofs, L., Analysis of the formalin-fixed paraffin-embedded tissue proteome: pitfalls, challenges, and future prospectives. *Amino Acids* **2013,** *45* (2), 205-218.

83. Lemaire, R.; Desmons, A.; Tabet, J. C.; Day, R.; Salzet, M.; Fournier, I., Direct analysis and MALDI imaging of formalin-fixed, paraffin-embedded tissue sections. *J Proteome Res* **2007,** *6* (4), 1295-305.